

Lea Alexandra Brandner, BSc

# **Alkyne Activation on Bio-inspired Tungsten-Complexes**

## **MASTERARBEIT**

zur Erlangung des akademischen Grades

Master of Science

Masterstudium Chemie

eingereicht an der

**Technischen Universität Graz**

Betreuerin

Univ.-Prof. Dr. Nadia C. Mösch-Zanetti

Institut für Chemie, Bereich Anorganische Chemie

Karl-Franzens-Universität Graz

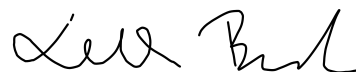
## EIDESSTATTLICHE ERKLÄRUNG

Ich erkläre an Eides statt, dass ich die vorliegende Arbeit selbstständig verfasst, andere als die angegebenen Quellen/Hilfsmittel nicht benutzt, und die den benutzten Quellen wörtlich und inhaltlich entnommenen Stellen als solche kenntlich gemacht habe. Das in TUGRAZonline hochgeladene Textdokument ist mit der vorliegenden Masterarbeit identisch.

26.04.2019

---

Datum

A handwritten signature in black ink, appearing to read 'Ludwig B...'. The signature is written in a cursive style.

---

Unterschrift

**Few scientists acquainted with the chemistry of biological systems at the molecular level  
can avoid being inspired.**

(Donald J. Cram, 1919 - 2001)

## **ACKNOWLEDGEMENT**

First, I would like to thank Prof. Dr. Nadia Mösch-Zanetti for giving me the opportunity to go abroad and branch out into new fields of chemistry. Thank you for helping me find an advisor at the University of New Mexico and supporting me in the administrative challenges connected with studying overseas.

I am equally thankful to Prof. Dr. Martin L. Kirk for welcoming me into his group at UNM and giving me new insight into spectroscopy. Thank you for always making time to meet and the countless hours we spent trying to connect the dots between experimental and computational results.

I want to thank Dr. Jing Yang for collecting and processing the large amount of XAS data and Dr. Cass Richers for helping me out whenever I was facing problems in the lab.

I am very grateful to Carina Vidovic for sharing her knowledge on tungsten chemistry with me, providing chemical precursors for my experiments and having an open ear for my personal difficulties. Thank you for dealing with my ups and downs and your constructive feedback on my work.

Furthermore, I would like to thank Dr. Ferdinand Belaj for his support with my crystallographic data.

I also want to thank all of my friends in Graz for the wonderful moments we shared in lecture halls, while playing cards or racing down ski slopes. I am particularly grateful to Karin Ratzenböck and Kordula Schnabls for regularly checking in with me over skype despite the large time difference and their kind words whenever I was feeling frustrated or upset. Your friendship is a true gift that I would not trade for anything.

Last but not least, I want to thank my family for always being there for me and making me feel so loved. Your constant and unconditional support means everything to me.

## ABSTRACT

The tungsten-dependent enzyme acetylene hydratase catalyzes the non-redox reaction of acetylene to acetaldehyde. Density functional theory (DFT) calculations were performed to determine the influence of acetylene-activation by the W(IV)-center in first-shell mechanistic proposals. The active site for this study was modeled based on the crystal structure of the enzyme. According to the calculations, an activation energy of 49.6 kcal/mol is required to hydrate  $\eta^2$ -bound acetylene by a water molecule in a concerted fashion.

In addition to the DFT calculations, the bio-inspired, heteroscorpionate ligand (2-dimethylethanethiol)-bis(3,5-dimethylpyrazol)methane (L3SH) was used to mimic the active site of acetylene hydratase. A synthetic approach toward a series of complexes of the type  $[\text{WO}(\text{C}_2\text{R}_2)(\text{L3S})\text{Br}]$  (R = Ph, Me, H) was investigated. The W(II)-complexes  $[\text{W}(\text{CO})(\text{C}_2\text{R}_2)(\text{L3S})\text{Br}]$  (R = Ph (**1**), Me (**2**), H (**3**)) were synthesized via the "ligand addition" method starting from W bis(alkyne)-precursors  $[\text{W}(\text{CO})(\text{C}_2\text{R}_2)_2(\text{CH}_3\text{CN})\text{Br}_2]$  (R = Ph, Me, H). Oxidation attempts of complexes **1 - 3** with the oxygen atom transfer reagents pyridine *N*-oxide, meta-chloro-perbenzoic acid and dimethyl dioxirane did not indicate the formation of the desired W(IV)-complexes. Complexes **1 - 3** were characterized by NMR and IR spectroscopy. Additionally, molecular structures of compounds **1** and **2** were obtained by X-ray diffraction analysis.

In order to further elucidate the electronic structure of biomimetic model compounds of acetylene hydratase, similar complexes of the type  $[\text{W}(\text{CO})(\text{C}_2\text{R}_2)\text{L}_2]$  and  $[\text{WO}(\text{C}_2\text{R}_2)\text{L}_2]$  (**4 - 15**) were probed by tungsten L-edge and sulfur K-edge X-ray absorption spectroscopy. Tungsten L1-edge spectra displayed higher rising edge energies by approximately 2 eV for the oxo-complexes compared to the carbonyl-analogs. Transitions of the sulfur 1s electron into the W  $d(xy)$ - and W  $d(x^2-y^2/xz)$ -based orbitals for the CO-complexes and into the W  $d(xz)$ - and W  $d(x^2-y^2/xz)$ -based orbitals for the oxo-complexes were assigned to the pre-edge features of the S K-edge spectra. This indicates oxidation states +II for W in the CO- and +IV for W in the oxo-complexes. The collected S K-edge data furthermore suggests less W-S-interaction in thiolate- compared to dithiolene-complexes.

## KURZFASSUNG

Das von Wolfram abhängige Enzym Acetylen Hydratase katalysiert die Nicht-Redoxreaktion von Acetylen zu Acetaldehyd. Dichtefunktionaltheorie (DFT) Rechnungen wurden durchgeführt, um den Einfluss der Acetylenaktivierung durch das W(IV)-Zentrum in Vorschlägen zu First-Shell-Mechanismen festzustellen. Für diese Studie wurde das aktive Zentrum basierend auf der Kristallstruktur des Enzyms modelliert. Gemäß den Rechnungen, wird eine Aktivierungsenergie von 49.6 kcal/mol benötigt, um  $\eta^2$ -gebundenes Acetylen mit einem Wassermolekül konzertiert zu hydrieren.

Ergänzend zu den DFT Rechnungen wurde der bio-inspirierte, heteroscorpionate Ligand (2-Dimethylethanthiol)-bis(3,5-dimethylpyrazol)methan (L3SH) verwendet, um das aktive Zentrum von Acetylen Hydratase nachzuahmen. Ein synthetischer Ansatz in Richtung einer Reihe von Komplexen des Typs  $[\text{WO}(\text{C}_2\text{R}_2)(\text{L3S})\text{Br}]$  ( $\text{R} = \text{Ph}, \text{Me}, \text{H}$ ) wurde untersucht. Die W(II)-Komplexe  $[\text{W}(\text{CO})(\text{C}_2\text{R}_2)(\text{L3S})\text{Br}]$  ( $\text{R} = \text{Ph}$  (**1**),  $\text{Me}$  (**2**),  $\text{H}$  (**3**)) wurden ausgehend von den W bis(alkin) Vorstufen  $[\text{W}(\text{CO})(\text{C}_2\text{R}_2)_2(\text{CH}_3\text{CN})\text{Br}_2]$  ( $\text{R} = \text{Ph}, \text{Me}, \text{H}$ ) via der „Ligandenadditions“-Methode synthetisiert. Oxidationsversuche der Komplexe **1 - 3** mit den Sauerstoff übertragenden Reagenzien Pyridin *N*-oxid, meta-Chlorperbenzoesäure und Dimethyldioxiran wiesen nicht auf die Bildung der erwünschten W(IV)-Komplexe hin. Komplexe **1 - 3** wurden mittels NMR und IR Spektroskopie charakterisiert. Zusätzlich wurden Molekülstrukturen der Komplexe **1** und **2** durch Röntgenstrukturanalyse erhalten.

Um die elektronische Struktur biomimetischer Modellverbindungen von Acetylen Hydratase weiter zu erläutern, wurden die Wolfram L-Kanten und Schwefel K-Kanten von Komplexen der Art  $[\text{W}(\text{CO})(\text{C}_2\text{R}_2)\text{L}_2]$  und  $[\text{WO}(\text{C}_2\text{R}_2)\text{L}_2]$  (**4 - 15**) mittels Röntgenabsorptionsspektroskopie gemessen. Wolfram L1-Kanten-Spektren weisen um etwa 2 eV höhere Absorptionskantenenergien für die Oxo-Komplexe im Vergleich zu den Carbonyl-Komplexen auf. Übergänge des Schwefel 1s Elektrons in W  $d(xy)$ - und W  $d(x^2-y^2/xz)$ -basierte Orbitale für CO-Komplexe und in W  $d(xz)$ - und W  $d(x^2-y^2/xz)$ -basierte Orbitale für Oxo-Komplexe wurden den Vorkantenmerkmalen der S K-Kantenspektren zugeordnet. Das weist auf Oxidationsstufen von +II für W in CO- und +IV für W in Oxo-Komplexen hin. Die aufgenommenen S K-Kantendaten deuten außerdem auf weniger W-S-Wechselwirkung in Thiolat- verglichen mit Dithiolen-Komplexen hin.

## TABLE OF CONTENTS

ABSTRACT .....	I
KURZFASSUNG .....	II
INTRODUCTION .....	1
1. BIOLOGICAL USE OF TUNGSTEN .....	1
1.1. Tungstoenzymes .....	2
1.2. Acetylene hydratase .....	3
1.2.1. Structure of acetylene hydratase .....	4
1.2.2. Reactivity of acetylene hydratase .....	5
1.2.3. Mechanistic studies on acetylene hydratase .....	6
1.2.4. Biomimetic models of acetylene hydratase .....	12
2. ELECTRONIC ABSORPTION SPECTROSCOPY .....	15
2.1. Spectroscopic selection rules .....	16
2.2. X-ray absorption spectroscopy (XAS) .....	19
2.2.1. XAS spectra .....	19
2.2.2. XANES .....	20
2.2.3. EXAFS .....	21
2.2.4. Ligand K-edge XAS .....	22
AIM OF THIS THESIS.....	24
RESULTS AND DISCUSSION .....	27
3. REVISITING THE REACTION MECHANISM OF AH.....	27
3.1. C-C-elongation .....	27
3.2. W-assisted hydration of acetylene .....	29
3.3. Enforcing early transition states for acetylene hydration.....	31
4. SYNTHESIS OF W ALKYNE-COMPLEXES .....	34
4.1. Synthesis of the W(II)-complexes $[W(CO)(C_2R_2)(L_3S)Br]$ (R = Ph, Me, H).....	34
4.1.1. Comparison of complexes of the type $[W(CO)(C_2H_2)L_2]$ .....	36
4.1.2. Comparison of complexes of the type $[W(CO)(C_2R_2)L_2]$ (R = Ph, Me, H).....	39
4.1.3. Molecular structures .....	41
4.2. Studies on W(IV)-complexes .....	43
4.2.1. OAT reactions .....	44

5.	XAS-STUDY OF W ALKYNE-COMPLEXES.....	47
5.1.	XAS assessment of oxidation states .....	48
5.2.	Pre-edge analysis.....	52
5.3.	Sulfur K-edge XAS .....	53
5.4.	Tungsten-sulfur covalencies .....	55
	CONCLUSION .....	58
	EXPERIMENTAL SECTION.....	60
6.	GENERAL INFORMATION ON COMPUTATIONAL METHODS.....	60
7.	GENERAL INFORMATION ON SYNTHETIC METHODS .....	60
7.1.	Experimental procedures .....	61
7.1.1.	[W(CO)(C <sub>2</sub> Ph <sub>2</sub> )(L3S)Br] (1).....	61
7.1.2.	[W(CO)(C <sub>2</sub> Me <sub>2</sub> )(L3S)Br] (2) .....	61
7.1.3.	[W(CO)(C <sub>2</sub> H <sub>2</sub> )(L3S)Br] (3) .....	62
8.	X-RAY ABSORPTION SPECTROSCOPY .....	63
8.1.	W L-edge XAS.....	63
8.2.	S K-edge XAS.....	63
8.3.	XAS Data Processing .....	64
8.4.	XAS TDDFT calculations .....	64
	REFERENCES .....	65
	APPENDIX .....	69



## INTRODUCTION

### 1. BIOLOGICAL USE OF TUNGSTEN

To date, various transition metals, such as V, Mn, Fe, Co, Ni, Cu, Zn, Mo and W, were found to play an important role in living systems.<sup>[1]</sup> Their individual biological functions vary from universal to organism-specific and can be of metabolic as well as structural nature. On a closer look, molybdenum and tungsten stand out against the other elements as they are the only representatives of the second and third transition row next to Cd and Hg.<sup>[1]</sup> They undertake similar biological tasks and are frequently referred to as twin elements. Despite that, most life forms including humans depend exclusively on Mo and only a few species use W instead. *Methanobacterium thermoautotrophicum* is a rare example, which is able to use both, Mo and W, based on the availability of the metals in the environment.<sup>[2,3]</sup>

Bioavailability and especially water solubility are critical for the universal biological use of an element. For tungsten, scheelite ( $\text{CaWO}_4$ ) and wolframite ( $(\text{Mn}, \text{Fe})\text{WO}_4$ ) are common ores, which contribute largely to the average concentration of tungsten in the oceans ( $< 1 \text{ nM}$ ).<sup>[4]</sup> Tungstate ( $\text{WO}_4^{2-}$ ) as the dominant species in water is stable over a wide pH range and generally redox indifferent.<sup>[2]</sup> Nevertheless, redox processes, particularly between the oxidation states +IV and +VI, are commonly observed when the metal is incorporated into enzymes.<sup>[3]</sup>

Despite the similar biological functions of Mo and W, molybdoenzymes are present in all domains of life whereas tungstoenzymes are mainly found in archaea. This sparked the theory that Mo gradually replaced W over time.<sup>[2,5]</sup> It is believed that under the hot, anaerobic conditions under which life arose, low-valent metal sulfides presented the main metal source. Indeed, molybdenum sulfide is less soluble in water than tungsten sulfide, increasing the bio-availability of the latter to early organisms.<sup>[6]</sup> Furthermore, tungsten-sulfur-bonds in enzymes exhibit higher stability than their molybdenum analogs.<sup>[3]</sup> Under the extreme conditions in the early stages of life, the third row transition metal was therefore presumably favored. However, upon cooling of Earth's crust and the rise of photosynthesis, which led to an oxygen-rich environment, the  $\text{O}_2$ -sensitive bio-active tungsten species were

put at a disadvantage. Molybdenum, on the other hand, became readily available and ubiquitous in nature due to the high solubility of molybdate in water.<sup>[3]</sup>

Nevertheless, tungsten has not been completely substituted by molybdenum during evolution and W-dependent archaea still exist.<sup>[2]</sup> Yet, these species are mostly found in extreme habitats, such as hydrothermal vents in the deep ocean or terrestrial geothermal sites. Studies on the metal content in the hyperthermophiles *Methanococcus jannaschii* and *Pyrococcus furiosus* versus the bacterium *Escherichia coli* showed that tungsten levels surpass molybdenum concentrations in the tested archaea while a reverse trend was found for mesophilic *E. coli*.<sup>[5]</sup> Despite these findings, there is no direct relationship between W-usage and extremophilicity in biology and it is currently believed that the exclusion of oxygen in these habitats is the crucial factor for W-dependent systems to occur.<sup>[2]</sup>

### 1.1. Tungstoenzymes

From a chemical point of view, the incorporation of metals into proteins is of particular interest. It facilitates catalytic pathways for many reactions including photosynthesis, dinitrogen fixation and the production of cellular energy.<sup>[7-9]</sup>

Tungsten usually enters the cytoplasm of cells in the form of tungstate in the oxidation state +VI.<sup>[2]</sup> Within the cellular machinery it is then bound to two dithiolene moieties of pterin co-factors forming the integral part of tungstoenzymes (**Figure 1**).<sup>[10]</sup> Up to now, no tungsten- or molybdenum-containing enzyme except nitrogenase has been found without this co-factor. Similar to Mo the biologically active oxidation states of tungsten range between +IV and +VI. Hence, one- and two-electron processes can be performed.<sup>[3]</sup>

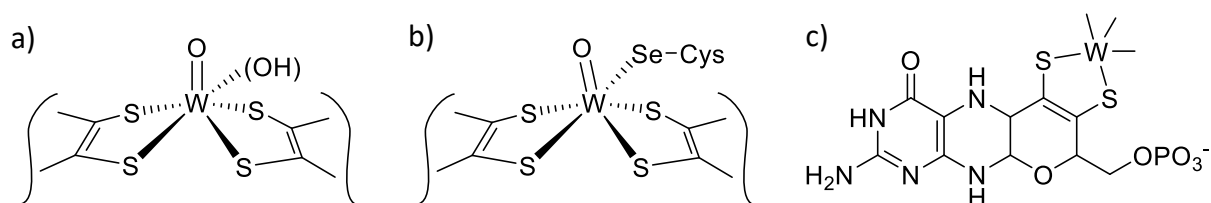
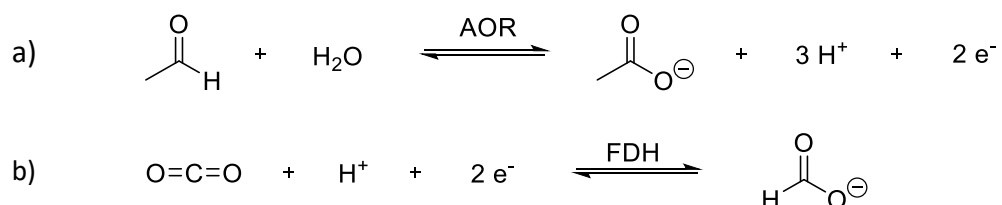


**Figure 1:** Active site structures of a) the aldehyde-ferredoxin oxidoreductase family and b) the formate dehydrogenase family; c) structure of the pterin co-factor of tungstoenzymes.

Tungstoenzymes are divided into three families. The aldehyde-ferredoxin oxidoreductase (AOR) family converts aldehydes to the corresponding carboxylic acids (**Scheme 1**). Members of the formate dehydrogenase (FDH) family catalyze the reversible oxidation of formate ( $\text{HCOO}^-$ ) to  $\text{CO}_2$ .<sup>[3,10]</sup>

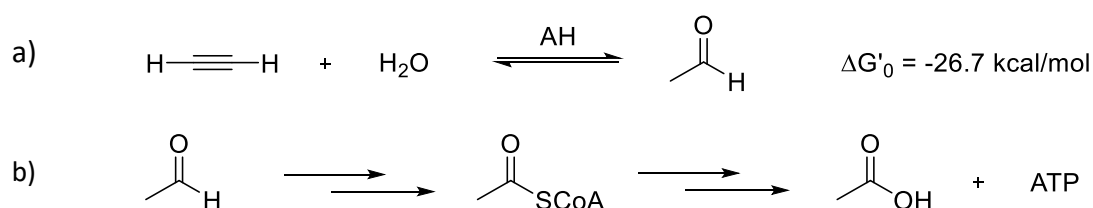


**Scheme 1:** a) Catalytic oxidation of aldehydes to carboxylic acid by AOR; b)  $\text{CO}_2$  conversion to formate catalyzed by FDH.

The third family consists of class II benzoyl-CoA reductase and acetylene hydratase.<sup>[3,11]</sup> The latter catalyzes the exergonic hydration of acetylene to acetaldehyde. In contrast to the other tungstoenzymes, it is therefore the only enzyme to catalyze a non-redox process.<sup>[3,10]</sup>

## 1.2. Acetylene hydratase

Acetylene hydratase (AH) was first isolated from the anaerobic, mesophilic bacterium *Pelobacter acetylenicus* by Schink in 1985.<sup>[12]</sup> Unlike other organisms, this bacterium was shown to be able to grow and live on acetylene as its only available carbon source.<sup>[12,13]</sup> In order to do so, acetaldehyde is subsequently converted into Acetyl-CoA and eventually acetic acid releasing ATP as the actual energy source (**Scheme 2**).<sup>[12]</sup>



**Scheme 2:** a) Acetylene hydration catalyzed by AH; b) metabolic conversion of acetaldehyde in the bacterium.

### 1.2.1. Structure of acetylene hydratase

Structurally, acetylene hydratase is similar to the DMSO reductase family of molybdoenzymes.<sup>[11,14]</sup> In contrast to other members of this family, AH exhibits a prominent rearrangement of two enzyme domains (residues 327-393) resulting in a subsequent shift of the loop region (residues 327-335) toward the surface of the protein.<sup>[15,16]</sup> This leads to the creation of a new entrance pathway for the substrate to the active site. The 6 - 8 Å wide and 17 Å deep channel ends in a hydrophobic pocket consisting of three isoleucine (Ile-14, Ile-113, Ile-142) and three tryptophane (Trp-179, Trp-293, Trp-472) amino acid residues. It is located directly above the tungsten coordination sphere and was found to form a perfectly suitable cavity for acetylene in computational docking experiments.<sup>[15]</sup>

The active site of the enzyme is composed of a tungsten-center coordinated by two dithiolene-moieties of the molybdopterin guanine dinucleotide co-factors ( $Q_{\text{MGD}}$  and  $P_{\text{MGD}}$ ) as well as a cysteine-residue (Cys-141).<sup>[15]</sup> In addition to this, a cubane-type iron-sulfur cluster, which is typical for all tungstoenzymes, was detected close to  $Q_{\text{MGD}}$  (**Figure 2a**).<sup>[15]</sup>

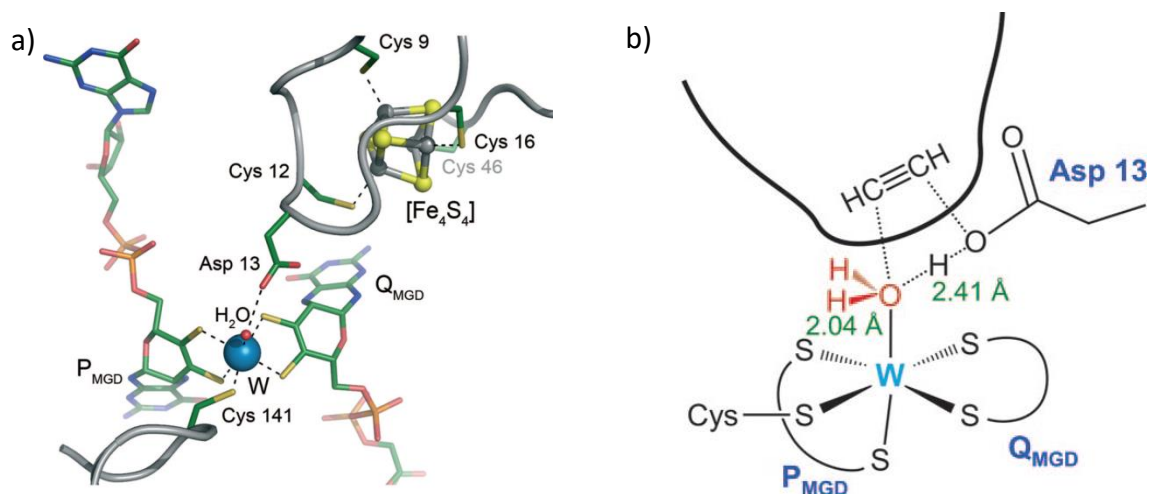


**Figure 2:** a) Crystal structure of the active site of AH;<sup>[16]</sup> b) schematic first coordination sphere of W featuring the adjacent Asp-13 amino acid residue and acetylene in the hydrophobic pocket.<sup>[15]</sup>

According to the crystal structure published in 2007, a sixth ligand is bound to tungsten via an oxygen-atom.<sup>[15]</sup> The W-O-distance of 2.04 Å indicates tightly coordinated water. However, crystal structures containing heavy scattering elements, such as tungsten, can be distorted by Fourier series termination effects blurring the true nature of the ligand.

Simulation of these effects resulted in a corrected metal-ligand-distance of 2.25 Å, which supports the idea of a coordinated water molecule (2.0 - 2.3 Å) over a hydroxo ligand (1.9 - 2.1 Å).<sup>[15]</sup>

The tungsten bound water molecule is also involved in a hydrogen-bond to Asp-13, whose protonation state is still disputed (**Figure 2b**).<sup>[15]</sup> The pK<sub>a</sub> value of aspartic acid in aqueous solution is 3.83, which suggests a deprotonated aspartate-residue in the active site. On the other hand, Asp-13 is buried deeply within the enzyme and is thus shielded from any protic solvent that could assist in the stabilization of the negative charge.<sup>[15,16]</sup> In order to determine the protonation state of Asp-13, Seiffert and co-workers derived titration curves from atomic charge calculations using density functional theory (DFT) and subsequent numerical solution of the Poisson-Boltzmann equation.<sup>[15]</sup> According to their results, the amino acid residues Glu-494 and Asp-13 remained in a fully protonated state between pH 0 and 24.<sup>[15]</sup> According to the authors, the major increase in the pK<sub>a</sub> value of Asp-13 results from desolvation effects inside the protein chain. Furthermore, it was postulated that proton affinity is increased by a positive inductive effect of the nearby iron-sulfur cluster, which increases the electron density at the Asp-13 through a connecting cysteine-residue.<sup>[15]</sup> Nevertheless, deprotonated Asp-13 cannot be ruled out completely. Liao and co-workers argue that two additional hydrogen-bonds to the peptide-bond of Cys-12 and Asp-13 as well as to Trp-179 lower the pK<sub>a</sub> value of Asp-13 significantly.<sup>[17]</sup> This idea was also supported by pK<sub>a</sub> predictions using the PROPKA method, which estimated a pK<sub>a</sub> value of 6.3 for Asp-13.<sup>[17]</sup>

### 1.2.2. Reactivity of acetylene hydratase

The enzymatic transformation of acetylene to acetaldehyde was found to be very substrate specific. Other molecules employing triple-bonds, such as cyanide, nitric oxide or carbon monoxide act as inhibitors to the enzyme while dinitrogen, isonitriles, ethylene, propyne and other derivatives of acetylene were not converted at all.<sup>[13,16]</sup>

Acetylene itself is mainly generated from fossil resources and not a very common substrate in biologic processes.<sup>[18]</sup> Apart from nitrogenase, which reduces acetylene to ethylene, acetylene hydratase is the only enzyme to accept acetylene as a substrate.<sup>[19–21]</sup>

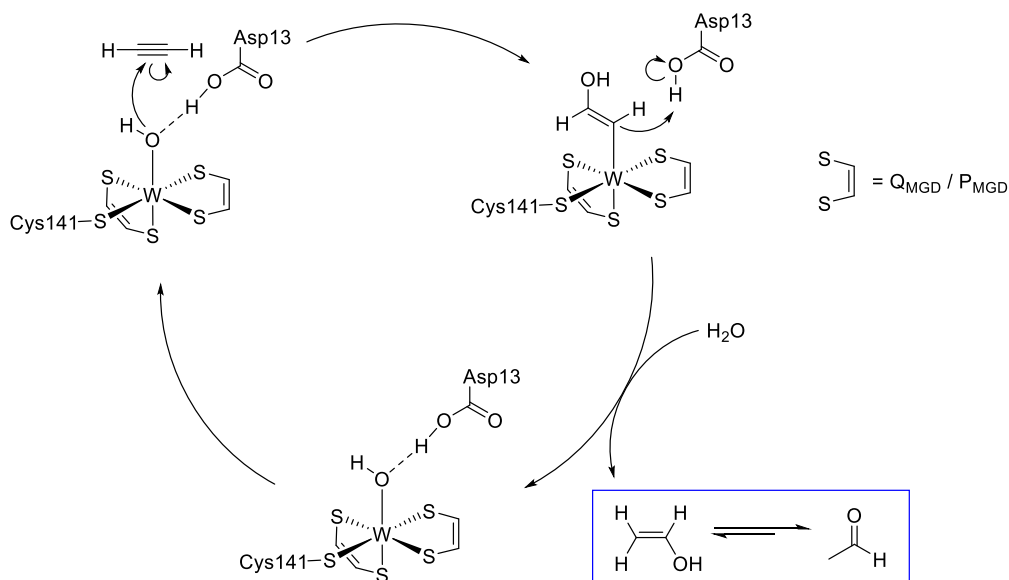
The cubane-type ferredoxin cluster close to the active site is usually used for electron-transfer processes in other tungstoenzymes.<sup>[10]</sup> Acetylene hydratase purified under N<sub>2</sub>/H<sub>2</sub>, on the other hand, is EPR silent.<sup>[14]</sup> Thus, catalysis is believed not to involve a redox-step at the metal-center or electron-transfer by the [4Fe-4S] cluster. Furthermore, when exposed to air, enzyme activity was only observed in the presence of strong reductants, such as Ti(II) citrate or dithionite.<sup>[14,15]</sup> This indicates O<sub>2</sub>-sensitivity of the W-center suggesting a W(IV) singlet state of the active species. When oxidized with hexacyanoferrate(III), an EPR signal assigned to W(V) emerged in the spectrum and disappeared again after addition of oxidant in excess.<sup>[14]</sup> It is therefore assumed that +IV is the active oxidation state of W in acetylene hydratase.

### 1.2.3. Mechanistic studies on acetylene hydratase

The reaction mechanism for the hydration of acetylene catalyzed by AH is still under discussion. So far, characterization of potential intermediates of the catalytic cycle by X-ray diffraction analysis failed. Single site-directed mutagenesis and biomimetic modeling of the enzyme have therefore become essential in providing experimental evidence.<sup>[22,23]</sup> Apart from that, various computational studies were published over the last 10 years.<sup>[17,24–26]</sup>

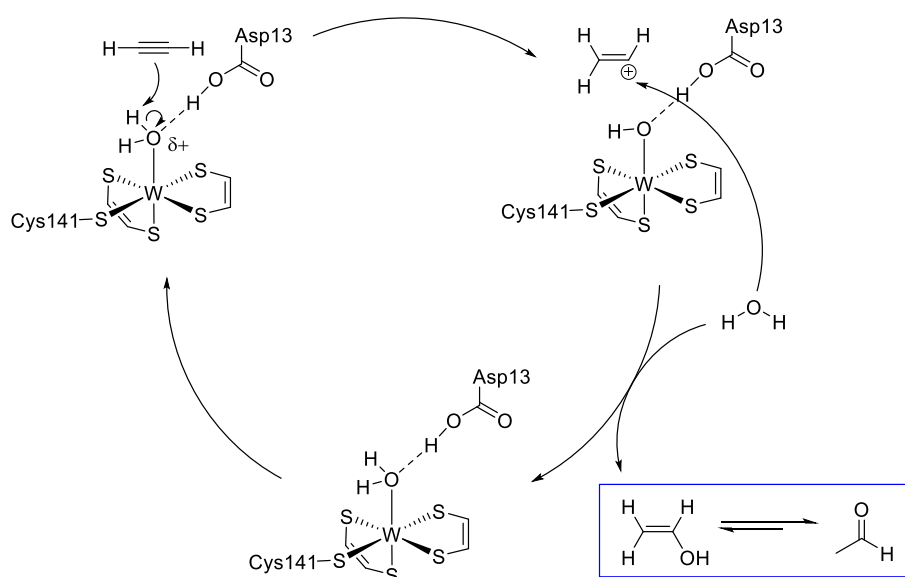
From single site-directed mutagenesis it is known that Asp-13, which forms a hydrogen-bond to the coordinated water molecule, plays an essential role in the mechanism.<sup>[22]</sup> When replaced against glutamic acid, which only differs from aspartic acid by one CH<sub>2</sub> unit in the amino acid side chain, acetylene conversion proceeded normally. However, when exchanged against more hydrophobic alanine, enzyme activity dropped to almost zero, indicating the necessity of a proton-donor/acceptor at this position of the active site.<sup>[22]</sup> Similar to this, Ile-142, which is part of the hydrophobic pocket at the end of the substrate channel, caused a significant decrease in catalytic activity when exchanged against alanine.<sup>[22]</sup> Since the hydrophobic pocket is handled as a potential substrate binding site, this result supports the idea of second-shell mechanisms. Two such approaches, in which acetylene is located in the hydrophobic pocket and has no bonding interaction with the metal, were proposed by Seiffert and co-workers.<sup>[15]</sup>

In their first mechanism, the oxygen-containing species coordinated to the tungsten-center was assumed to be a nucleophilic hydroxo ligand. It attacks acetylene to give a vinyl anion intermediate, which subsequently deprotonates the Asp-13-residue to form vinyl alcohol (Scheme 3).<sup>[15]</sup>



**Scheme 3:** Second-shell mechanism for AH proposing a nucleophilic attack on acetylene.

In the second mechanism, a water molecule coordinates to the tungsten-center and hydrogen-bonding towards Asp-13 results in a partially positive charge on the oxygen-atom (Scheme 4).

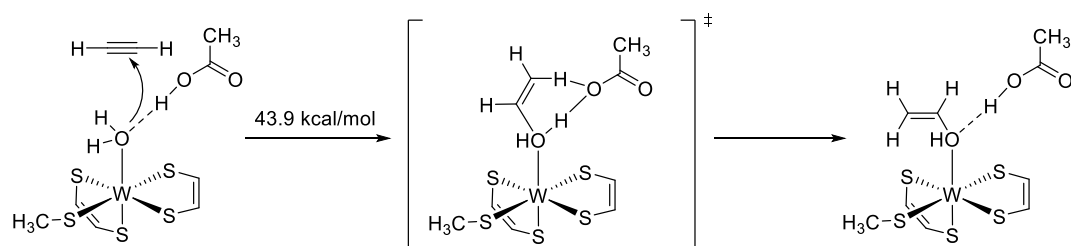


**Scheme 4:** Second-shell mechanism for AH proposing protonation of acetylene as the first step of the catalytic cycle and formation of a vinyl carbocation intermediate.

Protonation of acetylene to form a vinyl cation is supposed to proceed via a Markovnikov-type addition and believed to be facilitated by the increased acidity of the W-activated H<sub>2</sub>O ligand. Subsequently, the carbocation intermediate is attacked by a second water molecule and neutralized by the hydroxo ligand formed in the previous step.<sup>[15]</sup>

For both mechanisms, tautomerization of the enol to acetaldehyde is assumed to occur spontaneously.<sup>[15]</sup>

Seiffert and co-workers did not provide any energetics for these mechanisms. However, Vincent and co-workers calculated a concerted mechanism for a nucleophilic attack of water on acetylene (**Scheme 5**).<sup>[25]</sup> In this model dithiolene units were used to describe the pterin co-factors and Asp-13 and Cys-141 were represented by acetic acid and methyl thiolate, respectively.<sup>[25]</sup> Although the overall reaction was found to be exothermic, a high activation barrier of 43.9 kcal/mol rules out this mechanism.<sup>[25]</sup>



**Scheme 5:** Nucleophilic attack of tungsten bound water on acetylene forming a vinyl alcohol intermediate.<sup>[25]</sup>

For the second mechanism no computational data was presented to date. Yet, the formation of a vinyl carbocation intermediate is generally associated with formation enthalpies higher than 160 kcal/mol.<sup>[27]</sup> Furthermore, it is not assured that the catalytic function of acetylene hydratase is constricted to increased proton acidity since sulfuric acid is not a catalyst for acetylene hydration.<sup>[24,28]</sup>

The d<sup>2</sup> electron configuration of W(IV) necessary for enzyme activity as well as the discrimination of ethylene as a substrate cannot be explained by the proposed second shell mechanisms.<sup>[24]</sup> In case the substrate coordinates to the W-center, C<sub>2</sub>H<sub>4</sub> would only possess two electrons for ligand-donation. Acetylene, on the other hand, could donate up to four electrons into the d-orbitals of tungsten weakening the bonding interaction of the acetylene triple-bond considerably.<sup>[17]</sup> Further activation by the metal can be achieved by



$\pi$ -backdonation of d-electrons into one of the two anti-bonding  $\pi^*$ -orbitals of acetylene (**Figure 3**). W(IV)-complexes with side-on bound acetylene have furthermore been reported on various accounts and support the idea of such an intermediate.<sup>[23,29–34]</sup>

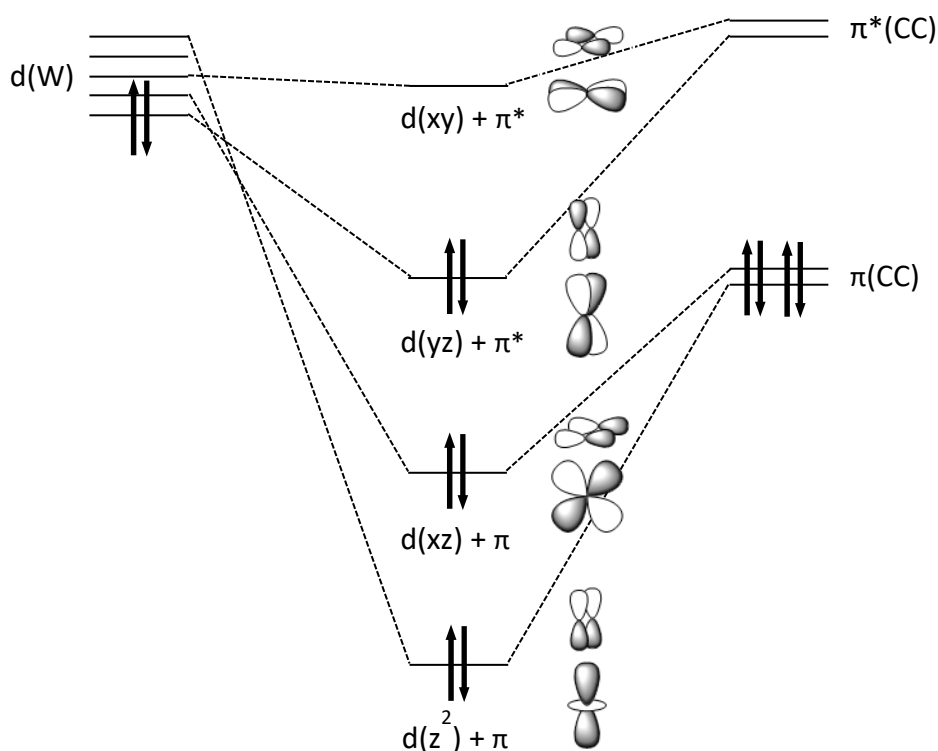
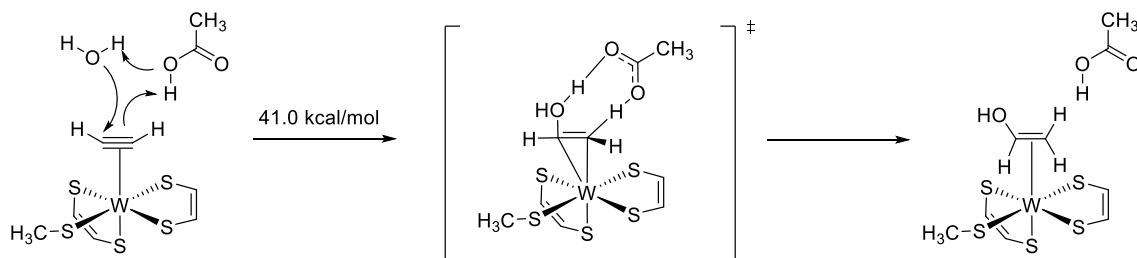


**Figure 3:** Possible C-C triple-bond activating interactions between W(IV) and side-on bound acetylene in the active site of acetylene hydratase.<sup>[17]</sup>

For a first-shell mechanism, in which acetylene binds to W prior to hydration, the coordinated water molecule is believed to be substituted. Calculations showed that this ligand exchange is exergonic by about 20 kcal/mol.<sup>[17,24,25]</sup> In principal, an associative or dissociative mechanism is possible for this process. Due to sterical overload, a dissociative mechanism is usually favored for complexes with a coordination number of six. On the other hand, the formally 14-electron structure of the active site is not electronically saturated and seven-coordinate tungsten species have been reported in literature.<sup>[35,36]</sup> Hence, both mechanisms have to be considered. Calculations showed that approximately 9 kcal/mol are required for the water molecule to fully dissociate.<sup>[17]</sup> Energy barriers for an associative mechanism are yet to be determined.

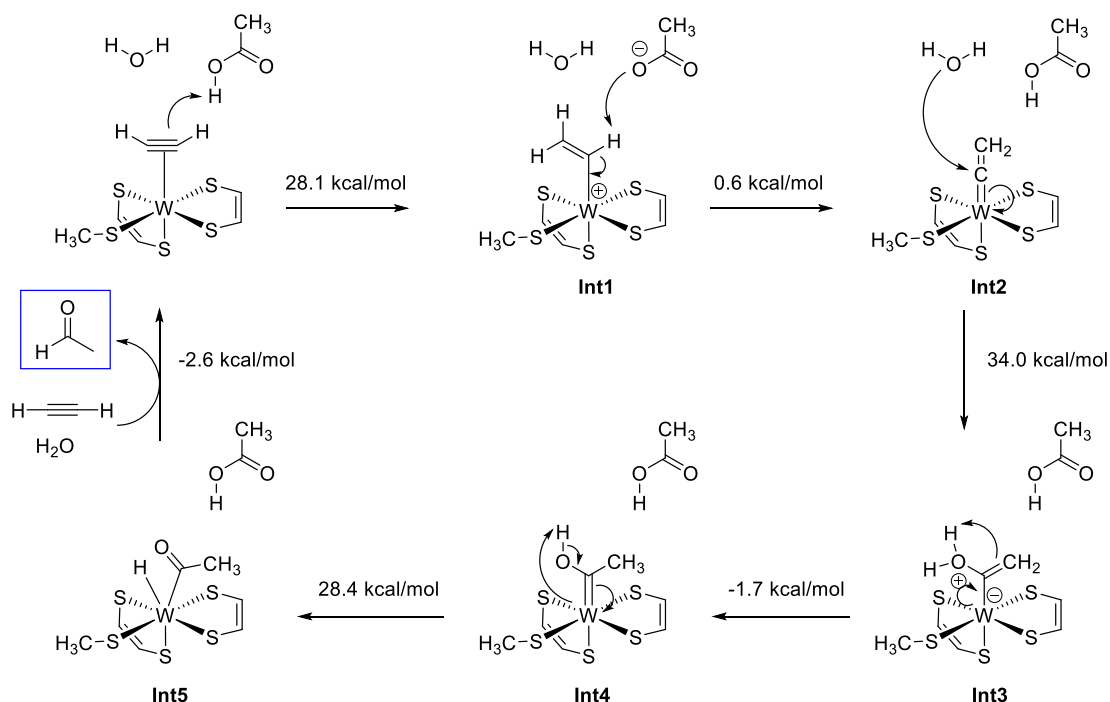
Following the idea of a first-shell mechanism, Bayse and co-workers suggested a nucleophilic attack of water on  $\eta^2$ -bound acetylene coupled with a proton transfer to form vinyl alcohol

**(Scheme 6).**<sup>[24]</sup> However, calculations for a concerted mechanism via a cyclic transition structure showed a high activation barrier of 41.0 kcal/mol, making this mechanism very unlikely.<sup>[25]</sup>



**Scheme 6:** First-shell mechanism for AH, in which water performs a nucleophilic attack on acetylene.<sup>[24,25]</sup>

An alternative route involving stable vinylidene and carbene intermediates was proposed in 2010 (**Scheme 7**).<sup>[25]</sup> The pterin co-factors were again modeled as dithiolene-units and Cys-141 as well as Asp-13 described as methyl thiolate and acetic acid, respectively.

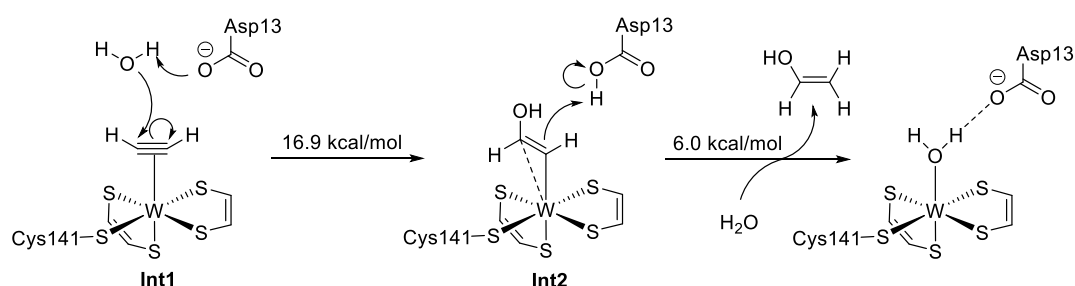


**Scheme 7:** First-shell mechanism for AH involving a vinylidene (Int2) and carbene (Int4) structure.<sup>[25]</sup>

In the first step of this mechanism,  $\eta^2$ -bound acetylene is protonated by Asp-13 leading to a partial oxidation of the metal-center. The transition state for this step is 28.1 kcal/mol higher in energy than the reactants and is rate-determining for the subsequent formation of the

vinylidene complex (**Int2**). The nucleophilic attack of water on the tungsten bound carbon-atom requires 34.0 kcal/mol and results in the high-energy intermediate **Int3**, which is 21.0 kcal/mol above the reactants. The following formation of the carbene complex (**Int4**) occurs spontaneously and is downhill in energy by 18.5 kcal/mol. In order to obtain acetaldehyde, it was suggested that **Int4** isomerizes via a hydride intermediate (**Int5**). The energy barrier for this step is 28.4 kcal/mol. Finally, the product is released by reductive elimination in an overall exergonic reaction by 31.2 kcal/mol.<sup>[25]</sup> Energy barriers for this approach are significantly lower than for previous routes, but still too high to qualify as a suitable mechanism for AH.

The most recent proposition of a catalytic cycle was postulated by Liao and co-workers (**Scheme 8**).<sup>[17]</sup> Unlike in all other mechanisms, Asp-13 is assumed to be deprotonated in the starting configuration of the enzyme. In DFT calculations, 116 atoms of the X-ray structure including several amino acid residues surrounding the metal-center were used and partially constrained during geometry optimizations.<sup>[17]</sup>



**Scheme 8:** First-shell mechanism for AH featuring an ionized Asp-13 amino acid residue that starts the catalytic cycle by deprotonation of the substituted water molecule.<sup>[17]</sup>

In the first step of this mechanism acetylene is substituted by water at the tungsten outer sphere. This was calculated to be an exothermic process by 5.4 kcal/mol.<sup>[17]</sup> Donation of up to four electrons from acetylene towards the metal and back-donation of two electrons into the  $\pi^*$ -orbital of acetylene results in a computed elongation of the C-C triple-bond from 1.21 Å to 1.30 Å. The released water is then deprotonated by Asp-13 and performs a nucleophilic attack on acetylene. The activation barrier for this step is 16.9 kcal/mol and therefore almost equal in energy to the vinyl anion intermediate **Int2**. According to the transition structure, the nucleophilic attack occurs almost perpendicularly to the W-acetylene plane and is believed to involve an empty  $\delta$ -like orbital formed by the

interaction of W d(xy) and the second  $\pi^*$ -orbital of acetylene. In the subsequent formation of the vinyl alcohol intermediate a proton is delivered by Asp-13. This step adds to the overall activation barrier of 23.0 kcal/mol and is rate-determining.<sup>[17]</sup> In agreement with previous mechanisms, tautomerization to acetaldehyde is suggested to occur either outside the active site or Asp-13-facilitated in the first coordination sphere of tungsten.<sup>[17]</sup>

In the following years, the mechanism was additionally studied at the quantum mechanical/molecular mechanical (QM/MM) level featuring QM regions of up to 157 atoms.<sup>[26,37]</sup> Surprisingly, the QM/MM system comprising the same 116 atoms, which were used in the QM-only approach, resulted in an unrealistic one-step energy profile with a very high energy barrier of 44.6 kcal/mol. This was attributed to the neglect of two adjacent diphosphate groups, which are believed to have a strong electrostatic influence. By addition of the diphosphate groups into the QM/MM model with 157 atoms the two-step mechanism was recovered and displayed an activation barrier of 16.7 kcal/mol.<sup>[26]</sup> However, in contrast to the QM-only approach, the nucleophilic attack is the rate-determining step for this model.

Despite reasonable energy barriers, the mechanism is not generally accepted by experts in the field. In a review paper published in 2016, the author once again raises doubts about deprotonated Asp-13 in the active site.<sup>[16]</sup> In order to further understand the reactivity of acetylene hydratase, the search for structural and functional biomimetic complexes is therefore of major importance.

#### 1.2.4. Biomimetic models of acetylene hydratase

Based on the EPR results of acetylene hydratase, compounds with a W(IV)-center and biologically relevant S- and N-donating ligands qualify as biomimetic models of the enzyme. The three structural models reported so far additionally employ a side-on bound acetylene molecule to mimic potential intermediates of a first-shell mechanistic proposal (**Figure 4**).<sup>[23,30,33]</sup> The complex  $[\text{WO}(\text{C}_2\text{H}_2)(\text{S}_2\text{CNR}_2)_2]$  (R = Me, Et) was reported by Templeton and co-workers in 1981.<sup>[30]</sup> The bonding in this complex is representative for all model compounds of AH and was described as a combination of ligand donation and  $\pi$ -backdonation from the W-center.<sup>[30,33]</sup>

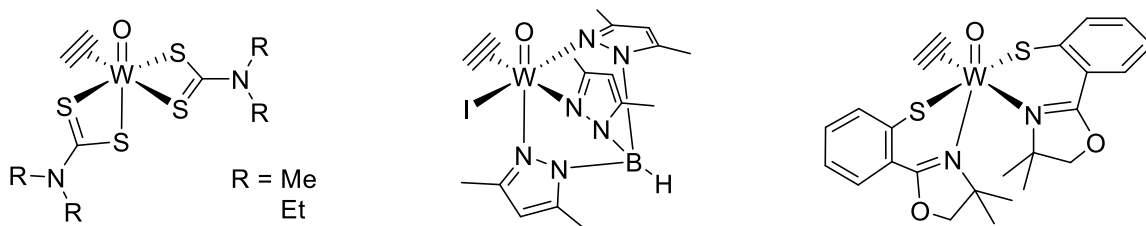


**Figure 4:** Structural model compounds of acetylene hydratase.

The oxygen lone-pairs of the terminal oxo-group interact with the W  $d(xz/yz)$ -orbitals via  $\pi$ -donation (**Figure 5**). Acetylene is oriented perpendicular to the oxo-ligand and can therefore donate two electrons into the W  $d(x^2-y^2)$ -orbital as well as two electrons into the W  $d(yz)$ -orbital creating a 3-center-4-electron (3c-4e) bond with the O=W-moiety.<sup>[30]</sup> At the same time  $\pi$ -backdonation occurs from the filled W  $d(xy)$ -orbital into the planar anti-bonding  $\pi^*$ -orbital of acetylene.<sup>[30]</sup> An alternative parallel ligand arrangement between the oxo-group and acetylene is considered unfavorable since the metal electrons would be located in the W  $d(yz)$ -orbital preventing the stabilizing formation of the 3c-4e-bond.<sup>[30,33]</sup>

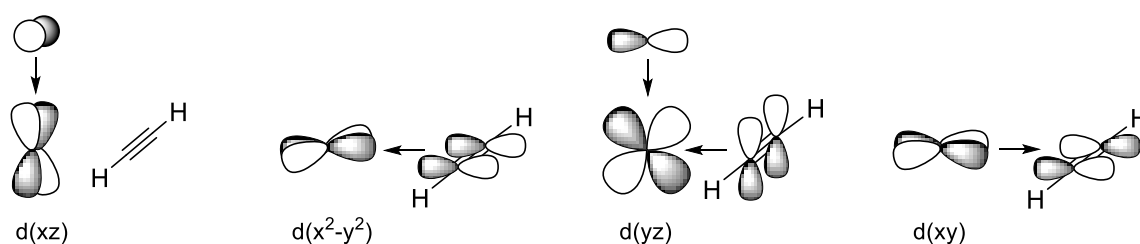
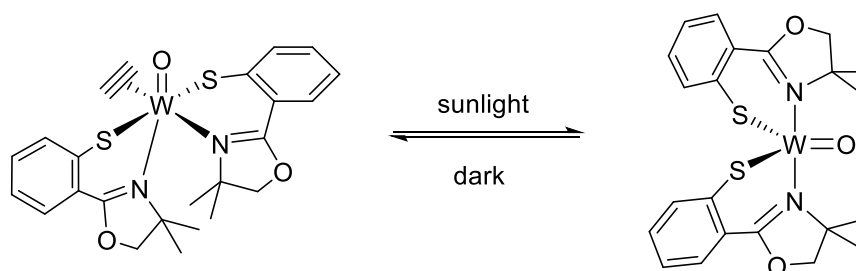


**Figure 5:** Metal-ligand interactions in biomimetic W-complexes of acetylene hydratase.

The historically second biomimetic model of AH is the complex  $[\text{WO}(\text{C}_2\text{H}_2)\text{Tp}^*]\text{I}$ , which employs the tridentate, facially coordinating scorpionate ligand hydridotris-(3,5-dimethylpyrazolyl)borate ( $\text{Tp}^*$ ).<sup>[33]</sup> The pyrazolyl N-donors of this ligand are usually used to mimic His-residues.<sup>[38,39]</sup> For the modeling of more diverse coordination spheres, such as the sulfur-rich environment of acetylene hydratase, the  $\text{N}_3$ -donor can be modified creating so called heteroscorpionate ligands.<sup>[40,41]</sup> Although a biomimetic model complex of this type has not been reported for AH yet, a ligand with a mixed NS-donor motif was beneficial for the preparation of the third structural model complex  $[\text{WO}(\text{C}_2\text{H}_2)(\text{S-Phoz})_2]$  (S-Phoz = 2-(4',4'-dimethyloxazolin-2'-yl)thiophenolate).<sup>[23]</sup> In contrast to the other two compounds, this system showed reversible release and coordination of acetylene under light exposure (**Scheme 9**). The  $^1\text{H}$  NMR study of this complex and its dimethylacetylene- and diphenylacetylene-analogs furthermore revealed a correlation between the metal-alkyne

interaction and the rate of the photoinduced alkyne release.<sup>[31]</sup> According to the authors, the electron-withdrawing nature of the phenyl groups in  $C_2Ph_2$  are believed to increase  $\pi$ -backdonation, binding the alkyne more strongly to the W-center. The  $C_2H_2$ - and  $C_2Me_2$ -complexes, on the other hand, seem to have more  $\eta^2$ -adduct character resulting in a faster photochemical release of the alkynes.<sup>[31]</sup>



**Scheme 9:** Reversible photoinduced alkyne release of the complex  $[WO(C_2H_2)(S-Phoz)_2]$ .<sup>[31]</sup>

The only functional model of acetylene hydratase was reported by the Sarkar group in 1997 (**Figure 6**).<sup>[42,43]</sup> The complex  $[Et_4N]_2[WO(mnt)_2]$  ( $mnt^{2-} = 1,2$ -dicyanoethylenedithiolate) was originally designed as a biomimetic model of aldehyde ferredoxin oxidoreductase, but performed approximately nine turnovers of acetylene hydration as well.<sup>[42,43]</sup> However, adduct formation with acetylene was not observed by spectroscopic techniques under ambient conditions.

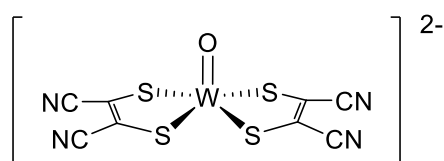


**Figure 6:** Structure of the proposed functional model complex of acetylene hydratase.

In 2017, Schreyer and Hintermann reported that their attempt to reproduce the catalytic activity of this complex failed.<sup>[44]</sup> They furthermore pointed out inadequacies in the analytical techniques applied by Yadav and co-workers and concluded that acetone, which is used as a stabilizer in acetylene pressure bottles, was possibly mistaken for acetaldehyde as the reaction product.<sup>[44]</sup> The complex  $[Et_4N]_2[WO(mnt)_2]$  is therefore no longer considered a biomimetic model for AH and the search for structural and functional model compounds is still of major interest.

## 2. ELECTRONIC ABSORPTION SPECTROSCOPY

In electronic absorption spectroscopy, electromagnetic radiation is used to promote electrons from the electronic ground state into partially or unoccupied orbitals of a molecule (**Figure 7**).<sup>[45,46]</sup> The energy required for such a transition is characteristic for each compound and provides information about the electronic structure of the probed environment.

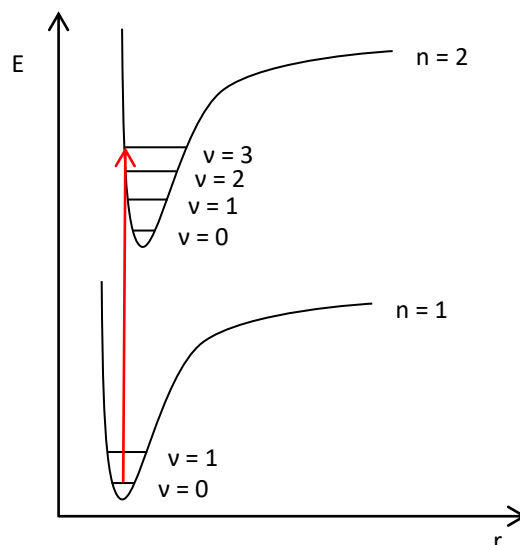


**Figure 7:** Electronic transition between ground and excited state of a molecule with  $n$  = principal quantum number describing the electron shell of the electron and  $v$  = vibrational levels within each potential well.

In order to excite an electron, the energy of the absorbed photon has to match the energy gap  $\Delta E$  between the energy levels involved in the transition.<sup>[45]</sup> This energy is directly related to the frequency  $\nu$  and the wavelength  $\lambda$  of the applied electromagnetic radiation via eq. 1,

$$\Delta E = h\nu = \frac{hc}{\lambda} \quad (1)$$

in which  $h$  represents Planck's constant and  $c$  the speed of light.<sup>[45,46]</sup>

The absorption of electromagnetic radiation at specific wavelengths can therefore be used to experimentally identify the nature of electronic transitions. Inherently, the least energy is required for valence electron jumps from the highest occupied molecular orbitals (HOMOs) to the lowest unoccupied molecular orbitals (LUMOs). Such transitions are often observed in optical spectroscopy using UV or visible light.<sup>[47,48]</sup> Larger energy gaps are also accessible

experimentally, but require higher-energy radiation. In X-ray absorption spectroscopy, for instance, X-rays are used to promote core electrons into high energy orbitals or the energy continuum.<sup>[49,50]</sup>

While the wavelength, at which the transition occurs, is indicative of the energy gap between the molecular orbitals (MOs), additional information about the type of transition can be gained from the intensity of the absorption feature. Beer's law shows the correlation between the percentage of absorbed radiation and the extinction coefficient  $\epsilon$  of the tested compound (eq. 2).<sup>[45,46]</sup>

$$A = \log \frac{I_0}{I} = \epsilon cd \quad (2)$$

The concentration  $c$  as well as the distance  $d$ , which describes the path length through the sample, can be regulated by sample preparation and experimental setup. For constant values of  $c$  and  $d$ , the absorption  $A$  is therefore defined by the logarithmic ratio between incident ( $I_0$ ) and transmitted ( $I$ ) radiation while the extinction coefficient  $\epsilon$  determines signal intensity. This is of interest since the magnitude of  $\epsilon$  can be connected to spectroscopic selection rules, which classify transitions as quantum mechanically allowed or forbidden.<sup>[45]</sup>

### 2.1. Spectroscopic selection rules

From a quantum mechanical point of view, the "allowedness" of a transition and therefore its signal intensity depends on the probability of a transition.<sup>[45]</sup> This dimension is proportional to the value of the transition moment integral (eq. 3),

$$M = \int \psi^* \hat{r} \psi d\tau \quad (3)$$

where  $\psi$  is the wave function in the ground state,  $\psi^*$  represents the wave function in the excited state and  $\hat{r}$  describes the transition moment operator according to the applied field.<sup>[45]</sup>



The transition moment integral  $M$  can be divided into a vibrational, an orbital and a spin component, which set the basis for the selection rules for transitions (eq. 4).<sup>[45]</sup>

$$M = \underbrace{\int \psi_v^* \psi_v d\tau_n}_{\text{Franck-Condon factor}} \underbrace{\int \psi_e^* \hat{r} \psi_e d\tau_e}_{\text{orbital selection integral}} \underbrace{\int \psi_s^* \psi_s d\tau_s}_{\text{spin selection integral}} \quad (4)$$

Each of the integrals describes the overlap of wave functions in electronic ground ( $\psi$ ) and excited ( $\psi^*$ ) state. By definition the transition moment operator  $\hat{r}$  acts on the orbital component of the wave function ( $\psi_e$ ) only. While the orbital selection integral extends over electron coordinates  $e$ , the vibrational and spin selection integrals rely on nuclear coordinates  $n$  and spin  $s$ , respectively.<sup>[45]</sup>

For an allowed transition,  $M$  is non-zero. However, not all selection integrals contribute equally to signal intensity. Some selection rules have a larger influence on  $M$  than others with the spin selection rule leading to the lowest signal intensities if not followed.<sup>[45]</sup>

For spin-allowed transitions, the spin-selection integral  $\int \psi_s^* \psi_s d\tau_s$  is non-zero. This is only the case if the multiplicities ( $2S + 1$ ) of the ground and the excited state are identical. Thus, singlet  $\rightarrow$  singlet or doublet  $\rightarrow$  doublet transitions are allowed whereas transitions, such as singlet  $\rightarrow$  triplet, are spin-forbidden.<sup>[45]</sup>

In orbital-allowed transitions, the orbital-selection integral  $\int \psi_e^* \hat{r} \psi_e d\tau_e$  has to be non-zero. Instead of calculating the exact value of the integral, it is sufficient to determine the symmetries of its individual components and form the triple direct product  $\Gamma(\psi_e^*) \times \Gamma(\hat{r}) \times \Gamma(\psi_e)$ . If the resulting term contains the totally symmetric irreducible representation of the molecule's point group, the transition is considered orbital-allowed.<sup>[45]</sup>

The Franck-Condon factor  $\int \psi_v^* \psi_v d\tau_n$  represents the vibrational component of the transition moment integral and is non-zero if the vibrational wave functions are not orthogonal. In general, this integral is only taken into account if a transition is orbital-forbidden. In this case, the wave function is described as a combination of electronic and vibrational contributions. If the integral for such a vibronic interaction  $\int \psi_e^* \psi_v^* \hat{r} \psi_e \psi_v d\tau_{en}$  is non-zero, the intensity of the orbital-forbidden transition is increased.<sup>[45]</sup>

Experimentally, the “allowedness” of electronic transitions correlates with the magnitude of the extinction coefficient  $\epsilon$ . Since the spin selection rule has the largest influence on the signal intensity,  $\epsilon$  values of spin-forbidden transitions are lowest (**Table 1**). Spin-allowed, but orbital-forbidden transitions are slightly more likely. They show extinction coefficients in the range of  $10^0$  and  $10^3 \text{ M}^{-1}\text{cm}^{-1}$ , which can be further magnified by vibronic coupling. The highest intensities are to be expected for spin- and orbital-allowed transitions with  $\epsilon$  values between  $10^3 - 10^5 \text{ M}^{-1}\text{cm}^{-1}$ .<sup>[45,51–54]</sup>

**Table 1:** Intensities of electronic transitions based on spin and orbital selection rules.<sup>[45]</sup>

Spin-allowed	Orbital-allowed	Vibronically-allowed	Approximate $\epsilon$ values [ $\text{M}^{-1}\text{cm}^{-1}$ ]
✗			$10^{-5} - 10^0$
✓	✗		$10^0 - 10^3$
✓	✗	✓	$10^0 - 10^3$
✓	✓		$10^3 - 10^5$

In electronic spectroscopy, such as UV-vis or X-ray absorption spectroscopy, absorption features with high intensity usually result from electric dipole induced electron jumps. Additionally, electrons can be promoted by other fields, such as electric quadrupoles. Depending on the applied field, the symmetry of the transition moment operator can change the orbital allowedness of the transition.<sup>[45]</sup> In an octahedral environment, for instance, the orbital integral is zero if the triple direct product  $\Gamma(\psi_e^*) \times \Gamma(\hat{r}) \times \Gamma(\psi_e)$  is anti-symmetric (ungerade). Considering that the dipole moment operator transforms as x, y, z and the quadrupole moment operator as the quadratic combinations of x, y and z, the orbital allowedness in the octahedral point group  $O_h$  only depends on the parity of the electron-donating and accepting orbitals (**Table 2**). In case the orbitals involved in the transition have the same parity, the transition is dipole-forbidden, but quadrupole-allowed. Dipole-allowed and quadrupole-forbidden transitions, on the other hand, occur between orbitals with unlike parities.<sup>[55]</sup>

**Table 2:** Orbital selection rules in an octahedral environment.

Transition	$\Delta n^a$	$\Delta l^b$	Signal intensity
Dipole-allowed	arbitrary	$\pm 1$	strong
Quadrupole-allowed	arbitrary	$0, \pm 2$	weak

<sup>a</sup> n = principal quantum number describing the electron shell; <sup>b</sup> l = azimuthal quantum number describing the atomic orbital.

Although quadrupole-induced transitions are quantum-mechanically allowed, signals for such transitions are difficult to observe unless the intensities are enhanced through vibronic coupling.<sup>[55]</sup>

## 2.2. X-ray absorption spectroscopy (XAS)

In X-ray absorption spectroscopy (XAS), transitions between the electronic ground state and excited states are observed. The radiation for such processes is usually derived from synchrotron sources and is element specific.<sup>[50]</sup> This is particularly useful in the study of large biological systems, such as metalloenzymes. In contrast to other analytical methods, XAS facilitates the investigation of the local first coordination sphere structure of the metal-site without absorption interferences of the surrounding protein matrix, solvent molecules or atmosphere.<sup>[49,56,57]</sup> XAS is also not limited to specific sample states. Powders and solutions, including frozen solutions, can be measured providing the opportunity to run kinetic studies of enzymes and trap catalytic intermediates.<sup>[58–61]</sup>

Nevertheless, the probing of simple metal compounds with known crystallographic structure is still of importance, and is often used as a reference to understand the electronic environment of enzymes.<sup>[62,63]</sup> Furthermore, it provides data on many chemical characteristics, such as complex bonding interactions and oxidation states, which can be difficult to determine using other techniques.<sup>[50]</sup>

### 2.2.1. XAS spectra

XAS spectra can be divided into two energy regions. The low energy region is called X-ray absorption near-edge structure (XANES) whereas the high energy region is referred to as extended X-ray absorption fine structure (EXAFS).<sup>[64]</sup> In both cases the energy of the incoming X-ray photon is used to promote core electrons. In the XANES region of the spectrum, core electrons are promoted into partially or unoccupied orbitals. In EXAFS, the electron is ejected into the energy continuum (**Figure 8**).<sup>[50]</sup> Metal K-edge and L-edge spectroscopy are distinguished by the nature of the orbital from which the electron

originated. K-edge XAS describes the excitation of 1s electrons and is common for many elements, such as first and second row transition metals.<sup>[65,66]</sup> L-edge spectroscopy is less common and usually applied to investigate elements with unattainable ionization energies of the first shell electrons. Therefore, transitions from the 2s orbital are induced in L1-edge XAS whereas in L2- and L3-edge XAS the electron is ejected from orbitals that produce  $2p_{1/2}$  and  $2p_{3/2}$  final states, respectively.<sup>[67]</sup>

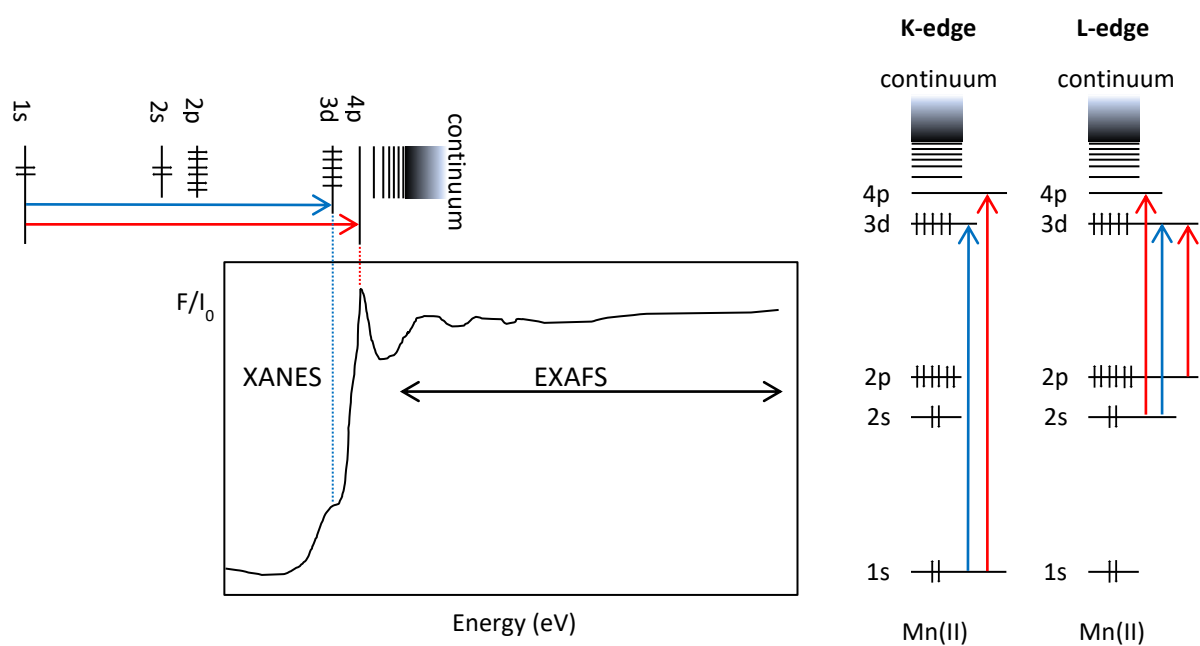


**Figure 8:** Display of a Mn K-edge XAS spectrum in consideration of possible X-ray induced transitions (red: dipole-allowed transitions; blue: dipole-forbidden transitions).<sup>[50]</sup>

### 2.2.2. XANES

In the XANES region, transitions of core electrons into partially occupied or unoccupied high energy orbitals are investigated. The corresponding absorption increases are called absorption edges. Among these, the most intense edge is also referred to as the rising edge and usually results from a dipole-allowed transition, such as  $1s \rightarrow np$  for metal K-edge XAS.<sup>[50]</sup>

The rising edge also correlates to the effective nuclear charge  $Z^{\text{eff}}$  of the absorbing atom.<sup>[68,69]</sup> This is particularly interesting in regard to the determination of physical oxidation

states. In oxidized species the ejected electron experiences less shielding by inner electrons and more attraction towards the nucleus, which increases the transition energy. In a series of compounds with different nuclear charge, the position of the rising edge therefore shifts toward higher energies as the oxidation state of the probed atom increases.<sup>[50]</sup>

Apart from the rising edge, additional absorption features can be observed in the metal K-edge or L1-edge XANES if the probed compounds display a partially occupied or unoccupied d-manifold.<sup>[70,71]</sup> These absorption features occur at lower energy than the rising edge and, for K-edge spectroscopy, result from  $1s \rightarrow (n-1)d$  transitions, which are quadrupole-allowed, but dipole-forbidden. The intensity of these pre-edge features is about two orders of magnitude lower than the absorption increase of the  $1s \rightarrow np$  transition.<sup>[71]</sup> However, in many compounds, especially transition metal complexes, the intensities of pre-edge features are enhanced by vibrational or structural distortion of the complex symmetry. Low symmetry distortions that remove inversion symmetry provide an intensity gaining mechanism for  $1s \rightarrow np$  transitions, which gain their allowedness through metal d-p mixing. In the XAS spectrum the intensity of the dipole-forbidden  $s \rightarrow (n-1)d$  transitions is therefore increased proportional to the amount of p-character present in the accepting orbital.<sup>[67,68]</sup> The more d-p mixing occurs in the complex, the higher the intensity of the pre-edge feature.

### 2.2.3. EXAFS

In the EXAFS region, core electrons are emitted into the energy continuum. For such an event, the absorbed energy ( $E_{hv}$ ) has to be higher than the ionization energy ( $E_{ion}$ ) of the probed atom. Excess energy is transformed into translational kinetic energy ( $E_{kin}$ ) of the released core electron (eq. 5).<sup>[50,72]</sup>

$$E_{kin} = E_{hv} - E_{ion} \quad (5)$$

The energy of the incoming X-ray radiation modulates the wavelength of the photoelectron, which is backscattered by atoms within 4-5 Å of the ionized center.<sup>[50]</sup> Photoelectron and backscattered waves can either be in constructive or destructive interference. This changes the absorption coefficients, which determine signal intensities in the EXAFS region. In case of

constructive interference, the absorption coefficient is enhanced. A decrease in absorption, on the other hand, is observed if the waves are out of phase (**Figure 9**).<sup>[50]</sup> The resulting EXAFS modulation can be generally described by the oscillatory contribution of the absorption coefficient  $\chi(k)$ , which is defined as the observed absorption coefficient  $\mu(k)$  minus the absorption coefficient of the free atom  $\mu_0(k)$ , normalized by  $\mu_0(k)$  (eq. 6).<sup>[50]</sup>

$$\chi(k) = \frac{\mu(k) - \mu_0(k)}{\mu_0(k)} \quad (6)$$

A quantitative expression for  $\chi(k)$  contains information about the number and electron density of backscattering atoms, as well as their distance to the absorbing atom. In organometallic and bioinorganic chemistry, EXAFS used in combination with XANES can determine coordination numbers, identity of ligands and precise bond lengths if single crystals are not available.<sup>[70]</sup>

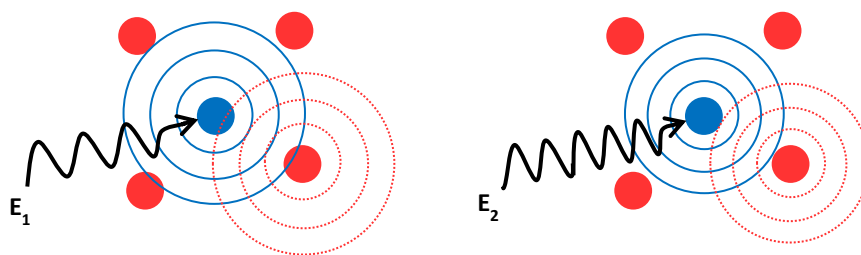


**Figure 9:** Interference patterns of photoelectron (blue) and backscattered (red) waves at different energies of the incoming x-ray radiation ( $E_2 > E_1$ ).<sup>[50]</sup>

#### 2.2.4. Ligand K-edge XAS

In coordination chemistry, not only core electrons of the metal-center, but also of ligand atoms are often excited. The resulting spectra contain a XANES and EXAFS region analogous to metal XAS. Common elements that are probed using this technique are Cl and S, which can interact with the d-orbitals of transition metals via  $\sigma$ - and  $\pi$ -bonding interactions.<sup>[73,74]</sup> The metal-ligand MOs exhibit metal d- and ligand p-character that are dependent on the relative energy levels of the respective atomic orbitals and their overlap (**Figure 10**). In general, the smaller the energy difference between the metal (M) and ligand (L) orbitals, the more mixing between the two components occurs. For donor ligands, this increases the

M d-character in the bonding wave function as well as the L p-character in the anti-bonding MO. Transitions into these M d- L p-mixed orbitals  $\varphi^*$  are observed in the XANES region of ligand K-edge XAS.<sup>[74]</sup>

$$\varphi^* = (1 - \alpha^2)^{1/2} |M d\rangle - \alpha |L p\rangle \quad (7)$$

In eq. 7,  $\alpha^2$  describes the degree of L p-character in the predominantly metal-based acceptor orbital. Since the transition from L 1s into L 3p is dipole-allowed, the intensity of the absorption edge for  $L 1s \rightarrow \varphi^*$  is proportional to the L p-character in the orbital. The intensity  $D_0$  is therefore described as the intensity of the purely L-centered transition  $I(L 1s \rightarrow L 3p)$  weighted by the M-L covalency  $\alpha^2$ , which is consistent with the amount of L p-character in  $\varphi^*$  (eq.8).<sup>[75]</sup>

$$D_0(L 1s \rightarrow \varphi^*) = const. |\langle L 1s | \hat{r} | \varphi^* \rangle|^2 = \alpha^2 \times I(L 1s \rightarrow L 3p) \quad (8)$$

In order to quantitate  $\alpha^2$ , the transition dipole integral  $\langle L 1s | \hat{r} | \varphi^* \rangle$  for  $L 1s \rightarrow L 3p$  has to be determined.<sup>[75]</sup> The experimental covalencies can also be correlated to the results of DFT calculations. For a good fit, the oxidation and spin states of the metal have to be met. Therefore, L K-edge XAS is often used to complement the information gained by metal XAS.<sup>[76,77]</sup>

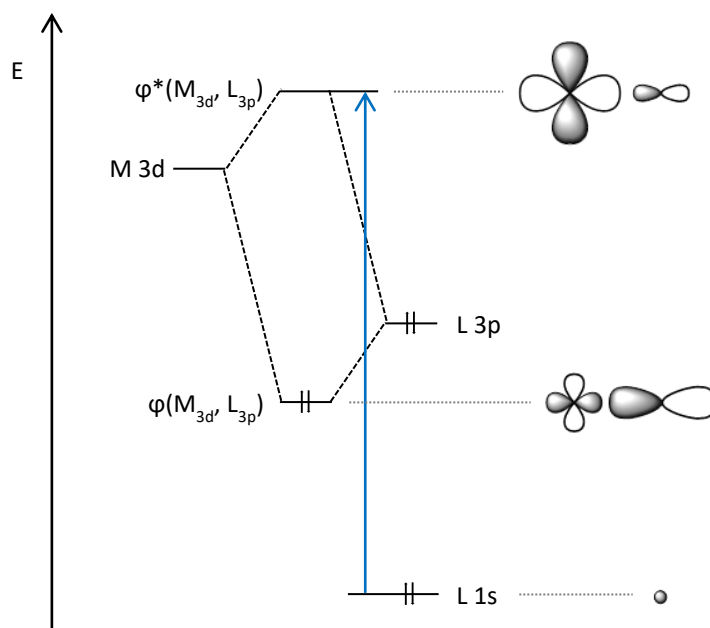
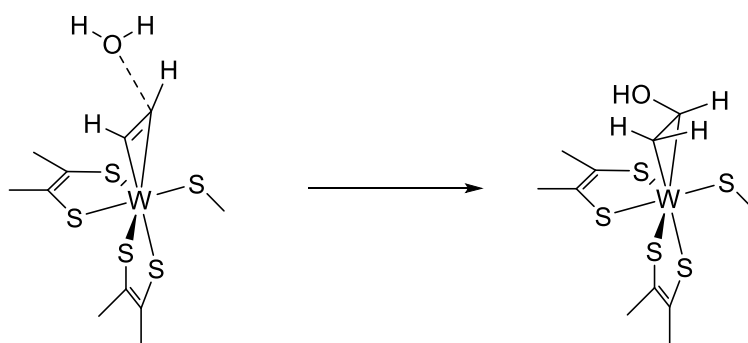


**Figure 10:** Transition of the ligand 1s electron into a metal d- ligand p-mixed orbital. The size of the orbital lobes represents the degree of M d- and L p-character.

## AIM OF THIS THESIS

The reaction mechanism of acetylene hydratase has been a topic of renewed interest ever since the crystal structure of the enzyme was reported in 2007.<sup>[15]</sup> In theoretical calculations only one proposed mechanism displayed reasonable activation barriers, but was not accepted consensually in the field.<sup>[16,17]</sup> Still disputed are the binding site of the substrate as well as the protonation state of Asp-13.<sup>[16]</sup> While the crystallographic data favors a second-shell mechanism, in which acetylene is held in a hydrophobic cavity and attacked by a W-bound water molecule, the  $d^2$  electron configuration of W in the active site is suitable for activation of acetylene by  $\pi$ -backdonation. The latter supports the idea of a first-shell mechanism, in which the interaction between metal and substrate should facilitate the reaction significantly. Thus, a computational study comparing the energetic profiles of the uncatalyzed vs. the metal-assisted hydration of acetylene should provide insight into this matter (**Scheme 10**).



**Scheme 10:** Proposed reaction scheme for the computational study on the W-assisted hydration of acetylene.

Although computational studies provide valuable information for the determination of enzymatic reaction mechanisms, experimental data is often required to prove the suggested reactivity. In case of acetylene hydratase various biomimetic complexes that count as structural models exist.<sup>[23,30,33]</sup> The proposal of the only functional model, which was reported by the Sarkar-group in 1997, comprised inadequacies in the applied analytical techniques and was eventually revoked in 2017.<sup>[42-44]</sup> The search for a structural and functional model compound for acetylene hydratase is therefore still of major interest.



The ligand (2-dimethylethanethiol)-bis(3,5-dimethylpyrazol) methane (L3SH), which is isoelectronic to the well-established scorpionate ligand Tp<sup>\*</sup>, but contains a N<sub>2</sub>S-donor motif, was already used to prepare bio-inspired Zn- and Mo-complexes (**Figure 11**).<sup>[78–83]</sup> A mixed NS-donor set was furthermore suitable for the most recent biomimetic model of AH.<sup>[23,31]</sup> Therefore, a new model compound for acetylene hydrates employing the L3S-ligand should be prepared.

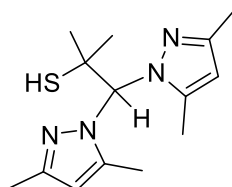
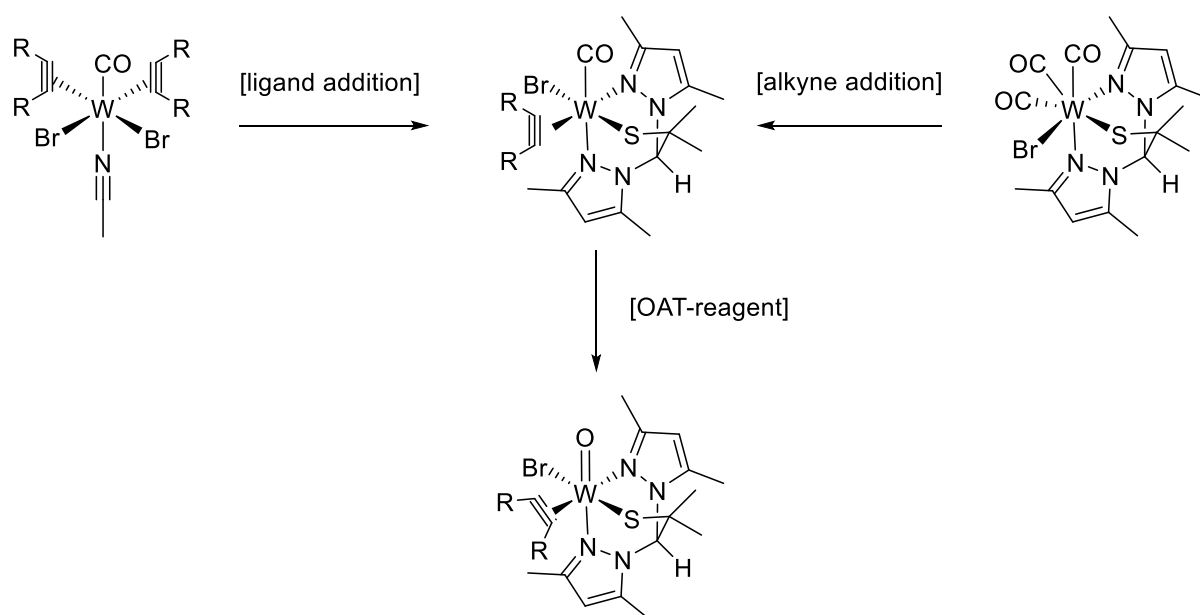


**Figure 11:** Structure of the heteroscorpionate, tridentate ligand L3SH.

The selected approach towards such a model complex proceeds via the preparation of a carbonyl-containing W(II)-precursor of the type [W(CO)(C<sub>2</sub>R<sub>2</sub>)(L3S)Br] (R = Ph, Me, H). Since dimethylacetylene (C<sub>2</sub>Me<sub>2</sub>) and diphenylacetylene (C<sub>2</sub>Ph<sub>2</sub>) are assumed to be easier to handle than gaseous C<sub>2</sub>H<sub>2</sub>, these alkynes should be investigated in addition to the natural substrate. In principal, two routes referred to as the ligand- and the alkyne-addition method are applicable to obtain the desired compound (**Scheme 11**).



**Scheme 11:** Synthetic approach for the preparation of alkyne coordinated complexes of the type [WO(C<sub>2</sub>R<sub>2</sub>)(L3S)Br] (R = H, Me, Ph).

In order to obtain complexes in the physiologically relevant oxidation state +IV, subsequent oxidation of the W(II)-precursors to complexes of the type  $[\text{WO}(\text{C}_2\text{R}_2)(\text{L}_3\text{S})\text{Br}]$  ( $\text{R} = \text{Ph}, \text{Me}, \text{H}$ ) is required. Therefore, oxygen atom transfer (OAT) reagents, such as PyNO, mCPBA and DMDO should be studied in regard to their oxidation abilities. The spectroscopic behavior as well as the reactivity of the resulting complexes should then be determined and implications regarding the mechanism of acetylene hydratase discussed.

Since alkynes can act as two- or four-electron-donors, the formal oxidation state of W in complexes of the form  $[\text{WO}(\text{C}_2\text{R}_2)\text{L}_2]$  is defined as either +IV or +VI.<sup>[84]</sup> In order to better mimic the active site of enzyme, it is therefore desirable to further elucidate the electronic structure of such complexes. In contrast to other analytical techniques, X-ray absorption spectroscopy (XAS) is able to provide experimental data to determine the oxidation state of metal ions based on the effective nuclear charge  $Z^{\text{eff}}$  of the probed element.<sup>[50]</sup> Thus, a series of similar complexes of the type  $[\text{W}(\text{CO})(\text{C}_2\text{R}_2)\text{L}_2]$  and  $[\text{WO}(\text{C}_2\text{R}_2)\text{L}_2]$  should be probed by W L-edge and S K-edge XAS. The collected data should then be compared and evaluated to gain new insight into the electronic environment of the metal-center as well as unveil details about metal-ligand covalent interactions.

## RESULTS AND DISCUSSION

### 3. REVISITING THE REACTION MECHANISM OF AH

In order to determine the effect of C-C-elongation for a potential nucleophilic attack on acetylene, preliminary calculations, in which the C-C-distance of the alkyne was gradually increased, were performed. To quantitate the effect of acetylene activation by the W(IV)-center in a hypothetical first-shell mechanism, acetylene hydration was then calculated as a concerted mechanism in the W inner-sphere at the DFT level. The ligand field of the active site was modeled based on the crystal structure of AH including two but-2-ene-2,3-bis(thiolate)-units for the pterin co-factors and a methyl thiolate for the Cys-141-residue (**Figure 12**). Acetylene was bound to W in a side-on fashion and a water molecule was moved towards the substrate in increments of 0.3 Å. Structures were fully optimized at each step. In total, the model comprised 37 atoms with an overall charge of -1.

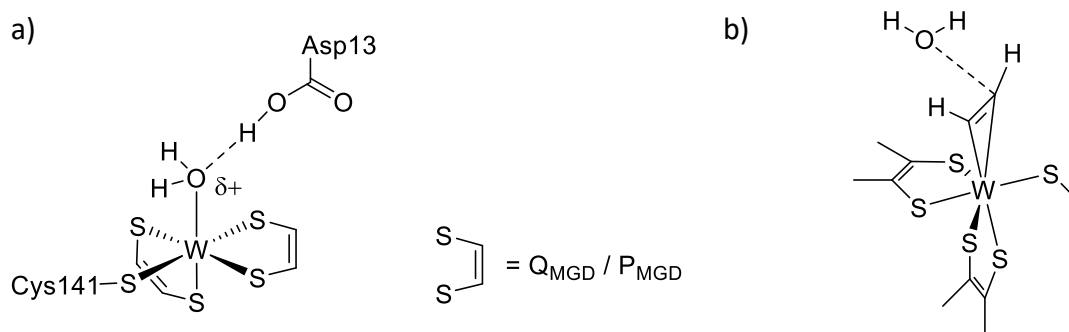


**Figure 12:** a) Crystal structure of the active site of acetylene hydratase;<sup>[15]</sup> b) active site model for the W-assisted hydration of acetylene.

#### 3.1. C-C-elongation

In order to understand the effect of C-C-elongation on the HOMO-LUMO gap of acetylene, C-C-distances were constrained between 1.00 Å and 1.60 Å for geometry optimization. The corresponding HOMO-LUMO gaps are summarized in **Table 3**.

**Table 3:** HOMO-LUMO gaps of acetylene dependent on the C-C-bond length  $d(\text{C-C})$ .

$d(\text{C-C})$ [Å]	$E_{\text{HOMO}}$ [eV] <sup>a</sup>	$E_{\text{LUMO}}$ [eV] <sup>a</sup>	$E_{\text{HOMO}} - E_{\text{LUMO}}$ [eV]
1.00	-8.68	3.26	11.94
1.10	-8.14	2.34	10.48
1.20	-7.84	1.47	9.31
1.30 <sup>b</sup>	-7.29	0.65	7.94
1.40 <sup>b</sup>	-6.99	0.00	6.99
1.50 <sup>b</sup>	-6.72	-0.63	6.09
1.60 <sup>b</sup>	-6.50	-1.14	5.36

<sup>a</sup> electronic energies; <sup>b</sup>  $d(\text{C-C}) > d(\text{C-C}_{\text{free acetylene}})$ .

The calculated data shows that longer the C-C-distances, the higher the energy of the HOMO and the lower the energy of the LUMO. Interestingly, the overall decrease in energy by the LUMO from 3.26 eV to -1.14 eV is almost two times the energy increase calculated for the HOMO from -8.68 eV to -6.50 eV. In the series of gradually decreasing HOMO-LUMO gaps, particularly large differences of 1.40 eV and 1.37 eV were calculated for the C-C-elongation from 1.00 Å to 1.10 Å and from 1.20 Å to 1.30 Å, respectively.

In many cases, activation of small molecules by transition metals includes  $\pi$ -backdonation of the metal-center into anti-bonding orbitals of the substrate.<sup>[85]</sup> Acetylene, the natural substrate of the W-dependent enzyme AH, has two sets of  $\pi^*$ -orbitals available for metal to ligand interaction. In the case that acetylene hydration proceeds via a first-shell mechanism, the  $d^2$ -configuration of W in the active site would therefore be able to activate the substrate by  $\pi$ -backdonation into one of the anti-bonding  $\pi$ -orbitals. Simultaneously, electron-donation of acetylene into the empty d-orbitals of the metal-center reduces the triple-bond character of the alkyne further. Experimentally, the activation of acetylene by alkyne-donation and  $\pi$ -backdonation is commonly observed as elongated C-C-distances.<sup>[86–88]</sup>

Decreasing HOMO-LUMO gaps in correlation with an increasing C-C-distance can be explained by the interaction of the respective atomic orbitals. When pulling the carbon-atoms of  $\text{C}_2\text{H}_2$  apart, the overlap between the bonding C-orbitals is reduced. Thus, the increasing energy of the HOMO with increasing C-C-distance correlates to destabilization of the bonding MOs due to reduced orbital overlap. On the other hand, an increased distance between the carbon-atoms is beneficial for the anti-bonding orbitals in acetylene. In the LUMO, the unlike p-orbitals experience less repulsion the further they are apart from each other. Therefore, a reciprocal correlation between the energy of the LUMO and the C-C-distances is in agreement with the calculated energy values. The largest changes in the

HOMO-LUMO gap were calculated at a very short C-C-distance of 1.00 Å and at the C-C-distance of 1.30 Å, which exceeds the C-C-distance of the energy minimum at 1.20 Å. In the first case, the large HOMO-LUMO gap can be attributed to increased repulsion of unlike orbitals at small C-C-distances. In the second case, the stabilizing interaction of the bonding orbitals is significantly reduced by the larger C-C-distance.

In regard to the reaction mechanism of acetylene hydratase, an energetically low  $\pi^*$ -orbital of  $C_2H_2$  would be beneficial for a nucleophilic attack of water due to smaller energy differences between the involved orbitals. Thus, metal-activation of the substrate should facilitate such a reactivity significantly.

### 3.2. W-assisted hydration of acetylene

The calculated energy profile for the W-assisted vs. the uncatalyzed hydration of acetylene is displayed in **Figure 13**.

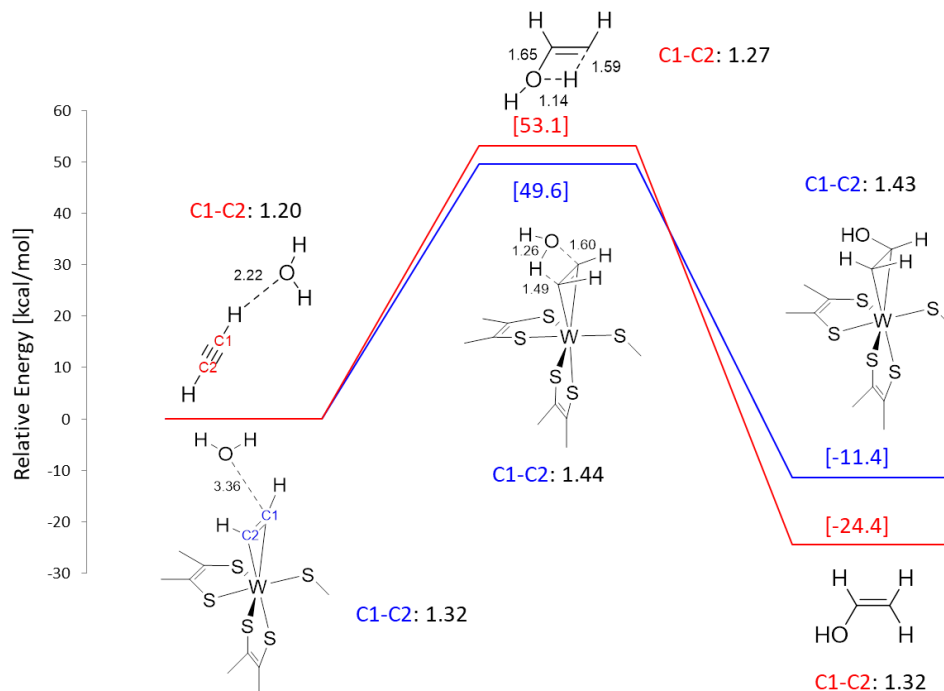


**Figure 13:** Energy profile of the W-assisted (blue) vs. the uncatalyzed (red) hydration of acetylene.<sup>[89]</sup> Bond lengths of the optimized structures are given in Å and energies are displayed in [kcal/mol].

In the fully optimized starting complex acetylene is coordinated towards tungsten in a side-on fashion and the C-C-bond is elongated by 0.12 Å compared to the calculated C-C-distance of free C<sub>2</sub>H<sub>2</sub>. The reaction of both, the uncatalyzed as well as the metal-assisted route, proceeds in a concerted manner. The transition structures are similar for both pathways and feature a four-membered ring, consisting of the acetylenic carbon-atoms and the O-H-bond of water. An energy barrier of 49.6 kcal/mol was calculated for the W-assisted mechanism, which is 3.5 kcal/mol lower than the activation barrier of the uncatalyzed reaction. Since tautomerization of vinyl alcohol to acetaldehyde is assumed to occur spontaneously, further reaction steps were not investigated.

Liao and co-worker proposed a reaction mechanism, which included the nucleophilic attack of a deprotonated water molecule on W-bound acetylene.<sup>[17]</sup> Their results showed that the  $\pi_{\parallel}^*$ -orbital of C<sub>2</sub>H<sub>2</sub> is involved in a bonding interaction with the filled W d(xz)-orbital whereas the nucleophilic attack of the water lone pair occurs at the  $\pi_{\perp}^*$ -orbital (**Figure 14**).<sup>[17]</sup> This is in agreement with the orbitals generated for the W-assisted approach of acetylene hydration. In order to determine the sole effect of acetylene activation by the metal-center, Asp-13, which deprotonates water in the Liao-model, was intentionally not included in this work.

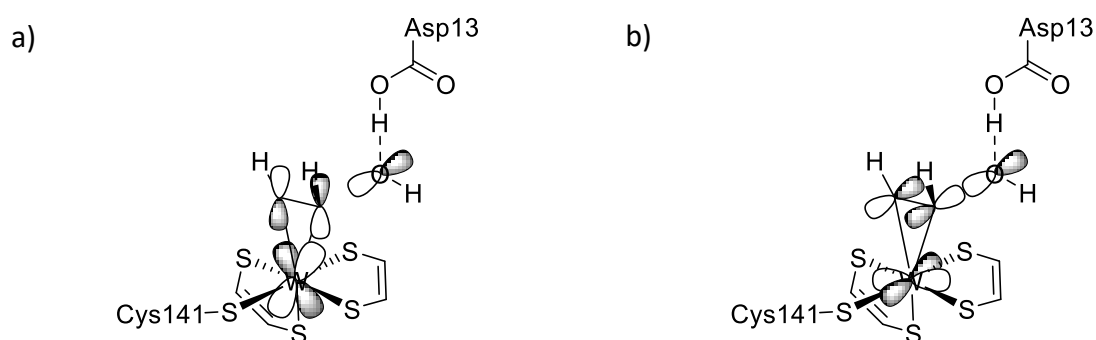


**Figure 14:** Orbital arrangement in the first transition structure of the mechanism by Liao and co-workers for a) the  $\pi$ -backdonation from d(xz) into the  $\pi_{\parallel}^*$ -orbital and b) the nucleophilic attack of water at the  $\pi_{\perp}^*$ -orbital.<sup>[17]</sup>

Although the computed C-C-bond length of 1.32 Å is significantly larger in the starting complex of the W-assisted pathway compared to the 1.20 Å of the free substrate, the energy barriers of 49.6 kcal/mol for the W-assisted and 53.1 kcal/mol for the uncatalyzed reaction differ only slightly. This is surprising since a considerable reduction of the energy barrier

through the energetically lowering of the  $\pi_{\perp}^*$ -orbital of acetylene by metal-activation was anticipated. Nevertheless, it indicates that in the Liao-model the significantly lower activation barrier of 23.0 kcal/mol<sup>[17]</sup> is not primarily connected with acetylene activation by the W(IV)-center. Instead, the Asp-13-residue, which was not included in this work, seems to have a larger influence on the calculated energy barrier.

However, when repeating the calculations for the W-assisted hydration using a split basis set for tungsten (LANL2DZ) and the other elements (6-31G\*\*) to receive more accurate energy values, a different reactivity was observed. Instead of a concerted reaction pathway, deprotonation of water by a dithiolate-ligand was observed as a first reaction step. Detailed energetics for this new pathway are still under investigation. Nevertheless, a similar mechanism for acetylene hydration, where water is deprotonated by the sulfur coordination sphere, was previously reported by Liu and co-workers, but involved a high energy barrier of 38.4 kcal/mol.<sup>[89]</sup>

### 3.3. Enforcing early transition states for acetylene hydration

In nature, enzymes often exhibit a constrained geometries to facilitate catalytic reactions.<sup>[90]</sup> These constrained structures are geometrically similar to the transition structure of the reaction and lead to low energy barriers.<sup>[91]</sup> According to this principal, small activation barriers should be obtained if the geometry of the starting structure is adjusted to the geometric parameters observed at the transition state. From an energetic point of view, such an adjustment increases the energy of the starting complex relative to the transition state, which leads to a reduced energy barrier.

In calculations investigating the reactivity of sulfite oxidase, it was shown that the rotation of the thiolate-residue vs. the Mo-oxo-axis increased the total energy of the starting complex by up to 17.4 kcal/mol (**Figure 15**).<sup>[92]</sup>

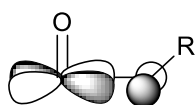


**Figure 15:** Orbital interaction between Mo and S at a dihedral angle O=Mo-S-C of 0.0°.

In order to obtain early transition states in the W-assisted hydration of acetylene, dihedral angles (dh) between the SCH<sub>3</sub>-moiety and the W-acetylene-axis as well as between the dithiolate-ligands were therefore constrained for geometry optimization (**Figure 16**).

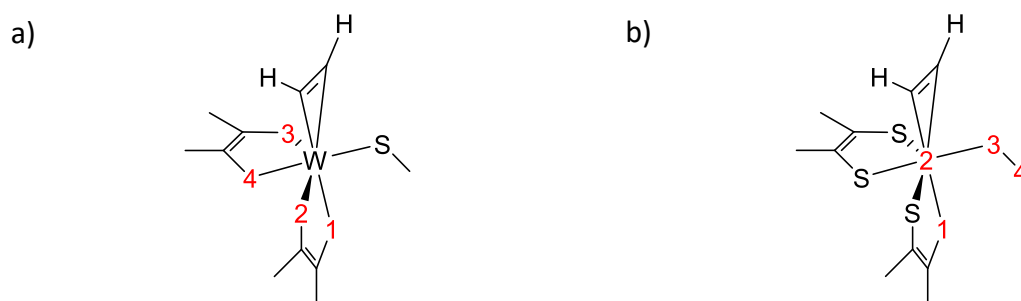


**Figure 16:** Constrained dihedral angles (dh) of a) the dithiolate-units and b) the thiolate-residue.

The methyl thiolate-moiety was constrained at 0.0° and 90.0° relative to the W-acetylene-axis to minimize and maximize the overlap with the d(xy)-orbital, respectively (**Figure 17b** and c).



**Figure 17:** Orbital interaction between a) W and S at dh(methyl thiolate) = 0.0° and b) W and S at dh(methyl thiolate) = 90.0°.

The dihedral angle of the dithiolate-units, on the other hand, was fixed at 102.7°, which equals the angle found at the transition state of the fully optimized reaction (**Table 4**).

**Table 4:** Effect of constrained dihedral angles on the energy barrier of acetylene hydration.

Structure	dh(dithiolates)	dh(methyl thiolate)	$E_{TS} - E_{SC}$ [kcal/mol] <sup>a</sup>
Starting complex (SC) <sup>b</sup>	113.4°	-75.4°	47.8
Transition structure <sup>b</sup>	102.7°	28.0°	
SC1	109.6°	0.0°	52.3
SC2	70.3°	90.0°	46.1
SC3	102.7°	-76.1°	47.6

<sup>a</sup>  $E_{SC} = E_{\text{complex}} + E_{\text{water}}$ ; <sup>b</sup> values taken from the fully optimized reaction in section 3.2; red: constrained dh.

Aligning the methyl thiolate with the W-acetylene-axis in SC1 resulted in an energy difference between starting complex and transition state of 52.3 kcal/mol.



For SC2, where the methyl thiolate is oriented perpendicular to the W-actylene-axis, an energy difference of 46.1 kcal/mol was calculated. In SC3, the dihedral angle between the dithiolates was fixed at 102.7°, which resulted in an energy difference of 47.6 kcal/mol.

At  $\text{dh}(\text{methyl thiolate})$  of 0.0°, the highest energy difference to the transition state was obtained. This suggests that SC1 is stabilized instead of energetically elevated, which is in agreement with increased  $\pi$ -bonding between W and the thiolate-ligand at this angle. At a dihedral angle of 90° the energy barrier decreases by 1.7 kcal/mol compared to the fully optimized reaction. This correlates to the expected destabilizing interaction between the W  $d(xy)$ - and the S  $p_z$ -orbital, which increases the energy of SC2. When constraining the dihedral angle between the two dithiolate-units, the energy difference between starting complex and transition state is only 0.2 kcal/mol lower than in the original reaction. This indicates that the applied constraint does not significantly raise the energy of SC1.

In conclusion, the high energy differences calculated for these starting complexes do not indicate a first-shell mechanistic proposal through destabilization of the active site geometry by constrained dihedral angles in the sulfur coordination sphere.

## 4. SYNTHESIS OF W ALKYNE-COMPLEXES

For the preparation of a biomimetic model complex of acetylene hydratase, (2-dimethylethanethiol)-bis(3,5-dimethylpyrazol)methane (L3SH) was synthesized according to a literature procedure by Hammes and Carrano (**Scheme 12**).<sup>[79]</sup> The obtained <sup>1</sup>H NMR data was in accordance with literature values and showed six singlets in the ratio 1:2:1:6:6:6 for the tertiary hydrogen, the equivalent pyrazolyl protons, the thiol-group and the triple set of equivalent methyl-groups. The W(II)-precursors of the type [W(CO)(C<sub>2</sub>R<sub>2</sub>)<sub>2</sub>(CH<sub>3</sub>CN)Br<sub>2</sub>] (R = Ph, Me, H) were prepared according to procedures developed in the Mösch-Zanetti-group and provided by Carina Vidovic MSc for this work.<sup>[93]</sup>

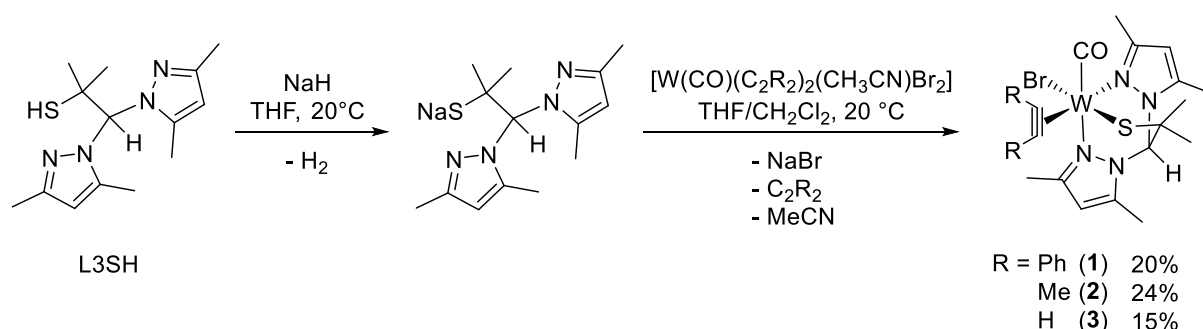
### 4.1. Synthesis of the W(II)-complexes [W(CO)(C<sub>2</sub>R<sub>2</sub>)(L3S)Br] (R = Ph, Me, H)

For the synthesis of the complexes [W(CO)(C<sub>2</sub>R<sub>2</sub>)(L3S)Br] (R = Ph (**1**), Me (**2**), H (**3**)) the ligand addition route was followed (**Scheme 12**). Prior to salt metathesis, L3SH was deprotonated in THF using NaH dispersed in 60% mineral oil. The reaction was stirred for 30 min to 60 min until gas evolution ceased. The THF phase, containing L3SNa, was immediately added to a suspension of [W(CO)(C<sub>2</sub>R<sub>2</sub>)<sub>2</sub>(CH<sub>3</sub>CN)Br<sub>2</sub>] (R = Ph, Me, H) in CH<sub>3</sub>CN. After stirring for 10 min to 15 min the solvent was evaporated in vacuo and the reaction mixture redissolved in CH<sub>2</sub>Cl<sub>2</sub>. Undissolved NaBr was removed via filtration. Complexes **1** and **3** were further purified in air via column chromatography on silica gel. For complex **2**, flash chromatography was not feasible due to decomposition of the product. After removal of NaBr, the solution was therefore concentrated and layered with heptane for recrystallization. Within 2 h a dark brown solid precipitated while the supernatant solution turned blue with fine particles dispersed in it. The blue phase was then decanted and cooled to -18 °C for complete precipitation of complex **2**.

Complex **1** was obtained as a green powder in 20% yield. The complex was stable in air and in solution in dry and wet solvents over several weeks. Pure complex **2** was isolated as a blue powder in 24% yield. Under air, a brownish-black layer formed on the surface of the product within 24 hours. The nature of this layer could not be characterized by <sup>1</sup>H NMR spectroscopy. In solution decomposition of the compound was observed in dry and wet

solvents over night. Complex **3** was obtained in 15% yield as a light blue powder. The compound was stable in air and in dry and wet solvents over several days.

Single crystals of complexes **1** and **2** were grown from CH<sub>2</sub>Cl<sub>2</sub> layered with heptane at -18 °C. All attempts to obtain single crystals of complex **3** failed.



**Scheme 12:** Synthetic route for the preparation of complexes **1 – 3**.

The <sup>1</sup>H NMR spectra of the chiral complexes **1 – 3** each displayed six singlets assigned to the L3S-based methyl-groups in the aliphatic region. Chemical shifts were similar in chlorinated solvents and ranged between 1.13 ppm and 2.81 ppm. In complex **2** and **3**, the singlets of the methyl-groups in proximity to the S-donor appeared upfield between 1.13 ppm and 1.45 ppm while the protons of the pyrazolyl methyl-groups resonated between 2.38 ppm and 2.81 ppm. In complex **1**, the ligand-based signals could not be differentiated. For complexes **1 – 3**, the singlets in the aromatic region of the spectra between 5.95 ppm and 6.29 ppm were assigned to the pyrazolyl hydrogen-atoms and the tertiary proton of the L3S-ligand. Coordinated diphenylacetylene of [W(CO)(C<sub>2</sub>Ph<sub>2</sub>)(L3S)Br] (**1**) was observed as a multiplet at 7.37 ppm in CD<sub>2</sub>Cl<sub>2</sub>. For [W(CO)(C<sub>2</sub>Me<sub>2</sub>)(L3S)Br] (**2**), the protons of the two rotationally hindered methyl-residues of dimethylacetylene resonated at 3.02 ppm and 3.07 ppm in CDCl<sub>3</sub> whereas they could not be differentiated in CD<sub>2</sub>Cl<sub>2</sub>. The <sup>1</sup>H NMR resonances of the rotationally hindered acetylenic protons of [W(CO)(C<sub>2</sub>H<sub>2</sub>)(L3S)Br] (**3**) were recorded as two distinct singlets at 12.83 ppm and 11.91 ppm in CD<sub>2</sub>Cl<sub>2</sub>.

In the <sup>13</sup>C NMR spectra of complexes **1** and **3**, the signal of the carbonyl-group is displayed at 232 ppm and 231 ppm for complexes **1** and **3**, respectively. The <sup>13</sup>C resonances of the alkyne carbon-atoms appeared at 204 ppm and 198 ppm for the diphenylacetylene- and at 185 ppm and 194 ppm for the dimethylacetylene-ligand. <sup>13</sup>C-<sup>183</sup>W coupling was not observed for

complex **1** and **3** when recording overnight. A  $^{13}\text{C}$  NMR spectrum of complex **2** could not be obtained due to decomposition in solution.

In the IR spectrum, a prominent CO-band was observed at  $1908\text{ cm}^{-1}$  for the complex  $[\text{W}(\text{CO})(\text{C}_2\text{Ph}_2)(\text{L3S})\text{Br}]$  (**1**). CO-frequencies of  $1889\text{ cm}^{-1}$  and  $1900\text{ cm}^{-1}$  were recorded for the complexes  $[\text{W}(\text{CO})(\text{C}_2\text{Me}_2)(\text{L3S})\text{Br}]$  (**2**) and  $[\text{W}(\text{CO})(\text{C}_2\text{H}_2)(\text{L3S})\text{Br}]$  (**3**), respectively. These values are in range with other W(II) CO-complexes.<sup>[86–88]</sup>

When performing the salt metathesis with the isolated ligand salt (L3SNa), considerable side product formation was observed. Although spectroscopic evidence indicating decomposition or oxidation of  $\text{L3S}^-$  is lacking, better results were achieved when deprotonation was executed in-situ for each experiment (Sec. 7.1). Increasing amounts of impurities were also observed for reaction times over 15 min and led to significantly lower yields under 5%. Since no fitting integral ratios could be found, the additional peaks in the  $^1\text{H}$  NMR spectra could not be assigned to potential product isomers or a complex of the type  $[\text{W}(\text{L3S})_2]$ . Performing the reaction at low temperatures, such as  $-78\text{ }^\circ\text{C}$  and  $0\text{ }^\circ\text{C}$ , did not improve reaction selectivity. Furthermore, analysis of the different fractions collected by column chromatography of complexes **1** and **3** did not give conclusive results regarding the nature of the side products. In order to rule out decomposition of the complexes on  $\text{SiO}_2$ , repetitive recrystallization from  $\text{CH}_2\text{Cl}_2$ /heptane was tested as an alternative purification method for the complexes  $[\text{W}(\text{CO})(\text{C}_2\text{Ph}_2)(\text{L3S})\text{Br}]$  and  $[\text{W}(\text{CO})(\text{C}_2\text{H}_2)(\text{L3S})\text{Br}]$ , but did not increase product yields. Considerable side product formation and low yields were also observed in the preparation of molybdenum L3S-complexes.<sup>[82,83]</sup> This might indicate a generally limited stability of the deprotonated L3S-ligand.

#### 4.1.1. Comparison of complexes of the type $[\text{W}(\text{CO})(\text{C}_2\text{H}_2)\text{L}_2]$

In W(II)-complexes with a coordinated alkyne and a terminal CO-group, the  $d(xz)$ - and  $d(yz)$ -orbitals of tungsten are stabilized by interaction with the anti-bonding alkyne- and CO-orbitals (**Figure 18**).<sup>[94]</sup> Occupied by the W d-electrons,  $\pi$ -backdonation from these orbitals into  $\pi^*$ -orbitals of the coordinated alkyne as well as the terminal CO-group reduces the triple-bond character of both ligands. The acetylene derivatives can furthermore donate

up to four electrons into the empty  $W d(x^2-y^2)$ - and  $d(xy)$ -orbitals of tungsten. Electron-donation from the alkyne as well as  $\pi$ -backdonation from the metal-center therefore contribute to experimentally observed elongated C-C-bond lengths and R-C $\equiv$ C-angles similar to  $sp^2$ -hybridized carbon-atoms in  $C_2R_2$ .<sup>[86–88]</sup>

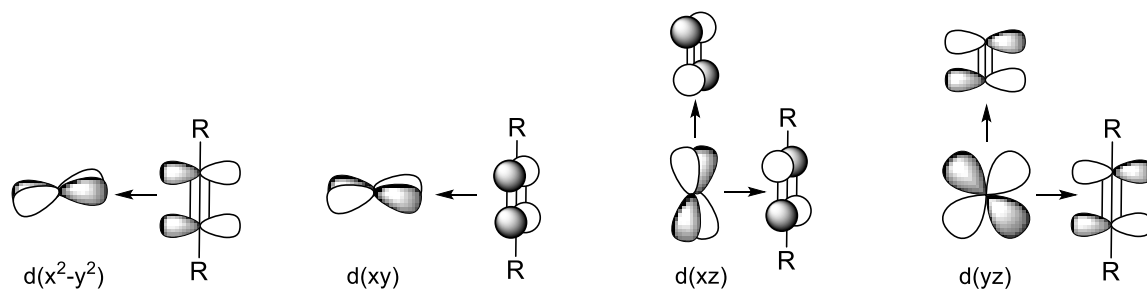


**Figure 18:** Metal-ligand interactions in W(II) CO-complexes with mono-coordinated alkynes.

In order to estimate the degree of acetylene activation in the complex  $[W(CO)(C_2H_2)(L3S)Br]$  (**3**), structural and spectroscopic data was compared with other complexes of the form  $[W(CO)(C_2H_2)L_2]$ .

**Table 5:** Spectroscopic data of complexes of the form  $[W(CO)(C_2H_2)L_2]$ .

	$\delta(\equiv C-H)^a$ [ppm]	$\delta(C\equiv C)^b$ [ppm]	$\nu(CO)$ [ $cm^{-1}$ ]	ref.
$[W(CO)(C_2H_2)(L3S)Br]$ ( <b>3</b> )	12.83 11.91	194 185	1900	this work
$[W(CO)(C_2H_2)Tm^{Me}Br]^d$	12.71 12.13	197 193	1900	[93]
$[W(CO)(C_2H_2)Tp^*I]$	13.59 12.42	209 199	1896 <sup>c</sup>	[95]
$[W(CO)(C_2H_2)(S-Phoz)_2]$	12.22 11.57	200 193	1889	[23]

<sup>a</sup>  $^1H$  NMR data in  $CD_2Cl_2$ ; <sup>b</sup>  $^{13}C$  NMR data in  $CD_2Cl_2$ ; <sup>c</sup> KBr pellet; <sup>d</sup>  $Tm^{Me}$  = hydrotris(methimazolyl)borate.

According to **Table 5**, the frequency of the CO-vibration increases for the complexes in the ligand order S-Phoz <  $Tp^*$  <  $Tm^{Me}$ , L3S. Since  $\nu(CO)$  is higher the smaller the  $\pi$ -backdonation into the  $\pi^*$ -orbitals of the CO-group, the heteroscorpionate ligands  $Tm^{Me}$  and L3S seem to exhibit the most electron-deficient character.

Due to electron-donation of coordinated acetylene into empty d-orbitals of tungsten, the  $^1H$  NMR resonances of acetylenic H-atoms shift downfield compared to free  $C_2H_2$ , which displays a singlet at 1.91 ppm in  $CDCl_3$ .<sup>[96]</sup> The magnitude of this shift depends on the amount of ligand-donation as well as  $\pi$ -backdonation from the metal-center.

For ternary Cu(I) ethylene-complexes of the type  $[\text{Cu}(\text{C}_2\text{H}_4)\text{L}]$  (L = phenantroline (phen), 2,2'-bipyridine (bpy), tetramethylethylenediamine (tmen)), an upfield shift of the  $^1\text{H}$  NMR resonances of  $\text{C}_2\text{H}_4$  was observed the higher the basicity of the opposing N-ligands.<sup>[97]</sup> This indicates that  $\pi$ -backdonation from Cu into  $\pi^*$ -orbitals of ethylene is enhanced the more electron-donating the ligand *trans* to  $\text{C}_2\text{H}_4$ . In regard to the acetylene-complexes, the increasing  $^1\text{H}$  NMR chemical shifts of the  $\text{C}_2\text{H}_2$ -protons in the complex order  $\text{S-Phoz} < \text{L3S} \leq \text{Tm}^{\text{Me}} < \text{Tp}^*$  therefore classifies S-Phoz as the most electron-donating and  $\text{Tp}^*$  as the most electron-deficient ligand. The observed electron-donating effect of the S-Phoz-ligand should increase  $\pi$ -backdonation in the complex, which is in accordance with the low CO stretching-frequency in the IR spectrum of this complex. However, the upfield chemical shift of acetylenic protons in the L3S- and  $\text{Tm}^{\text{Me}}$ -complexes compared to the  $\text{Tp}^*$ -system indicate a higher degree of  $\pi$ -backdonation in these complexes than in  $[\text{W}(\text{CO})(\text{C}_2\text{H}_2)\text{Tp}^*]$ . This is contradictory to the increasing CO-frequencies from  $\text{Tp}^*$  to  $\text{Tm}^{\text{Me}}$  and L3S.

The number of S-atoms in the first coordination sphere, which increases in the order  $\text{Tp}^* < \text{L3S} < \text{S-Phoz} < \text{Tm}^{\text{Me}}$ , could not be correlated to  $^1\text{H}$  NMR and IR data, either. Considering that the complex geometries are distorted, the spectroscopic and structural differences might arise from varying degrees of interaction between the W-center and the ligand field.

The  $^{13}\text{C}$  NMR resonances of  $\text{C}_2\text{H}_2$  are indicative of the electrophilicity of the coordinated acetylenic carbon-atoms.<sup>[98]</sup> Increasing positive charge is expected when electron density is removed by donation from the C-C triple-bond into empty metal d-orbitals as well as reduced  $\pi$ -backdonation from the W-center. An empirical correlation between  $^{13}\text{C}$  NMR resonances of the alkyne and its formal number of donated electrons further shows that in complexes with an average  $^{13}\text{C}$  NMR chemical shift above 185 ppm, four electrons are donated by the alkyne.<sup>[98]</sup> According to this study, the coordinated acetylene ligands of all the complexes discussed in this section can be considered four-electron-donors. The small variance between the  $^{13}\text{C}$  NMR resonances among the complexes can be attributed to slight differences in the degree of alkyne-donation and W  $\pi$ -backdonation. However, since their effect is opposite to each other and both interactions can affect the magnitude of the experimental  $\delta(\text{C}\equiv\text{C})$  value for each of the complexes individually, an overall trend is hard to predict.

#### 4.1.2. Comparison of complexes of the type $[W(CO)(C_2R_2)L_2]$ (R = Ph, Me, H)

In order to further understand the influence of the acetylenic residues on alkyne activation, complexes of the type  $[W(CO)(C_2R_2)L_2]$  (R = Ph, Me, H) were compared with complexes **1 – 3** (Table 6).

**Table 6:** Structural and spectroscopic data of complexes of the type  $W(CO)(C_2R_2)L_2$ .

	C≡C [Å]	$\Delta(C\equiv C)^a$ [Å]	R-C≡C [°]	$\nu(CO)$ [ $cm^{-1}$ ]	ref.
$[W(CO)(C_2Ph_2)(L3S)Br]$ ( <b>1</b> )	1.318(3)	0.119(9)	133.2(2) 136.4(2)	1908	this work
$[W(CO)(C_2Ph_2)(S-Phoz)_2]^b$	1.309(3)	0.110(9)	143.0(2) 142.8(2)	1927	[31]
$[W(CO)(C_2Ph_2)Tm^{Me}Br]$	1.332(8)	0.134(4)	140.5(5) 133.1(6)	1913	[93]
$[W(CO)(C_2Me_2)(L3S)Br]$ ( <b>2</b> )	1.307(3)	0.096	140.6(2) 140.6(2)	1889	this work
$[W(CO)(C_2Me_2)(S-Phoz)_2]$	1.314(3)	0.103	139.0(3) 136.2(8)	1880	[31]
$[W(CO)(C_2Me_2)Tm^{Me}Br]$	1.314(7)	0.104	141.2(6) 138.5(5)	1882	[93]
$[W(CO)(C_2H_2)(L3S)Br]$ ( <b>3</b> )	-	-	-	1900	this work
$W(CO)(C_2H_2)(S-Phoz)_2$	1.327(3)	0.14(1)	146.9(2) 122.7(2)	1889	[20]
$[W(CO)(C_2H_2)Tm^{Me}Br]$	1.252(7)	0.06(7)	147.1(7) 140.5(1)	1900	[93]

<sup>a</sup> C-C-difference between complex and free  $C_2R_2$  [99–101], <sup>b</sup> data of the S-S isomer found in single crystals.

The increase of the CO stretching-frequencies within the individual ligand-series of complexes in the order  $C_2Me_2 < C_2H_2 < C_2Ph_2$  can be explained by different degrees of  $\pi$ -backdonation into the  $\pi^*$ -orbitals of CO. In the complexes with coordinated  $C_2Ph_2$ , the CO-group requires the most energy for vibration, which suggests the least degree of  $\pi$ -backdonation towards CO in these complexes. Since the coordinated alkyne and the CO-ligand compete for the d-electrons of the W-center, the negative inductive effect of the phenyl-groups seems to increase  $\pi$ -backdonation into  $C_2Ph_2$ . Simultaneously the interaction with the  $\pi^*$ -orbitals of CO should be reduced. Dimethylacetylene, on the other hand, has a slightly positive inductive effect compared to a hydrogen-atom. Thus, the lower CO-frequencies of the  $C_2Me_2$ -complexes indicate enhanced  $\pi$ -backdonation into the CO-ligand in the  $C_2Me_2$ - compared to the  $C_2H_2$ -compounds.

The observed CO-frequencies suggest reciprocal degrees of  $\pi$ -backdonation into the CO-group and the coordinated alkyne in correlation with the alkyne-residues of the complexes. Thus, C-C-bond elongation of the alkynes should be more pronounced the higher the  $\pi$ -backdonation into the alkyne and the lower the metal to ligand interaction with  $\pi^*$ -orbitals of CO. In order to determine alkyne-activation, C-C-distances of  $C_2R_2$  are compared with the C-C-bond lengths of 1.18(6) Å in free  $C_2H_2$ , 1.211 Å in free  $C_2Me_2$  and 1.198(4) Å in free  $C_2Ph_2$ .<sup>[99–101]</sup> According to this concept, the average increase of the C-C-bond length in the  $C_2Ph_2$ -complexes by 0.12 Å is larger than the average C-C-elongation by 0.10 Å in the  $C_2Me_2$ -complexes. This suggests increased  $\pi$ -backdonation in the diphenylacetylene-compounds compared to the dimethylacetylene-complexes, which is in agreement with the observed reciprocal degrees of  $\pi$ -backdonation into the corresponding CO-ligands. Elongation of the C-C triple-bond in the  $C_2H_2$ -complexes is contradictory within the two complexes  $[W(CO)(C_2H_2)(S-Phoz)_2]$  and  $[W(CO)(C_2H_2)(Tm^{Me})Br]$ . A large increase of the C-C-distance by 0.14(1) Å in  $[W(CO)(C_2H_2)(S-Phoz)_2]$  and a small increase by 0.06(7) Å in  $[W(CO)(C_2H_2)(Tm^{Me})Br]$  compared to free acetylene is observed. This indicates a high degree of  $\pi$ -backdonation into  $C_2H_2$  of the acetylene S-Phoz-complex, in which the CO-group is activated considerably by the W-center as well. In the acetylene  $Tm^{Me}$ -complex, on the other hand, the C-C-bond seems to experience the least amount of  $\pi$ -backdonation while  $\pi$ -backdonation into the CO-ligand is similar to the other  $C_2H_2$ -complexes.

The R-C $\equiv$ C-angles, which are smaller the higher the  $sp^2$ -character of the alkyne C-atom, are in the same range for all complexes except  $[W(CO)(C_2H_2)(S-Phoz)_2]$ . In the latter, the two angles differ significantly (122.7(2)° and 146.9(2)°) and suggest a particularly asymmetric coordination of the acetylenic carbon-atoms. An overall trend in correlation with the acetylene-residues is not found for the R-C $\equiv$ C-angles.

In summary, reciprocal degrees of  $\pi$ -backdonation into the alkyne- and the CO-ligand directed by the negative inductive effect of the Ph-groups and the positive inductive effect of the Me-groups was observed. In the  $C_2H_2$ -complexes, the collected structural and spectroscopic data is more diverse compared to the other compounds and might be attributed to more electronic flexibility of the H-residue.



### 4.1.3. Molecular structures

Molecular structures of complexes  $[\text{W}(\text{CO})(\text{C}_2\text{Ph}_2)(\text{L3S})\text{Br}]$  (**1**) and  $[\text{W}(\text{CO})(\text{C}_2\text{Me}_2)(\text{L3S})\text{Br}]$  (**2**) were determined by single crystal X-ray diffraction analysis. Selected bond lengths and angles are given in **Table 12** and **Table 13** (Appendix). Both structures exhibit a distorted octahedral geometry with S-W-Br angles of  $159.23^\circ$  and  $160.30^\circ$  for complexes **1** and **2**, respectively. The C-H-bond of the facially bound tridentate L3S-ligand is facing away from the W-center and the coordinated alkyne is oriented parallel to the W-CO-bond (**Figure 19**). The pyrazoly N-donors of L3S are aligned *trans* to the CO group and the coordinated alkyne.

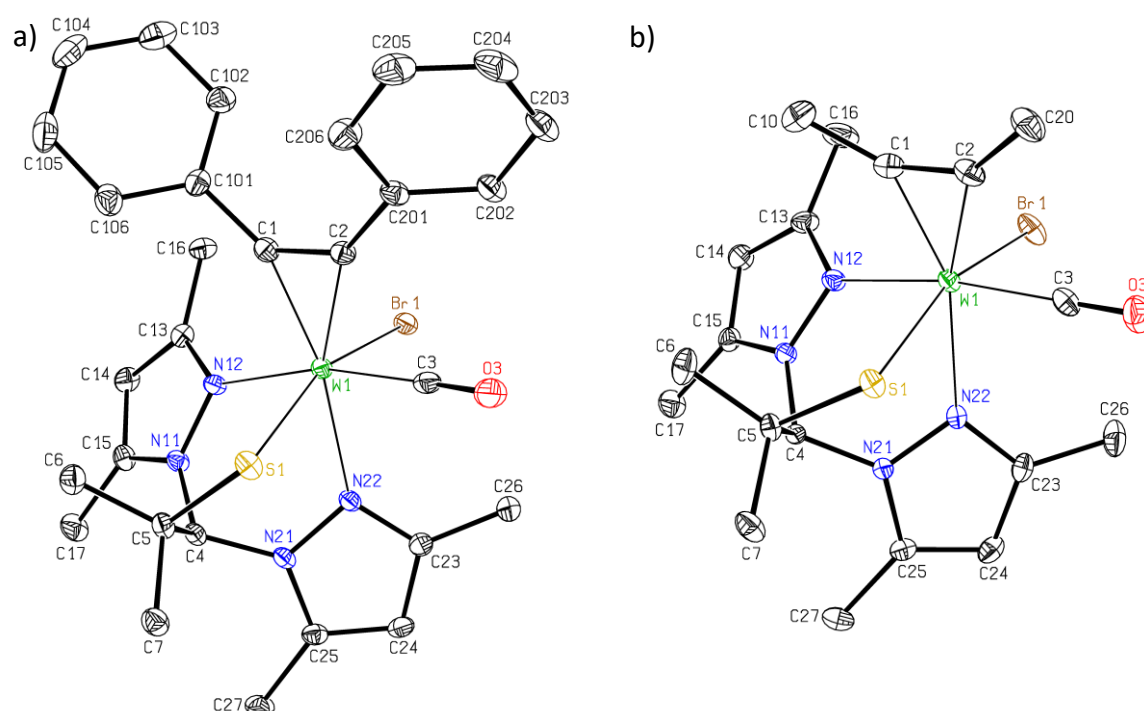


**Figure 19:** ORTEP plot of a) complex **1** and b) complex **2** showing the atomic numbering scheme.<sup>[102]</sup> The probability ellipsoids are drawn at the 50% probability level. The H-atoms as well as the solvent molecule were omitted for clarity.

The C-C $\equiv$ C-angles of the alkyne ligands are distorted from the ideal  $180^\circ$  angle of free  $\text{C}_2\text{Ph}_2$  and  $\text{C}_2\text{Me}_2$ . In the coordinated dimethylacetylene both methyl-groups form an angle of  $140.6^\circ$  with the C-C-axis. In the diphenylacetylene-ligand, on the other hand, the C-C $\equiv$ C-angles are asymmetric with  $133.2^\circ$  and  $136.4^\circ$ . In addition to this, the C-C-bonds of the acetylene derivatives are elongated by  $0.10 \text{ \AA}$  in  $[\text{W}(\text{CO})(\text{C}_2\text{Me}_2)(\text{L3S})\text{Br}]$  (**2**) and  $0.12 \text{ \AA}$  in  $[\text{W}(\text{CO})(\text{C}_2\text{Ph}_2)(\text{L3S})\text{Br}]$  (**1**) compared to the bond lengths of  $1.211 \text{ \AA}$  and  $1.198(4) \text{ \AA}$  in free  $\text{C}_2\text{Me}_2$  and  $\text{C}_2\text{Ph}_2$ , respectively.<sup>[99,100]</sup>

The W-alkyne-distances within each structure differ slightly, but display a shorter bond length to the carbon facing the CO-ligand (**Table 7**). The carbonyl-groups are at a distance of approximately 1.95 Å from W-center and display almost equal bond lengths of 1.148(3) Å and 1.148(2) Å in both complexes. The W-S- and W-Br-distances of the isostructural compounds are also very similar. Despite such close similarity, considerable differences can be observed in the W-N-bond lengths. While the W-N-distances in complex **1** range between 2.2748(18) Å and 2.2897(19) Å, complex **2** exhibits a W-N-distance of 2.3160(15) Å *trans* to dimethylacetylene and 2.2430(15) Å *trans* to the CO-group.

**Table 7:** Selected bond lengths in [Å].

	(L3S)W(CO)(C <sub>2</sub> Ph <sub>2</sub> )Br ( <b>1</b> )	(L3S)W(CO)(C <sub>2</sub> Me <sub>2</sub> )Br ( <b>2</b> )
C1-C2	1.318(3)	1.307(3)
W1-C1	2.034(2)	2.0205(19)
W1-C2	2.066(2)	2.0691(18)
W1-C3	1.956(2)	1.9513(19)
C3-O3	1.148(3)	1.148(2)
W1-S1	2.3759(6)	2.3814(5)
W1-N12	2.2748(18)	2.2430(15)
W1-N22	2.2897(19)	2.3160(15)
W1-Br1	2.6152(4)	2.6009(3)

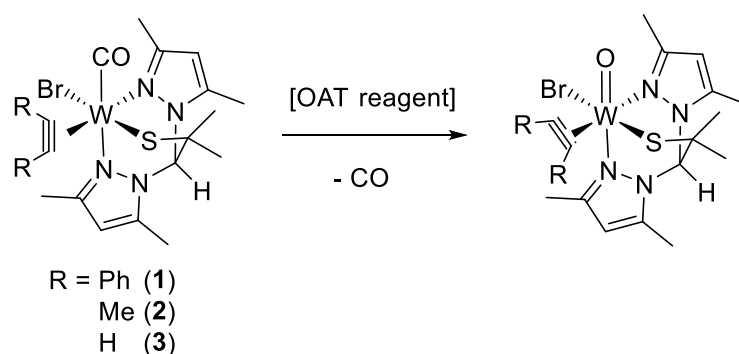
The stronger deviation from linear geometry in C<sub>2</sub>Ph<sub>2</sub> as well as the longer C-C-distance compared to C<sub>2</sub>Me<sub>2</sub> indicates a stronger transformation from sp- to sp<sup>2</sup>-hybridized carbon-atoms in complex **1**. Thus, the electron-donating ability of the alkyne as well as π-backdonation from the W-center seems to be influenced by the alkyne-substituents. Methyl-groups are considered to have a slight positive inductive effect, which would increase electron-donation towards the metal, but reduce π-backdonation. The negative inductive effect of phenyl-residues, on the other hand, is believed to increase the charge on the carbon-atoms and induce more π-backdonation from the W-center into the alkyne as suggested in section 4.1.2. The larger increase of the C-C-bond in complex [W(CO)(C<sub>2</sub>Ph<sub>2</sub>)(L3S)Br] (**1**) is therefore assumed to result from the increased π-backdonation into π\*-orbitals of C<sub>2</sub>Ph<sub>2</sub>. A closer look at the W-N-distances *trans* to alkynes furthermore reveals a longer W-N-bond in the complex [W(CO)(C<sub>2</sub>Me<sub>2</sub>)(L3S)Br] (**2**). Since dimethylacetylene and pyrazolyl-N both donate into the empty W d(x<sup>2</sup>-y<sup>2</sup>)-orbital, the longer W-N-distance might result from the increased electron-donation of the C<sub>2</sub>Me<sub>2</sub>-ligand. This was also observed for the complexes [W(CO)(C<sub>2</sub>R<sub>2</sub>)(Tm<sup>Me</sup>)Br] (R = Ph, Me), where the W-S-bond *trans* to C<sub>2</sub>Me<sub>2</sub> (2.6330(13) Å) was longer than *trans* to C<sub>2</sub>Ph<sub>2</sub> (2.611(2) Å).<sup>[93]</sup>

Enhanced  $\pi$ -backdonation of W into the  $\pi^*$ -orbitals of  $C_2Ph_2$  would suggest less activation of the CO-ligand, which competes with the alkyne for the d-electrons of the metal-center. Despite that, the CO-bond lengths are nearly identical in both complexes. This is in contrast to the CO-frequencies of  $1908\text{ cm}^{-1}$  for complex **1** and  $1889\text{ cm}^{-1}$  for complex **2**, which indicate different degrees of  $\pi$ -backdonation into the CO-ligand.

#### 4.2. Studies on W(IV)-complexes

W(IV)-complexes of the form  $[WO(C_2H_2)L_2]$  can be prepared by oxidation of the corresponding CO-complexes with a suitable oxygen atom transfer (OAT) reagent.<sup>[23,30]</sup> The preparation of previous biomimetic model compounds of acetylene hydratase involved oxidizing agents, such as pyridine *N*-oxide (PyNO) and  $Mo_2O_3[S_2P(OEt)_2]_4$ .<sup>[23,30,31]</sup> Other examples of oxidants include meta-chloro-perbenzoic acid (mCPBA), which was feasible for the synthesis of the mono-oxo-complex  $[WO(acac)_2(PhC_2H)]$  (acac = acetylacetonate),<sup>[103]</sup> and dimethyl dioxirane (DMDO), which was used for the preparation of a Pt oxo-complex.<sup>[104]</sup>

Screening reactions with the previously described complexes **1**, **2** and **3** were performed using the OAT reagents PyNO, mCPBA and DMDO (**Scheme 13**). The oxidants PyNO and mCPBA were purchased from commercial sources while DMDO was prepared according to literature procedures.<sup>[105]</sup>



**Scheme 13:** Screening reaction for the oxidation of the W(II)-precursors with the OAT reagents PyNO, mCPBA and DMDO.

#### 4.2.1. OAT reactions

The reaction conditions for the synthesis of the desired W(IV) oxo-species of the type  $[\text{WO}(\text{C}_2\text{R}_2)(\text{L3S})\text{Br}]$  ( $\text{R} = \text{Ph}, \text{Me}, \text{H}$ ) are summarized in **Table 8**. The CO-complexes **1 – 3** were dissolved in  $\text{CH}_2\text{Cl}_2$  and respective OAT reagent added in a solution of  $\text{CH}_2\text{Cl}_2$  (PyNO, mCPBA) or acetone (DMDO) at the corresponding temperature. Reaction mixtures were stirred for 5.5 h (PyNO), 4.0 h (DMDO) and 5 min to 30 min (mCPBA). The solvent was subsequently evaporated in vacuo and the reaction progress monitored with  $^1\text{H}$  NMR and IR spectroscopy.

**Table 8:** Reaction conditions for the oxidation of the complexes **1 – 3**.

Starting complex (SC)	OAT reagent	Solvents	Temperature	Reaction time
$[\text{W}(\text{CO})(\text{C}_2\text{Ph}_2)(\text{L3S})\text{Br}]$ ( <b>1</b> )	PyNO	$\text{CH}_2\text{Cl}_2$	$20\text{ }^\circ\text{C} \rightarrow 40\text{ }^\circ\text{C}$	5.5 h
	DMDO	$\text{CH}_2\text{Cl}_2/\text{acetone}$	$-30\text{ }^\circ\text{C} \rightarrow 20\text{ }^\circ\text{C}$	4.0 h
	mCPBA	$\text{CH}_2\text{Cl}_2$	$0\text{ }^\circ\text{C}$	5 min
$[\text{W}(\text{CO})(\text{C}_2\text{Me}_2)(\text{L3S})\text{Br}]$ ( <b>2</b> )	mCPBA	$\text{CH}_2\text{Cl}_2$	$0\text{ }^\circ\text{C}$	30 min
$[\text{W}(\text{CO})(\text{C}_2\text{H}_2)(\text{L3S})\text{Br}]$ ( <b>3</b> )	mCPBA	$\text{CH}_2\text{Cl}_2$	$0\text{ }^\circ\text{C}$	5 min

At  $20\text{ }^\circ\text{C}$  no conversion was observed for the reaction of complex **1** with PyNO. After heating the reaction mixture to reflux, a colorless solid, which was insoluble in  $\text{H}_2\text{O}$ , acetone,  $\text{CH}_3\text{CN}$  and apolar solvents, precipitated. Characterization by IR analysis showed several bands between  $800\text{ cm}^{-1}$  and  $1000\text{ cm}^{-1}$  identifying the precipitate as polyoxotungstate.<sup>[106]</sup>  $^1\text{H}$  NMR and IR analysis of the  $\text{CH}_2\text{Cl}_2$ -soluble fraction displayed only starting material ruling out the formation of a new species. Thus, PyNO is not considered a feasible oxidant for this complex-system.

The reaction of complex **1** with DMDO showed color changes from green to light blue at  $-30\text{ }^\circ\text{C}$  and from light blue to yellow when warmed to  $20\text{ }^\circ\text{C}$  (**Table 9**). Chemical shifts in  $^1\text{H}$  NMR spectroscopy indicated the formation of a new species. In addition to this, the CO band at  $1908\text{ cm}^{-1}$  of the starting material disappeared in the IR spectrum and new signals at  $1149\text{ cm}^{-1}$  and  $948\text{ cm}^{-1}$  were observed.

The oxidation of complex **1** using mCPBA displayed a similar color change from green over light blue ( $0\text{ }^\circ\text{C}$ ) to yellowish-green ( $20\text{ }^\circ\text{C}$ ) as observed in the reaction with DMDO.  $^1\text{H}$  NMR spectroscopy indicated the formation of two new species in a 2:1 ratio. Interestingly, the  $^1\text{H}$  NMR signals of the minor product matched the chemical shifts of the DMDO reaction product. IR analysis revealed several overlapping peaks between  $1920\text{ cm}^{-1}$  and  $1990\text{ cm}^{-1}$ .

Oxidation of complex **2** with mCPBA led to a color change from blue to pink. When recrystallized from CH<sub>2</sub>Cl<sub>2</sub>/heptane at -18 °C, <sup>1</sup>H NMR data indicated the formation of a new C<sub>2</sub>Me<sub>2</sub>-containing species. The methyl protons of the coordinated alkyne resonated downfield at 3.15 ppm and 3.36 ppm compared to signals at 3.07 ppm and 3.02 ppm of the starting material. The IR spectrum furthermore displayed a shift of the CO band from 1889 cm<sup>-1</sup> to 1929 cm<sup>-1</sup>. When performing the OAT reaction of mCPBA with complex **3**, an instant color change from light blue to yellow was observed. <sup>1</sup>H NMR analysis displayed new signals in the anticipated intensity-pattern, indicating the formation of a new W alkyne-complex. Most characteristic were the singlets of the acetylenic protons, which shifted downfield from 11.96 ppm and 12.93 ppm to 12.84 ppm and 13.73 ppm in CDCl<sub>3</sub>. A shift to higher energy from 1900 cm<sup>-1</sup> to 1923 cm<sup>-1</sup> was also observed for the CO-stretch in the IR spectrum. A distinctive signal for the W=O-vibration between 900 cm<sup>-1</sup> and 1000 cm<sup>-1</sup> could not be observed for any of the oxidation products with mCPBA.

**Table 9:** Optical and IR data for the OAT reactions.

Starting complex (SC)	OAT agent	Color(SC)	Color(RM <sup>a</sup> )	v(CO <sub>SM</sub> ) [cm <sup>-1</sup> ]	v(CO <sub>RM</sub> ) [cm <sup>-1</sup> ]
[W(CO)(C <sub>2</sub> Ph <sub>2</sub> )(L3S)Br] ( <b>1</b> )	PyNO	green	green	1908	1908
	DMDO	green	yellow	1908	-
	mCPBA	green	yellowish-green	1908	1921 <sup>b</sup>
[W(CO)(C <sub>2</sub> Me <sub>2</sub> )(L3S)Br] ( <b>2</b> )	mCPBA	blue	pink	1889	1929
[W(CO)(C <sub>2</sub> H <sub>2</sub> )(L3S)Br] ( <b>3</b> )	mCPBA	light blue	Yellow	1900	1923

<sup>a</sup> RM = reaction mixture; <sup>b</sup> most prominent among several peaks.

The absence of a CO-band after oxidation of complex **1** with DMDO and the IR signal at 948 cm<sup>-1</sup> indicate the formation of the desired W(IV)-complex [WO(C<sub>2</sub>Ph<sub>2</sub>)(L3S)Br]. However, the assumed oxo-signal occurs in an energy region where ligand vibrations are frequent. Thus, a modification on the L3S-ligand by DMDO causing signal shifts or the appearance of new peaks in this region should also be considered. One possibility of such an alteration is the oxidation of the thiolate to a sulfoxide- or sulfonyl-moiety. Schenk and co-workers reported the formation of sulfoxide-species by oxygen transfer of DMDO to Ru thioether-complexes.<sup>[107]</sup> IR analysis of sulfonyl-complexes furthermore showed vibration modes of the SO<sub>2</sub> group between 1040 cm<sup>-1</sup> and 1190 cm<sup>-1</sup>.<sup>[108]</sup> In agreement with this data, the signal at 1149 cm<sup>-1</sup> fits perfectly into the reported energy range supporting the idea of an oxidized sulfur-ligand.

$^1\text{H}$  NMR spectra for the reactions with mCPBA also displayed plausible signal patterns in the anticipated relative intensities of W oxo-complexes. While complexes **2** and **3** formed only one reaction product, two new species were observed in the screening reaction with complex **1**. However, the increased acidity of the acetylenic protons of complex **3** contradicts the upfield shift reported for coordinated acetylene in other W(IV)-complexes.<sup>[23,30]</sup> The coinciding chemical shifts of the minor product of the reaction with complex **1** with the oxidation product using DMDO furthermore indicates similar reaction-centers for both OAT reagents. Despite that, carbonyl signals were still present in the IR spectra of the oxidation products with mCPBA, but shifted to higher wave numbers. This indicates less  $\pi$ -backdonation from the W-center into the CO-ligand and therefore a potential alteration on the L3S-ligand to a more electron-deficient species in these complexes. Yet, oxidation to a sulfoxide- or sulfonyl-group is questionable since a prominent S-O vibration mode as observed for the oxidation with DMDO did not appear in the IR spectra. The formation of an oxo-species is also unlikely due to the absence of a W-O band.

In summary, the preparation of complexes of the type  $[\text{WO}(\text{C}_2\text{R}_2)(\text{L3S})\text{Br}]$  ( $\text{R} = \text{Ph}, \text{Me}, \text{H}$ ) was not successful when using PyNO and mCPBA as OAT reagents. The IR spectrum of the oxidation product of the complex  $[\text{W}(\text{CO})(\text{C}_2\text{Ph}_2)(\text{L3S})\text{Br}]$  (**1**) with DMDO displays a potential oxo-band at  $948\text{ cm}^{-1}$ . Additional oxidation of the S-donor ligand to a sulfonyl- or sulfoxide-moiety is suggested by the IR signal at  $1149\text{ cm}^{-1}$ . In order to fully identify the reaction product, analysis by  $^{13}\text{C}$  NMR spectroscopy, which could detect significant shifts in the  $\delta$ -values of the carbon-atoms adjacent to sulfoxide- or sulfonyl-groups, as well as X-ray crystal diffraction analysis will be required.

## 5. XAS-STUDY OF W ALKYNE-COMPLEXES

From the crystal structure and EPR studies of acetylene hydratase the active site of the enzyme was shown to involve a tungsten-center in oxidation state +IV.<sup>[14,15]</sup> Biomimetic complexes of the type  $[W(C_2H_2)L_2]$  are believed to exhibit a W(IV) metal-center as well. Yet, alkyne donation into empty metal d-orbitals and  $\pi$ -backdonation from the tungsten-center into  $\pi^*$ -orbitals of the triple-bond make the actual bonding interaction and the oxidation state of W hard to predict. In order to further understand the electronic structure of such complexes, tungsten L-edge and sulfur K-edge data were collected for W carbonyl- and W oxo-complexes of the type  $[W(CO)(C_2R_2)L_2]$  and  $[WO(C_2R_2)L_2]$  ( $R = H, Me, Ph$ ).<sup>[93,109]</sup> All investigated complexes exhibit C1 symmetry and possess two bidentate NS-donor ligands in a distorted octahedral coordination environment (**Figure 20**).

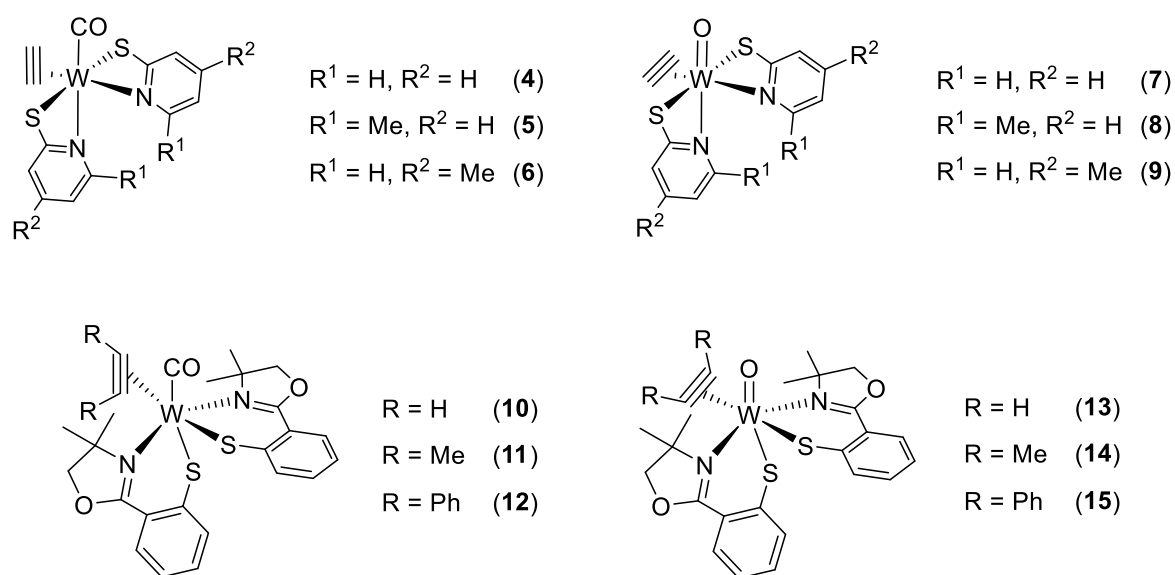


**Figure 20:** Schematic overview of CO- and oxo-complexes of the type  $[W(CO)(C_2R_2)L_2]$  and  $[WO(C_2R_2)L_2]$  with modifications on the NS-ligand or differing residues on acetylene.

The CO- and oxo-complexes **4 – 15** were provided by Carina Vidovic Msc for this work. XAS data was collected at the Stanford Synchrotron Radiation Lightsource (SSRL) and processed by Dr. Jing Yang at the University of New Mexico using the Demeter software suite and Athena. Sulfur K-edge pre-edge XAS computations were performed at the DFT level in the software ORCA using complex geometries based on the respective crystal structures.

### 5.1. XAS assessment of oxidation states

Overlays of the W L1-edges of the CO-complexes **4** – **6** and **10** – **12** as well as their oxo-analogs **7** – **9** and **13** – **15** are displayed in **Figure 21a** and **b**, respectively. Pre-edge and rising edge energies of these compounds show little to no variance within each series of complexes. A comparison of the W L1-edges of complexes **5** and **8**, representative of all probed CO- and oxo-complexes, is given in **Figure 21c**. Both the pre-edge and the rising edge are shifted to higher energy for the oxo-complex. From the first and second derivatives of the XANES spectra in **Figure 21d**, a difference of approximately 2 eV can furthermore be determined between the rising edge energies.

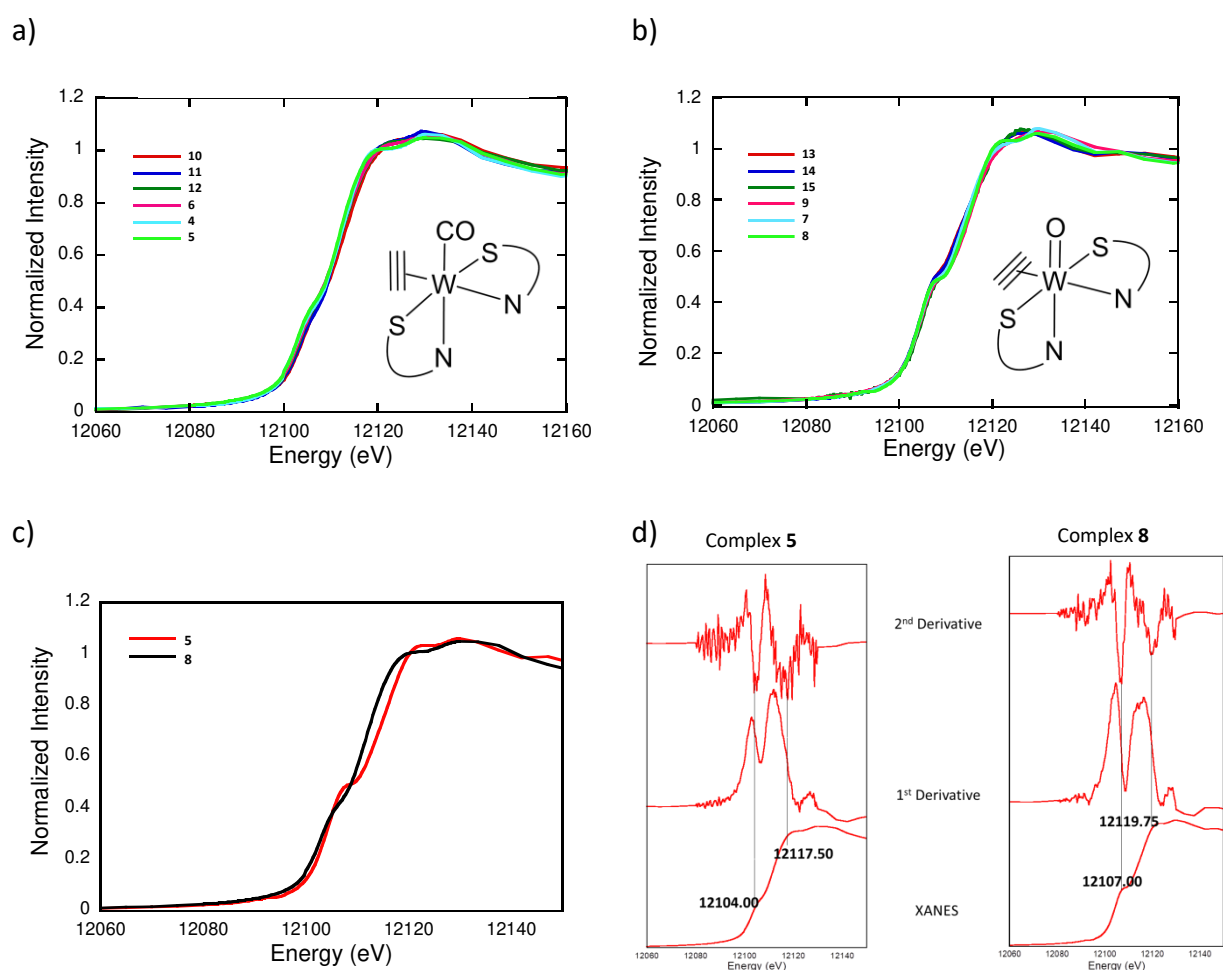


**Figure 21:** a) W L1-edge overlay of all CO-complexes; b) W L1-edge overlay of all oxo-complexes; c) W L1-edge overlay of complexes **5** (CO) and **8** (oxo); d) first and second derivative of the XANES region of complexes **5** and **8**.



The consistent pre-edge and rising edge energies within each series of carbonyl- and oxo-complexes indicates similar effective nuclear charges ( $Z^{\text{eff}}$ ) for W, as anticipated for compounds with identical first coordination spheres. When comparing the spectra of CO- and oxo-complexes, the higher pre-edge and rising edge energies for the oxo-compounds correlate with a higher  $Z^{\text{eff}}$  for W in the oxo-complexes. This is in accordance with the formally higher oxidation state of these compounds.

XAS-studies on metal-based redox-processes generally show an energy difference of approximately 1 eV between consecutive oxidation states in the K-edge spectra of first row transition metal elements.<sup>[110]</sup> A systematic study on a series of six-coordinate tungsten complexes with formal oxidation states ranging from 0 to +VI resulted in an approximate 0.5 eV rising edge energy difference per redox-step.<sup>[111]</sup> According to this, the ~2 eV shift between complexes **5** and **8** suggests a four d-electron count difference in the probed compounds, indicating oxidation states 0 or +II for the carbonyl- and +IV or +VI for the oxo-complex. This is not consistent with the formal oxidation states of +II and +IV for the CO- and the oxo-species. Considering that CO is a strong  $\pi$ -acceptor that withdraws electron density from the metal-center by  $\pi$ -backdonation, the suggested low oxidation state of W in the CO- compared to the oxo-complexes is surprising. In fact, spectral data of other CO-complexes displayed comparably high rising edge energies due to higher  $Z^{\text{eff}}$  of the metal-centers.<sup>[111]</sup> This was most noticeable in the spectra of the complexes  $[\text{W}^0(\text{PMe}_3)_6]$  and  $[\text{W}^0(\text{CO})_6]$ , which share the same formal oxidation state.<sup>[111]</sup> The rising edge of  $[\text{W}^0(\text{PMe}_3)_6]$ , which is coordinated by only  $\sigma$ -donating  $\text{PMe}_3$ -ligands, was approximately 3 eV lower in energy than the rising edge of  $[\text{W}^0(\text{CO})_6]$ , which bears  $\pi$ -accepting CO-groups.<sup>[111]</sup>

Extensive studies on dithiolene-complexes, which were probed due to their similarity to the pterin co-factor found in Mo- and W-enzymes, showed that the presence of a CO-ligand can lead to enhanced electron-donation of other  $\pi$ -donors in the ligand field.<sup>[111,112]</sup> This kind of electron-donation can partially reverse or even exceed the electron withdrawing effect of the CO-group.<sup>[111,112]</sup> In the case of  $\pi$ -donating dithiolene-ligands, the interaction with the metal-center is not exclusively described by W-S based MOs, but can also involve a 3-center-2-electron interaction of W-S based MOs with the  $\pi$ -accepting CO orbital (**Figure 22a**).<sup>[111,112]</sup> However, dithiolenes are known to be non-innocent ligands able to adopt redox states from

negatively charged dithiolate to fully oxidized dithione.<sup>[113]</sup> Yan and co-workers observed dithiolate character in  $[\text{W}(\text{CO})_4(\text{mdt})]$  ( $\text{mdt}^{2-} = 1,2\text{-dimethyl-1,2-dithiolate}$ ) and dithioketone character in  $[\text{W}(\text{CO})_4(\text{Me}_2\text{pipdt})]$  ( $\text{Me}_2\text{pipdt} = 1,4\text{-dimethylpiperazine-2,3-dithione}$ ) leading to different electronic structures of W in the overall isoelectronic complexes.<sup>[113]</sup> The W L1 rising edge of  $[\text{W}^{\text{II}}(\text{CO})_4(\text{mdt})]$  furthermore shifted to higher energy by 1.5 eV compared to  $[\text{W}^{\text{0}}(\text{CO})_4(\text{Me}_2\text{pipdt})]$ . This is surprising since  $[\text{W}(\text{CO})_4(\text{mdt})]$  exhibits an almost octahedral geometry allowing considerable  $\pi$ -backdonation into CO, whereas  $\text{Me}_2\text{pipdt}$  enforces a trigonal prismatic structure disfavoring  $\pi$ -orbital overlap between metal-center and the CO-ligands.

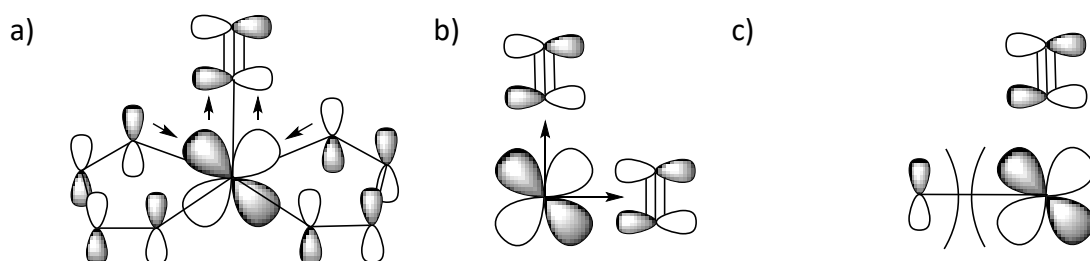


**Figure 22:** a) Dithiolene- $\pi$ -donating-CO- $\pi$ -accepting interaction in the HOMO-2 of  $[\text{W}^{\text{IV}}(\text{CO})_2(\text{mdt})_2]$ ;<sup>[113]</sup> b)  $\pi$ -backdonation into  $\pi^*$ -orbitals of acetylene and CO; c) repulsive interaction between the filled S  $p_z$ - and W  $d(xz/yz)$ -orbitals in CO-complexes of this work.

In regard to the complexes presented in this work, two sulfur-atoms as well as a side-on bound acetylene could act as potential  $\pi$ -donors toward W. However, in contrast to the dithiolene-CO interaction described above, acetylene is not involved in a  $\pi$ -donating- $\pi$ -accepting relationship with the CO-ligand, but competes with the carbonyl for the d-electrons of the metal-center (**Figure 22b**). DFT-generated molecular orbitals of complex **5** furthermore show that  $\pi$ -backdonation from W(II) into the anti-bonding  $\pi$ -orbitals of CO (HOMO) and acetylene (H-4) seems to occur via separate d-orbitals instead of a 3-center-2-electrons interaction (**Figure 23**).

In addition to this, H-1 is mostly composed of S  $p_z$ -character and a multi-center-bond between CO and S, as observed in dithiolene-complexes, is not generated. This is most likely due to repulsive interaction between the filled S  $p_z$ - and W  $d(xz/yz)$ -orbitals in the carbonyl-complexes (**Figure 22c**). The other S  $p_z$ -orbital of complex **5** is also not available for such an interaction since it is engaged in bonding with the pyridine ring. A possible bonding

interaction between the S  $p_y$ -orbital and the unoccupied W  $d(xy)$ -orbital seems unlikely due to the almost pure S  $p_y$ -character generated for H-2.

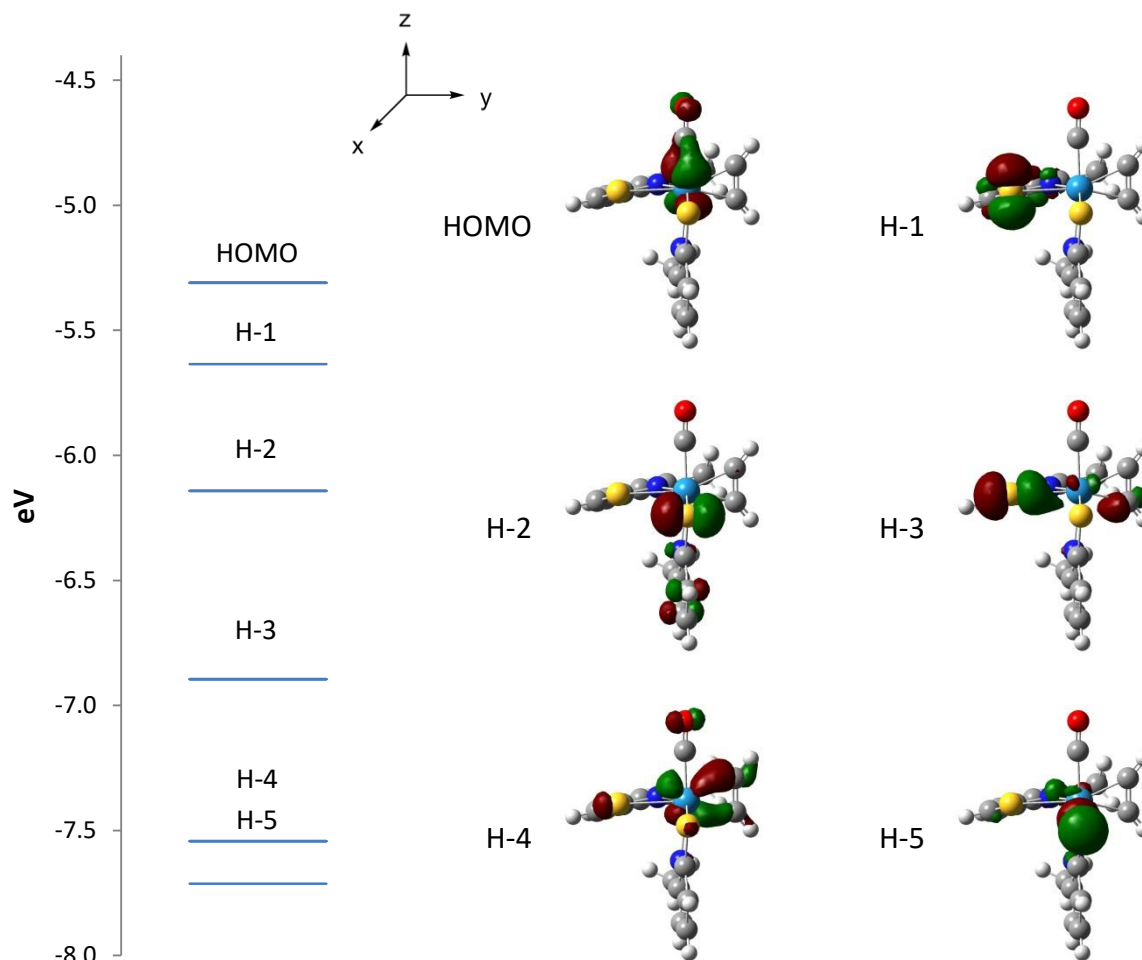


**Figure 23:** Molecular orbitals of complex 5.

In contrast to dithiolene-complexes, such as  $[W(CO)_2(mdt)_2]$ , the S-donors in the complexes of the type  $[W(CO)(C_2R_2)L_2]$  (**4 – 6**; **10 – 12**) are not able to tune  $\pi$ -backdonation of the W-center into  $\pi$ -accepting orbitals. In the corresponding oxo-complexes **7 – 9** and **13 – 15**, a repulsive interaction between the S  $p$ -orbitals and the W  $d(xy)$ -orbital is also assumed to prevent increased  $\pi$ -backdonation into the alkyne. However, no functional model of acetylene hydratase was prepared so far. Thus, only future research will tell whether dithiolene- or thiolate-ligands are more beneficial for acetylene hydration in a first-shell mechanistic proposal.

## 5.2. Pre-edge analysis

Formally dipole-forbidden transitions of the 2s core electrons into partially occupied or unoccupied d-orbitals are displayed at energies lower than the rising edge in the XANES region. Such pre-edge features were observed for both the CO- and oxo-complexes **4 – 15**. Yet, absorption intensities are more pronounced for the oxo-complexes. Computed W L1-edge XAS spectra based on TD-DFT calculations revealed that pre-edge intensities primarily arise from transitions into d-p-mixed W-orbitals of  $d(z^2)$ -character. Quadrupole-allowed contributions to the transition intensities were found to be small (**Figure 24**).

Enhanced pre-edge intensities of formally forbidden  $s \rightarrow nd$  transitions involving strong  $\pi$ -donors have been discussed in the literature.<sup>[114–116]</sup> Molybdenum oxo-species even showed a direct relationship between pre-edge peak intensities and the number of Mo=O-bonds.<sup>[116,117]</sup>

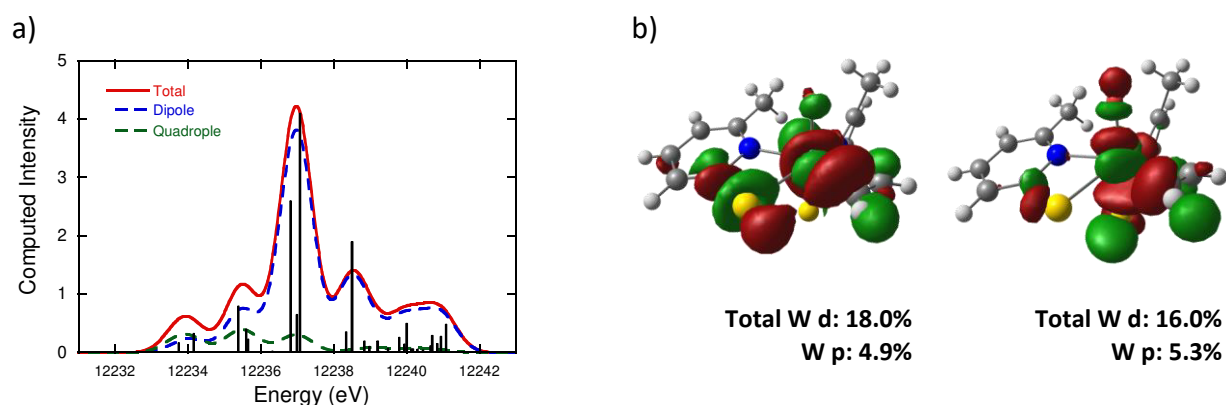


**Figure 24:** a) Curve fitting of the W L1-edge XAS of complex **8** displaying quadrupole and dipole allowed contributions to the peak intensity; b) accepting  $d(z^2)$ -based orbitals of the  $2s \rightarrow 5d$  transition.

The higher intensity of the pre-edge feature for the oxo-complexes suggests a greater  $d(z^2)$ - $p_z$  mixing in these compounds. Considerable d-p mixing with the energetically higher W 6p-orbitals is observed for the more destabilized the W  $d(z^2)$ -orbital. Since destabilization of the  $d(z^2)$ -orbital by the O 2p - W  $5d(z^2)$  interaction resulting from the W=O-bond is stronger than by  $\sigma$ -interaction with the CO-ligand, the pre-edge feature in the oxo-complexes is more pronounced.

### 5.3. Sulfur K-edge XAS

In order to better evaluate the collected W L-edge data, the complexes **4 – 15** were also probed by S K-edge XAS. Yet, the collected S K-edge data of complexes **10 – 15** was not conclusive and is therefore not further discussed. Crystal structures determined by X-ray diffraction analysis of the complexes **4 – 9** are depicted in **Figure 25**.

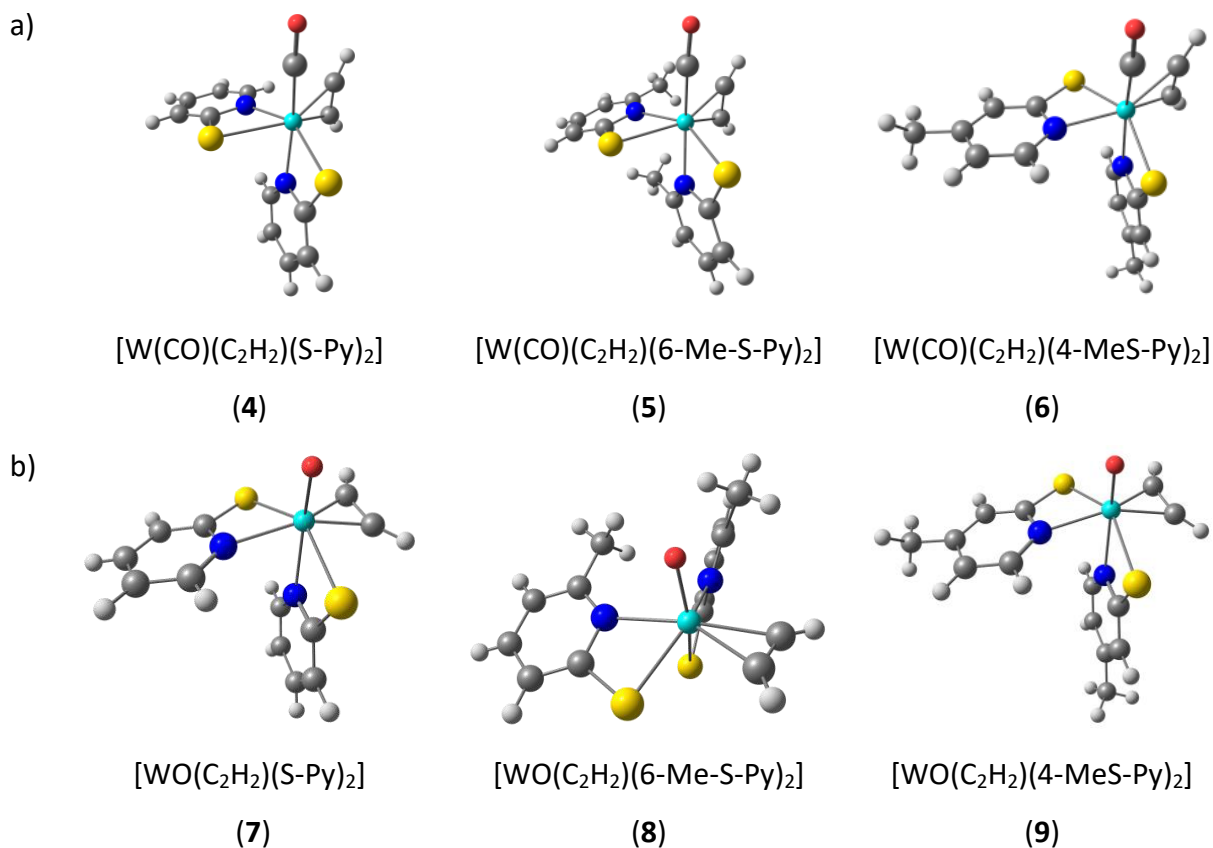


**Figure 25:** Crystal structures of the a) W CO-complexes **4 – 6** and b) W oxo-complexes **7 – 9**; W displayed in cyan, S displayed in yellow, N displayed in blue, O displayed in red.

Overlays of the sulfur K-edge XAS spectra of the three W carbonyl-complexes **4 - 6** and the three W oxo-complexes **7 – 9** are displayed in **Figure 26a** and **b**. Within the series of CO-complexes, complexes **4** and **5** show very similar spectra whereas complex **6** displays a less pronounced pre-edge feature and a slight shift by 0.2 eV of the rising edge to lower energies. For the oxo-compounds, the spectra of the complexes **7** and **9** are similar while the spectrum of **8** differs in pre-edge intensity as well as rising edge energy. Comparison between CO- and oxo-complexes furthermore revealed that rising edge energies are of up to 0.4 eV higher in the carbonyl complexes.

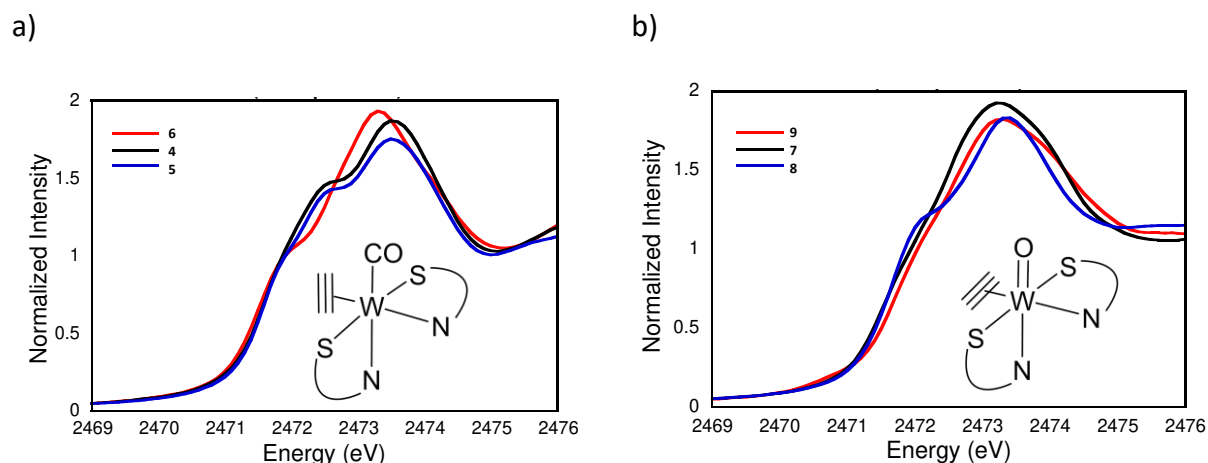


**Figure 26:** a) S K-edge overlay of CO-complexes **4 – 6** ; b) S K-edge overlay of oxo-complexes **7 - 9**.

Curve fitting supported by TD-DFT calculations was used to assign transitions to the observed energy absorption edges. For the CO-complexes, transitions to W  $d(xy)$ -,  $d(x^2-y^2/xz)$ - as well as other unoccupied, mostly ligand-based orbitals were identified. In the series of oxo-complexes the lowest available orbitals occupied by the ejected S 1s electron were W  $d(xz)$ - and  $d(x^2-y^2/xz)$ -based for complexes **7** as well as **9**, and W  $d(xz/yz)$ -,  $d(x^2-y^2)$ - and  $d(z^2)$ -based for complex **8**.

The energy, at which the rising edge appears in the spectrum, depends on the effective nuclear charge of the sulfur-atoms and shifts towards higher energy with increasing oxidation state.<sup>[112]</sup> The fact that the CO-complexes show rising edge energies of up to 0.4 eV higher than observed for the oxo-complexes therefore indicates less electron density localized at the sulfur-atoms in this series of compounds. Different oxidation levels for sulfur are not uncommon, especially if the ligands are redox non-innocent. W bis(dithiolene)-complexes, for instance, exhibit a 0.8 eV difference between the dithiolate- and dithione-redox state of the ligands.<sup>[112]</sup> Thus, higher  $Z^{\text{eff}}$  in the CO-complexes also indicates a more covalent character of the respective S-ligands.

Computationally determined transitions into W  $d(xy)$ - and  $d(x^2-y^2/xz)$ -based orbitals of the CO-complexes and W  $d(xz/yz)$ -,  $d(x^2-y^2)$ - and  $d(z^2)$ -orbitals of the oxo-complexes supports the formal oxidation states of +II and +IV for W in the CO- and oxo-compounds, respectively. The different acceptor orbitals within the oxo-series of complexes can furthermore be explained by the differing complex geometries. While the complexes  $[\text{WO}(\text{C}_2\text{H}_2)(\text{S-Py})_2]$  (**7**) and

[WO(C<sub>2</sub>H<sub>2</sub>)(4-MeS-Py)<sub>2</sub>] (**9**) both exhibit sulfur-atoms *trans* to each other and *cis* to the oxo-group, the complex [WO(C<sub>2</sub>H<sub>2</sub>)(6-Me-S-Py)<sub>2</sub>] (**8**) has one sulfur-donor *cis* and one sulfur-donor *trans* to the doubly-bonded oxygen-atom (**Figure 25**). In contrast to the former two complexes, which are geometrically aligned for orbital overlap of the S p<sub>z</sub>- with the W d(xz)-orbital and the S p<sub>x</sub>- with the W d(x<sup>2</sup>-y<sup>2</sup>)-orbital, the sulfur-atom *trans* to the oxo-ligand in complex **8** is directed toward the W d(z<sup>2</sup>)-orbital. This is expected to cause the additional interaction with the W d(yz)- and d(z<sup>2</sup>)-orbitals in this complex.

In summary, the collected S K-edge data is in agreement with the formal oxidation states of +II and +IV for W in the CO- (**4 – 6**) and oxo-complexes (**7 – 9**), respectively. This is particularly noteworthy since a +IV oxidation state is necessary to model the active site of AH. In contrast to these results, a four electron difference for the oxidation states of W was suggested by the W L1-edge rising-edge energies of CO- and oxo-complexes when compared to literature values. Yet, rising edge energies are sensitive to the ligand field, especially π-donating and π-accepting ligands. Thus, the comparison of the probed complexes with compounds featuring vastly different coordination spheres might explain the discrepancy between the oxidation states determined by S K-edge and W L-edge XAS.

#### 5.4. Tungsten-sulfur covalencies

In order to further understand the interaction between the W-center and the coordinated S-donor ligands, the amount of sulfur p-character (covalency,  $\alpha^2$ ) in the acceptor orbitals of the CO- and oxo-complexes **4 – 9** was quantified by the relationship shown in eq. 9.

$$D_0 = \alpha^2 \frac{hI_s}{3n} \quad (9)$$

Here,  $D_0$  describes the integrated absorption intensity,  $h$  represents the number of holes in the LUMO,  $I_s$  is the transition dipole integral ( $I_s = 11$ ) and  $n$  accounts for the number of absorbing sulfur-atoms. The calculated covalencies as well as selected bond lengths from X-ray diffraction analysis of complexes **4 – 9** are summarized in **Table 10**.

All complexes show covalencies over 25% with the W d(x<sup>2</sup>-y<sup>2</sup>/xz)-based orbital. For the CO-complexes, the S p-character in the unoccupied W d(xy)-S MO reaches up to 24%

whereas in the oxo-compounds the covalency in the anti-bonding MO containing S p- and W d(xz)-character is less than 20%. The listed crystallographic bond lengths show that S-atoms *trans* to N-donors exhibit the shortest W-S-distances of up to 2.418 Å. In the case of two sulfur-atoms *trans* to each other, the W-S-bond length ranges from 2.441 Å to 2.527 Å. W-S-distances, where S is *trans* to acetylene, are in the range of 2.584 Å to 2.601 Å. The longest bond is observed for the S-W-interaction *trans* to the oxo-group at 2.637 Å.

**Table 10:** Crystallographic and spectroscopic data on the S-W interaction

	Ligand <i>trans</i> to		bond lengths <sup>[93,109]</sup> [Å]		S K-edge XAS		
	S <sub>1</sub>	S <sub>2</sub>	S <sub>1</sub> -W	S <sub>2</sub> -W	edge <sup>a</sup> [eV]	covalency W d(xy)-S [%]	covalency W d(x <sup>2</sup> -y <sup>2</sup> /xz)-S [%]
apical CO							
<b>4</b>	acetylene	N	2.601	2.406	2473.5	17.5	25.6
<b>5</b>	acetylene	N	2.584	2.407	2473.5	15.3	36.5
<b>6</b>	S <sub>2</sub>	S <sub>1</sub>	2.479	2.479	2473.3	24.0	25.9
apical oxo							
<b>7</b>	S <sub>2</sub>	S <sub>1</sub>	2.516	2.439	2473.1	15.8	43.0
<b>8</b>	oxo	N	2.637	2.418	2473.3	14.7 <sup>b</sup>	26.1 <sup>c</sup> , 15.8 <sup>d</sup>
<b>9</b>	S <sub>2</sub>	S <sub>1</sub>	2.527	2.441	2473.1	19.1	70.4

<sup>a</sup> Defined as the rising edge inflection point determined by the second derivative of the XAS spectrum;

<sup>b</sup> covalency W d(xz/yz)-S [%]; <sup>c</sup> covalency W d(x<sup>2</sup>-y<sup>2</sup>)-S [%]; <sup>d</sup> covalency W d(z<sup>2</sup>)-S [%].

Higher S p-character in the W d(x<sup>2</sup>-y<sup>2</sup>/xz)-S MO is in good agreement with the idealized orbital arrangement in an octahedron featuring a d(x<sup>2</sup>-y<sup>2</sup>)-orbital directed toward the ligands in the octahedral plane. The fact that the S-W-interaction does not purely consist of an overlap of S p- and W d(x<sup>2</sup>-y<sup>2</sup>)-orbitals, but results in a molecular orbital with a considerable amount of W d(xz)-character suggests orbital mixing due to symmetry reduction in these complex geometries.

Little S p-character in the W d(xy)-S- and W d(xz)-S-acceptor orbitals is assumed to be a result of a weak  $\pi$ -interaction between S p<sub>y</sub>- and W d(xy)-orbitals as well as S p<sub>z</sub>- and W d(xz)-orbitals in CO- and oxo-complexes, respectively. This is in agreement with the almost pure S p<sub>y</sub>-orbital generated by DFT calculations for the complex [W(CO)(C<sub>2</sub>H<sub>2</sub>)(6-Me-S-Py)<sub>2</sub>] (**5**) in section 5.1. In the dithiolene-complex [W(CO)<sub>2</sub>(mdt)<sub>2</sub>] (mdt<sup>2-</sup> = 1,2-dimethyl-1,2-dithiolate), on the other hand, the S p-character of the S-W- $\pi$ -interacting LUMO is 67%.<sup>[112]</sup> This indicates increased electron density on the metal-center for  $\pi$ -backdonation in dithiolene-complexes compared to the probed thiolate-based complexes **4** – **9**.



It is also noteworthy that total covalencies are higher in the oxo-complexes when compared to the CO-complexes, which reflects a higher degree of S p- metal d-mixing in the former. This is due to energetically lower W d-orbitals in the W(IV) oxo-complexes and the higher oxidation state.

The W-S-bond lengths, which increase in the donor order  $N < S < \text{acetylene} < \text{oxo } \textit{trans} \text{ to } S$ , correlate with the ability of  $\pi$ -donation of the *trans*-ligand. Nitrogen-atoms are considered strict  $\sigma$ -donors, sulfur is an intermediate  $\sigma$ - and  $\pi$ -donor, acetylene can donate up to four  $\pi$ -electrons and the oxo-group has the strongest  $\pi$ -interaction with the W-center. The investigated complexes exhibit either S-atoms *trans* to each other or one S-atom *trans* to an N-donor and the other *trans* to a stronger  $\pi$ -donor, such as acetylene or an oxo-ligand. Therefore, the trend observed for the W-S-bond lengths cannot be clearly translated to the S p-character found in the W-S  $\pi$ -interacting W d(xy)-S- and W d(xz)-S-acceptor orbitals. However, the covalency values for these orbitals are pretty similar and range between 14.7% and 24.0%. This suggests that the total W-S  $\pi$ -interaction is roughly the same in complexes with intermediate  $\pi$ -donors *trans* to each other (**6**, **7** and **9**), and in complexes where the two sulfur-atoms are arranged *trans* to a N-donor and the acetylene- or oxo-ligand (**4**, **5** and **8**).

In conclusion, different degrees of W-S interaction can be observed when comparing the S K-edge data and molecular orbitals of the probed CO- and oxo-compounds to dithiolene-complexes, such as  $[\text{W}(\text{CO})_2(\text{mdt})_2]$ . While dithiolene-ligands display high covalencies of 67%, leading to additional  $\pi$ -backdonation into  $\pi$ -accepting orbitals, the W-S covalency of thiolate-ligands is reduced. Due to the lack of a functional model for AH, it is not yet clear, whether a closely coordinated alkyne by increased  $\pi$ -backdonation from a dithiolene-ligand or a  $\text{W-C}_2\text{R}_2$  adduct-character observed in thiolate-complexes is more beneficial for alkyne reactivity in first-shell mechanistic proposals. Therefore, both ligand-types should be considered in future biomimetic studies.

## CONCLUSION

Due to its unique reactivity among tungstoenzymes, determination of the still disputed reaction mechanism of acetylene hydratase is of particular interest. Computational results of second-shell mechanistic proposals inspired by the crystal structure of the enzyme displayed high energy barriers over 40 kcal/mol.<sup>[25]</sup> Thus, acetylene hydration in the W inner-sphere has also been investigated.<sup>[17,25]</sup> In order to determine the influence of acetylene activation by the metal-center in such a first-shell mechanistic proposal, a computational study on the W-assisted hydration of acetylene was conducted. The obtained energetic profile displayed an energy barrier of 49.6 kcal/mol, which is similar to the activation barrier of 53.1 kcal/mol calculated for the uncatalyzed reaction.<sup>[89]</sup> Furthermore, constrained dihedral angles between the two dithiolate-units as well as the SCH<sub>3</sub>-moiety and the W-acetylene-axis did not increase the energy of the starting complex sufficiently to significantly lower the energy barrier. Thus, acetylene activation by the metal-center seems not to be influential on the activation barriers associated with first-shell mechanisms.

Beside computational work, biomimetic model compounds are often essential to understand the reactivity of enzymes. For acetylene hydratase, three structural model compounds were reported in literature.<sup>[23,30,33]</sup> Catalytic activity of the only functional model was revoked by Schreyer and co-workers in 2017,<sup>[44]</sup> which makes the preparation of new structural and functional model complexes desirable. Starting from W(II)-precursors of the form [W(CO)(C<sub>2</sub>R<sub>2</sub>)(CH<sub>3</sub>CN)Br<sub>2</sub>] (R = Ph, Me, H), complexes employing the bio-inspired, heteroscorpionate L3S-ligand were synthesized via the "ligand addition" route. Elongation of the alkyne C-C-bond lengths in the complexes [W(CO)(C<sub>2</sub>Ph<sub>2</sub>)(L3S)Br] (**1**) and [W(CO)(C<sub>2</sub>Me<sub>2</sub>)(L3S)Br] (**2**) was determined by single crystal diffraction analysis. More activation of the C-C-bond in complex **1** than in complex **2** when compared to the C-C-distances in free alkynes indicated that  $\pi$ -backdonation in the diphenylacetylene-complex is enhanced due to the negative inductive effect of the phenyl-groups. This is in agreement with structural data collected for similar C<sub>2</sub>Me<sub>2</sub>- and C<sub>2</sub>Ph<sub>2</sub>-complexes. Comparison of the CO-frequencies in the different diphenylacetylene-complexes suggested low  $\pi$ -backdonation into the CO-ligand whereas the opposite was observed for the dimethylacetylene-compounds. Thus, reciprocal degrees of  $\pi$ -backdonation into the C<sub>2</sub>R<sub>2</sub>- (R = Ph, Me) and

CO-ligand seem to occur in correlation with the inductive effects of the alkyne-residues. Intermediate CO-frequencies in acetylene-complexes, on the other hand, did not result in the expected intermediate amounts of  $\pi$ -backdonation into the alkyne. Instead C-C-elongation compared to free  $C_2H_2$  indicated varying degrees of  $\pi$ -backdonation into the coordinated acetylene depending on the remaining ligand-set. Comparison of the complex  $[W(CO)(C_2H_2)(L3S)Br]$  (**3**) with other complexes of the type  $[W(CO)(C_2H_2)L_2]$  ( $L = S\text{-Phoz}, Tm^{Me}/Br, Tp^*/I$ ), showed contradictory trends in the  $^1H$  NMR and IR data revealing no overall trend regarding the electron-donating ability of the ligands.

In order to obtain biomimetically relevant W(IV)-complexes of the type  $[WO(C_2R_2)(L3S)Br]$  ( $R = Ph, Me, H$ ), oxidation reactions with the OAT reagents PyNO, mCPBA and DMDO were performed. Characterization of the reaction products by  $^1H$  NMR and IR spectroscopy ruled out PyNO as a suitable oxidant under the applied reaction conditions. The formation of new species was observed for complexes **1 – 3** using mCPBA and DMDO. However, spectroscopic data indicated oxidation of the L3S-based S-atom to a sulfoxide- or sulfonyl-moiety rather than the formation of the desired oxo-complex.

Depending on the amount of alkyne-donation and  $\pi$ -backdonation, formal oxidation states of W in biomimetic complexes of the form  $[WO(C_2R_2)L_2]$  can be defined as either +IV or +VI.<sup>[84]</sup> In order to further understand the electronic structure of these complexes, W L-edge and S K-edge XAS data of similar complexes of the type  $[W(CO)(C_2R_2)L_2]$  and  $[WO(C_2R_2)L_2]$  ( $R = Ph, Me, H$ ;  $L =$  bidentate N,S-donor ligands; **4 - 15**) were compared. Overlays of W L1-spectra revealed that the rising edge of the oxo-complexes is approximately 2 eV higher in energy compared to the CO-analogs. When compared to literature, this suggests a four electron difference in the oxidation states. However, fitting of the S K-edge data of the same complexes was in agreement with the anticipated oxidation states of +II for W in the CO- and +IV for W in the oxo-complexes.

In contrast to dithiolene-complexes, which interact extensively with the W-center, W-S-covalencies supported by DFT-calculations furthermore indicated only little W-S- $\pi$ -interaction in the probed complexes **4 – 9**. Additional  $\pi$ -backdonation into the alkyne by S-donating ligands is therefore unlikely for W-complexes with thiolate-based ligand-sets.

## EXPERIMENTAL SECTION

### 6. GENERAL INFORMATION ON COMPUTATIONAL METHODS

All calculations were performed at the density functional theory (DFT) level. Molecular geometries for the enzymatic model were based on the crystal structure of native acetylene hydratase (PDB ID code 2E7Z)<sup>[15]</sup> and fully optimized using the LANL2DZ basis set for all elements. Intermediates and transition states were identified as optimized geometries with zero and one imaginary frequencies, respectively.

### 7. GENERAL INFORMATION ON SYNTHETIC METHODS

All experiments were performed using standard Schlenk and Glovebox techniques under inert atmosphere of N<sub>2</sub> unless otherwise indicated. All reagents were purchased from commercial sources and used without further purification if not stated otherwise. Dry MeCN and CH<sub>2</sub>Cl<sub>2</sub> were prepared via a PureSolv solvent purification system. Heptane was dried over MgSO<sub>4</sub> and purged with N<sub>2</sub> for 2 h prior to use. THF was dehydrated by distillation over the Na/benzophenone ketyl system under N<sub>2</sub> atmosphere. Dry solvents were used in all reactions unless otherwise indicated.

All nuclear magnetic resonance spectra were recorded on a Bruker Avance III Solution spectrometer at 20°C. The residual solvent peak was set as internal standard. Coupling constants (*J*) are reported as absolute values in Hertz (Hz) and chemical shifts are quoted in parts per million (ppm). Multiplicities of peaks are given as broad singlet (bs), singlet (s), doublet (d), triplet (t) and multiplet (m). IR spectra were measured in the solid state using a Bruker Alpha-P FTIR spectrometer. Measurements for the determination of crystal structures were carried out using a graphite-monochromatized Mo K<sub>α</sub> radiation at 100K. Structures were solved by direct methods (SHELXS-97)<sup>[118]</sup> and refined by full-matrix least-squares techniques against *F*<sup>2</sup> (SHELXL-2014/6).<sup>[119]</sup> The non-hydrogen-atoms were refined with anisotropic displacement parameters without any constraints.

The L3SH ligand was prepared according to literature procedures.<sup>[79]</sup> The complexes of the type [W(CO)(C<sub>2</sub>R<sub>2</sub>)<sub>2</sub>(CH<sub>3</sub>CN)Br<sub>2</sub>] (R = Ph, Me, H) were provided by Carina Vidovic Msc.<sup>[93]</sup>

## 7.1. Experimental procedures

### 7.1.1. [W(CO)(C<sub>2</sub>Ph<sub>2</sub>)(L3S)Br] (1)

In a 50 mL Schlenk flask 103 mg L3SH (0.37 mmol, 1.3 equiv) were dissolved in 4.0 mL THF and 14.7 mg of a 60% dispersion of NaH in mineral oil (0.37 mmol, 1.3 equiv) were added. The reaction was stirred at 20 °C for 60 min. The THF-soluble phase was subsequently filtered into a suspension of 222 mg [W(CO)(C<sub>2</sub>Ph<sub>2</sub>)<sub>2</sub>(CH<sub>3</sub>CN)Br<sub>2</sub>] (0.29 mmol, 1.0 equiv) in 3 mL CH<sub>3</sub>CN. After 10 min the solvent was removed in vacuo. The residue was redissolved in 3 mL dry CH<sub>2</sub>Cl<sub>2</sub> and precipitated NaBr removed via filtration after 10 min. Evaporation of the solvent followed by flash chromatography (60 g silica gel, CH<sub>2</sub>Cl<sub>2</sub>/hexanes = 5/1, fraction size: 20 – 100 mL, in air) gave 43.3 mg of a green powder (0.06 mmol) in 20% yield.

<sup>1</sup>H NMR (300.13 MHz, CD<sub>2</sub>Cl<sub>2</sub>) δ = 7.18 – 7.52 (m, 10H, C<sub>2</sub>Ph<sub>2</sub>), 6.33 (s, 1H, C-H), 6.14 (s, 1H, C-H), 6.02 (s, 1H, C-H), 2.69 (s, 3H, CH<sub>3</sub>), 2.54 (s, 3H, CH<sub>3</sub>), 2.41 (s, 3H, CH<sub>3</sub>), 1.95 (s, 3H, CH<sub>3</sub>), 1.69 (s, 3H, CH<sub>3</sub>), 1.47 (s, 3H, CH<sub>3</sub>).

<sup>13</sup>C NMR (75.47 MHz, CD<sub>2</sub>Cl<sub>2</sub>) δ = 232.3 (CO), 203.7 (Cq, C≡C), 197.6 (Cq, C≡C), 157.1 (Cq), 153.1 (Cq), 142.3 (Cq), 142.3 (Cq), 141.6 (Ph), 138.9 (Cq), 129.1 (Ph), 128.9 (Ph), 128.5 (Ph), 127.6 (Ph), 109.7 (C-H), 108.7 (C-H), 76.7 (C-H), 52.8 (Cq), 32.9 (CH<sub>3</sub>), 29.8 (CH<sub>3</sub>), 17.5 (CH<sub>3</sub>), 17.3 (CH<sub>3</sub>), 12.1 (CH<sub>3</sub>), 12.0 (CH<sub>3</sub>).

IR: ν(CO) 1908 cm<sup>-1</sup>.

### 7.1.2. [W(CO)(C<sub>2</sub>Me<sub>2</sub>)(L3S)Br] (2)

In a 50 mL Schlenk flask 85.0 mg L3SH (0.31 mmol, 1.5 equiv) were dissolved in 3.5 mL THF and 13.5 mg of a 60% dispersion of NaH in mineral oil (0.33 mmol, 1.5 equiv) were added. The reaction was stirred at 20 °C for 30 min. The THF-phase was subsequently added dropwise to a suspension of 111 mg [W(CO)(C<sub>2</sub>Me<sub>2</sub>)<sub>2</sub>(CH<sub>3</sub>CN)Br<sub>2</sub>] (0.21 mmol, 1.0 equiv) in 3 mL CH<sub>3</sub>CN. After stirring at 20 °C for 15 min, the solvent was changed to CH<sub>2</sub>Cl<sub>2</sub> and precipitating NaBr was removed via filtration. The solution was then concentrated to approximately 1.0 mL and layered with 10.0 mL heptane. After 2 h the blue supernatant was

decanted and cooled to  $-18^{\circ}\text{C}$ . Repeated recrystallization from  $\text{CH}_2\text{Cl}_2$ /heptane led to 31.0 mg of light blue powder (0.05 mmol) in 24% yield.

$^1\text{H}$  NMR (300.13 MHz,  $\text{CDCl}_3$ )  $\delta$  = 6.26 (s, 1H, C-H), 6.17 (s, 1H, C-H), 5.95 (s, 1H, C-H), 3.07 (s, 3H,  $\text{C}_2\text{Me}_2$ ), 3.02 (s, 3H,  $\text{C}_2\text{Me}_2$ ), 2.70 (s, 3H,  $\text{CH}_3$ ), 2.55 (s, 3H,  $\text{CH}_3$ ), 2.48 (s, 3H,  $\text{CH}_3$ ), 2.36 (s, 3H,  $\text{CH}_3$ ), 1.43 (s, 3H,  $\text{CH}_3$ ), 1.21 (s, 3H,  $\text{CH}_3$ ).

$^{13}\text{C}$  NMR data not available due to decomposition of the complex in solution.

IR:  $\nu(\text{CO})$   $1889\text{ cm}^{-1}$ .

### 7.1.3. $[\text{W}(\text{CO})(\text{C}_2\text{H}_2)(\text{L3S})\text{Br}]$ (3)

In a 50 mL Schlenk flask 133 mg L3SH (0.48 mmol, 1.4 equiv) were dissolved in 4.0 mL THF and 18.0 mg of a 60% dispersion of NaH in mineral oil (0.48 mmol, 1.4 equiv) were added. The reaction mixture was stirred at  $20^{\circ}\text{C}$  until gas evolution ceased completely. The THF-soluble phase was subsequently filtered into a suspension of 160 mg  $[\text{W}(\text{CO})(\text{C}_2\text{H}_2)_2(\text{CH}_3\text{CN})\text{Br}_2]$  (0.34 mmol, 1.0 equiv) in 4 mL  $\text{CH}_3\text{CN}$ . After 15 min of stirring the solvent was removed in vacuo. The residue was dissolved in 3 mL  $\text{CH}_2\text{Cl}_2$  and stirred at  $20^{\circ}\text{C}$  until a colorless precipitate was observed. Salt fractions were removed via filtration and the crude product purified via flash chromatography in air (60 g silica gel,  $\text{CH}_2\text{Cl}_2$ , fraction size: 30 - 50 mL). Recrystallization from  $\text{CH}_2\text{Cl}_2$ /heptane gave 30.3 mg (0.05 mmol) of light blue powder in 15% yield.

$^1\text{H}$  NMR (300.13 MHz,  $\text{CD}_2\text{Cl}_2$ )  $\delta$  = 12.83 (s, 1H,  $\text{C}_2\text{H}_2$ ), 11.91 (s, 1H,  $\text{C}_2\text{H}_2$ ), 6.32 (s, 1H, C-H), 6.18 (s, 1H, C-H), 6.02 (s, 1H, C-H), 2.76 (s, 3H,  $\text{CH}_3$ ), 2.57 (s, 3H,  $\text{CH}_3$ ), 2.50 (s, 3H,  $\text{CH}_3$ ), 2.39 (s, 3H,  $\text{CH}_3$ ), 1.41 (s, 3H,  $\text{CH}_3$ ), 1.11 (s, 3H,  $\text{CH}_3$ ).

$^{13}\text{C}$  NMR (75.47 MHz,  $\text{CD}_2\text{Cl}_2$ )  $\delta$  = 232.4 (CO), 195.0 (Cq,  $\text{C}\equiv\text{C}$ ), 186.0 (Cq,  $\text{C}\equiv\text{C}$ ), 159.2 (Cq), 151.2 (Cq), 141.6 (Cq), 141.3 (Cq), 109.6 (C-H), 108.5 (C-H), 76.2 (C-H), 51.9 (Cq), 32.4 ( $\text{CH}_3$ ), 26.8 ( $\text{CH}_3$ ), 17.5 ( $\text{CH}_3$ ), 17.0 ( $\text{CH}_3$ ), 12.0 ( $\text{CH}_3$ ), 11.8 ( $\text{CH}_3$ ).

IR:  $\nu(\text{CO})$   $1900\text{ cm}^{-1}$ .

## 8. X-RAY ABSORPTION SPECTROSCOPY

The complexes of the type  $[W(CO)(C_2H_2)L_2]$  (L = S-Py (**4**), 6-Me-S-Py (**5**), 4-Me-S-Py (**6**)) and  $[WO(C_2H_2)L_2]$  (L = S-Py (**7**), 6-Me-S-Py (**8**), 4-Me-S-Py (**9**)) as well as  $[W(CO)(C_2R_2)(S-Phoz)_2]$  (R = H (**10**), Me (**11**), Ph (**12**)) and  $[WO(C_2R_2)(S-Phoz)_2]$  (R = H (**13**), Me (**14**), Ph (**15**)) were provided by Carina Vidovic Msc.

### 8.1. W L-edge XAS

W L-edge X-ray absorption spectroscopic data were collected on beamline 7-3 at the Stanford Synchrotron Radiation Lightsource (SSRL) with the SPEAR storage ring containing 200–300 mA at 3.0 GeV. Beamline 7-3 is equipped with rhodium-coated mirrors upstream and downstream of the Si(220) double-crystal monochromator. The incident and transmitted X-ray intensities ( $I_0$ ,  $I_1$ , and  $I_2$ ) were monitored with three nitrogen filled ionization chambers. The sample temperature was maintained at 10 K using an Oxford Instruments CF1208 continuous flow liquid helium cryostat. Samples were made using 4 mg of compound that was finely ground with 36 mg of BN powder. The samples were subsequently sealed in the sample holder using sulfur-free Kapton tape. Data were collected in fluorescence mode using a Lytle detector. A Zn-3 filter and a Soller slit were used before the detector to reject the scattered radiation. The internal energy was calibrated using a W foil reference with the first inflection point set to 10,207 eV for the W L3 edge, 11,544 eV for the L2 edge, and 12,100 eV for the L1 edge. The scan ranges were 9,885 – 11,326 eV for the L3, 11,300 -12,000 for the L2, and 11,900 – 12,300 eV for the L1 edges. The spectra reported here are averaged with two sweeps.

### 8.2. S K-edge XAS

Sulfur K-edge XAS spectra were collected on beamline 4-3 at SSRL. BL4-3 is equipped with a liquid-nitrogen-cooled Si(111) double crystal monochromator. The samples were prepared using a ground powder-on-tape protocol. The sample holder with powder-smear tape was placed in a helium-gas-purged sample chamber. All measurements were collected using the

passivated implanted planar silicon (PIPS) fluorescence detector at room temperature. The first pre-edge peak of  $\text{Na}_2\text{S}_2\text{O}_3 \cdot 5\text{H}_2\text{O}$  was assigned as 2472.02 eV in order to calibrate the beam energy. The spectra reported here are averaged with four sweeps.

### **8.3. XAS Data Processing**

XAS data were processed using the Demeter software suite (version 0.9.25). The XANES spectra were calibrated, background smoothed, and normalized in Athena with the threshold energy assigned as 10,207 eV for the W L3-, 11,544 eV for L2-, 12,100 eV for L1- and 2,472 eV for the S K-edge. The pre-edge features for all S K-edge data were fitted using the Peakfitting Mode in Athena with one arctangent step line and several pseudo-Voigt peaks. All the pseudo-Voigt peak energies were determined by plotting the data as the second derivative and using the valley energies.

### **8.4. XAS TDDFT calculations**

All S K-edge pre-edge XAS computations were performed at the density functional theory (DFT) level in the software ORCA (version 4.0.0) with structures based on the crystal structures without further optimization. The B3LYP/G functional, the zero-order regular approximation (ZORA) were adopted, and the associated ZORA-def2-TZVP basis set was used for light atoms, the ZORA-def2-TZVPP basis set for S-atoms, and the SARC-ZORA-TZVP basis set was used for W.



## REFERENCES

- [1] R. H. Holm, P. Kennepohl, E. I. Solomon, *Chem. Rev.* **1996**, *96*, 2239–2314.
- [2] L. E. Bevers, P.-L. Hagedoorn, W. R. Hagen, *Coord. Chem. Rev.* **2009**, *253*, 269–290.
- [3] R. Hille, *Trends Biochem. Sci.* **2002**, *27*, 360–367.
- [4] A. Kletzin, M. W. W. Adams, *FEMS Microbiol. Rev.* **1996**, *18*, 5–63.
- [5] V. Cameron, C. H. House, S. L. Brantley, *Archaea* **2012**, 12 pages.
- [6] R. J. P. Williams, J. J. R. Fraústo Da Silva, *J. Theor. Biol.* **2003**, *220*, 323–343.
- [7] C. W. Cady, R. H. Crabtree, G. W. Brudvig, *Coord. Chem. Rev.* **2008**, *252*, 444–455.
- [8] B. K. Burgess, *Chem. Rev.* **1990**, *90*, 1377–1406.
- [9] A. K. Rines, H. Ardehali, *J. Mol. Cell. Cardiol.* **2013**, *55*, 50–57.
- [10] M. K. Johnson, D. C. Rees, M. W. W. Adams, *Chem. Rev.* **1996**, *96*, 2817–2839.
- [11] M. Boll, O. Einsle, U. Ermler, P. M. H. Kroneck, G. M. Ullmann, *J. Mol. Microbiol. Biotechnol.* **2016**, *26*, 119–137.
- [12] B. Schink, *Arch. Microbiol.* **1985**, *142*, 295–301.
- [13] B. M. Rosner, B. Schink, *J. Bacteriol.* **1995**, *177*, 5767–5772.
- [14] R. U. Meckenstock, R. Krieger, S. Ensign, P. M. H. Kroneck, B. Schink, *Eur. J. Biochem.* **1999**, *264*, 176–182.
- [15] G. B. Seiffert, G. M. Ukkmann, A. Messerschmidt, B. Schink, P. M. H. Kroneck, O. Einsle, *Proc. Natl. Acad. Sci. U.S.A.* **2007**, *104*, 3073–3077.
- [16] P. M. H. Kroneck, *J. Biol. Inorg. Chem.* **2016**, *21*, 29–38.
- [17] R.-Z. Liao, J.-G. Yu, F. Himo, *Proc. Natl. Acad. Sci. U.S.A.* **2010**, *107*, 22523–22527.
- [18] M. R. Hyman, D. J. Arp, *Anal. Biochem.* **1988**, *173*, 207–220.
- [19] J. M. Rivera-Ortiz, R. H. Burris, *J. Bacteriol.* **1975**, *123*, 537–545.
- [20] R. W. F. Hardy, R. D. Holsten, E. K. Jackson, R. C. Burns, *Plant Physiol.* **1968**, *43*, 1185–1207.
- [21] L. G. Miller, S. M. Baesman, J. Kirshtein, M. A. Voytek, R. S. Oremland, *Geomicrobiol. J.* **2013**, *30*, 501–516.
- [22] F. tenBrink, B. Schink, P. M. H. Kroneck, *J. Bacteriol.* **2011**, *193*, 1229–1236.
- [23] L. M. Peschel, F. Belaj, N. C. Mösch-Zanetti, *Angew. Chem., Int. Ed.* **2015**, *54*, 13018–13021.
- [24] S. Antony, C. A. Bayse, *Organometallics* **2009**, *28*, 4938–4944.
- [25] M. A. Vincent, I. H. Hillier, G. Periyasamy, N. A. Burton, *Dalton Trans.* **2010**, *39*, 3816–3822.
- [26] W. T. R.-Z. Liao, *J. Chem. Theory Comput.* **2012**, *8*, 3793–3803.
- [27] S. J. Mole, X. Zhou, R. Liu, *J. Phys. Chem.* **1996**, *100*, 14665–14671.
- [28] T. N. Sorrell, *Organic chemistry*, University Science Books, Sausalito, Calif., **1999**.
- [29] H. G. Alt, H. I. Hayen, *J. Organomet. Chem.* **1986**, *316*, 105–119.
- [30] J. L. Templeton, B. C. Ward, G. J.-J. Chen, J. W. McDonald, W. E. Newton, *Inorg. Chem.* **1981**, *20*, 1248–1253.
- [31] L. M. Peschel, C. Vidovic, F. Belaj, D. Neshchadin, N. C. Mösch-Zanetti, *Chem. Eur. J.* **2019**, *25*, 3893–3902.
- [32] M. Kersting, A. El-Kholi, U. Müller, K. Dehnicke, *Chem. Ber.* **1989**, *122*, 279–285.
- [33] T. W. Crane, P. S. White, J. L. Templeton, *Organometallics* **1999**, *18*, 1897–1903.
- [34] T. W. Crane, P. S. White, J. L. Templeton, *Inorg. Chem.* **2000**, *39*, 1081–1091.
- [35] M. G. B. Drew, *Prog. Inorg. Chem.* **1977**, *23*, 67–210.

- [36] J. L. Templeton, *Adv. Chem. Ser.* **1979**, *173*, 263–278.
- [37] W. T. R.-Z. Liao, *J. Phys. Chem. B* **2013**, *117*, 3954–3961.
- [38] N. Kitajima, K. Fujisawa, C. Fujimoto, Y. Moro-oka, S. Hashimoto, T. Kitagawa, K. Toriumi, K. Tatsumi, A. Nakamura, *J. Am. Chem. Soc.* **1992**, *114*, 1277–1291.
- [39] N. Kitajima, K. Fujisawa, Y. Moro-oka, *J. Am. Chem. Soc.* **1989**, *111*, 8976–8978.
- [40] R. Burth, A. Stange, M. Schäfer, H. Vahrenkamp, *Eur. J. Inorg. Chem.* **1998**, *11*, 1759–1764.
- [41] T. C. Higgs, C. J. Carrano, *Inorg. Chem.* **1997**, *36*, 298–306.
- [42] S. K. Das, D. Biswas, R. Maiti, S. Sarkar, *J. Am. Chem. Soc.* **1996**, *118*, 1387–1397.
- [43] J. Yadav, S. K. Das, S. Sarkar, *J. Am. Chem. Soc.* **1997**, *119*, 4315–4316.
- [44] L. H. M. Schreyer, *Beilstein J. Org. Chem.* **2017**, *13*, 2332–2339.
- [45] D. C. Harris, M. D. Bertolucci, *Symmetry and Spectroscopy. An Introduction to Vibrational and Electronic Spectroscopy*, Oxford University Press, New York, **1978**.
- [46] I. V. Hertel, C.-P. Schulz (Ed.) *Atoms, Molecules and Optical Physics 1. Atoms and Spectroscopy*, Springer-Verlag, Berlin Heidelberg, **2015**.
- [47] N. Grover, N. Chaudhri, M. Sankar, *Inorg. Chem.* **2019**, *58*, 2514–2522.
- [48] L. Schnaubelt, H. Petzold, G. Hörner, T. Ruffer, N. Klein, H. Lang, *Eur. J. Inorg. Chem.* **2019**, *7*, 988–1001.
- [49] L. J. Giles, C. Ruppelt, J. Yang, R. R. Mendel, F. Bittner, M. L. Kirk, *Inorg. Chem.* **2014**, *53*, 9460–9462.
- [50] J. Yano, V. K. Yachandra, *Photosynth Res* **2009**, *102*, 241–254.
- [51] A. J. Cruz, K. Siam, D. P. Rillema, *J. Phys. Chem. A* **2011**, *115*, 1108–1116.
- [52] D. M. L. Goodgame, M. Goodgame, F. A. Cotton, *J. Am. Chem. Soc.* **1961**, *83*, 4161–4167.
- [53] G. Y. Zheng, D. P. Rillema, J. DePriest, C. Woods, *Inorg. Chem.* **1998**, *37*, 3588–3592.
- [54] R. M. Breece, A. Costello, B. Bennett, T. K. Sigdel, M. L. Matthews, D. L. Tierney, M. W. Crowder, *J. Biol. Chem.* **2005**, *280*, 11074–11081.
- [55] J. E. Hahn, R. A. Scott, K. O. Hodgson, S. Doniach, S. R. Desjardins, E. I. Solomon, *Chem. Phys. Lett.* **1982**, *88*, 595–598.
- [56] H. Wang, G. Peng, L. M. Miller, E. M. Scheuring, S. J. George, M. R. Chance, S. P. Cramer, *J. Am. Chem. Soc.* **1997**, *119*, 4921–4928.
- [57] S. D. J. Kowalska, *Biochim. Biophys. Acta* **2015**, *1835*, 1406–1415.
- [58] O. Kleifeld, A. Frenkel, J. M. L. Martin, I. Sagi, *Nat. Struct. Biol.* **2003**, *10*, 98–103.
- [59] M. Grossman, N. Sela-Passwell, I. Sagi, *Curr. Opin. Struct. Biol.* **2011**, *21*, 678–685.
- [60] A. Solomon, B. Akabayov, A. Frenkel, M. E. Milla, I. Sagi, *Proc. Natl. Acad. Sci. U.S.A.* **2007**, *104*, 4931–4936.
- [61] I. Sagi, M. E. Milla, *Anal. Biochem.* **2008**, *372*, 1–10.
- [62] D. R. Gisewhite, J. Yang, B. R. Williams, A. Esmail, B. Stein, M. L. Kirk, S. J. N. Burgmayer, *J. Am. Chem. Soc.* **2018**, *140*, 12808–12818.
- [63] Y. Ha, A. L. Tenderholt, R. H. Holm, B. Hedman, K. O. Hodgson, E. I. Solomon, *J. Am. Chem. Soc.* **2014**, *136*, 9094–9105.
- [64] C. Garinoa, E. Borfecchia, R. Gobetto, J. A. van Bokhoven, C. Lamberti, *Coord. Chem. Rev.* **2014**, *277–278*, 130–186.
- [65] C. R. Randall, L. Shu, Y.-M. Chiou, K. S. Hagen, M. Ito, N. Kitajima, R. J. Lachicotte, Y. Zang, L. Que, Jr., *Inorg. Chem.* **1995**, *34*, 1036–1039.

- [66] P. P. Samuel, S. Horn, A. Döring, K. G. V. Havelius, S. Reschke, S. Leimkühler, M. Haumann, C. Schulzke, *Eur. J. Inorg. Chem.* **2011**, *28*, 4387–4399.
- [67] M. C. Corbett, F. Akif Tezcan, O. Einsle, M. Y. Walton, D. C. Rees, M. J. Latimer, B. Hedmand, K. O. Hodgson, *J. Synchrotron Rad.* **2005**, *12*, 28–34.
- [68] V. W. Hu, S. I. Chan, G. S. Brown, *Proc. Natl. Acad. Sci. U.S.A.* **1977**, *74*, 3821–3825.
- [69] C. Milsmann, S. Sproules, E. Bill, T. Weyhermüller, S. DeBeer George, K. Wieghardt, *Chem. Eur. J.* **2010**, *16*, 3628–3645.
- [70] A. L. Roe, D. J. Schneider, R. J. Mayer, J. W. Pyrz, J. Widom, L. Que, Jr., *J. Am. Chem. Soc.* **1984**, *106*, 1676–1681.
- [71] T. E. Westre, P. Kennepohl, J. G. DeWitt, B. Hedman, K. O. Hodgson, E. I. Solomon, *J. Am. Chem. Soc.* **1997**, *119*, 6297–6314.
- [72] R. G. Shulman, Y. Yafet, P. Eisenberger, W. E. Blumberg, *Proc. Natl. Acad. Sci. U.S.A.* **1976**, *73*, 1384–1388.
- [73] S. E. Shadle, B. Hedman, K. O. Hodgson, E. I. Solomon, *J. Am. Chem. Soc.* **1995**, *117*, 2259–2272.
- [74] T. Glaser, B. Hedman, K. O. Hodgson, E. I. Solomon, *Acc. Chem. Res.* **2000**, *33*, 859–868.
- [75] R. K. Szilagy, B. S. Lim, T. Glaser, R. H. Holm, B. Hedman, K. O. Hodgson, E. I. Solomon, *J. Am. Chem. Soc.* **2003**, *125*, 9158–9169.
- [76] R. K. Szilagy, E. I. Solomon, *Curr. Opin. Chem. Biol.* **2002**, *6*, 250–258.
- [77] R. K. Szilagy, M. Metz, E. I. Solomon, *J. Chem. Phys. A* **2002**, *106*, 2994–3007.
- [78] B. S. Hammes, C. J. Carrano, *Inorg. Chem.* **1999**, *38*, 4593–4600.
- [79] B. S. Hammes, C. J. Carrano, *Chem. Comm.* **2000**, *0*, 1635–1636.
- [80] B. S. Hammes, C. J. Carrano, *J. Chem. Soc., Dalton Trans.* **2000**, *0*, 3304–3309.
- [81] B. S. Hammes, C. J. Carrano, *Inorg. Chem.* **2001**, *40*, 919–927.
- [82] C. J. Carrano, B. S. Chohan, B. S. Hammes, B. W. Kail, V. N. Nemykin, P. Basu, *Inorg. Chem.* **2003**, *42*, 5999–6007.
- [83] K. Peariso, B. S. Chohan, C. J. Carrano, M. L. Kirk, *Inorg. Chem.* **2003**, *42*, 6194–6203.
- [84] K. H. Theopold, S. J. Holmes, R. R. Schrock, *Angew. Chem.* **1983**, *95*, 1012–1013.
- [85] P. L. Holland, *Dalton Trans.* **2010**, *39*, 5415–5425.
- [86] M. B. Wells, J. E. McConathy, P. S. White, J. L. Templeton, *Organometallics* **2002**, *21*, 5007–5020.
- [87] S. G. Feng, A. S. Gamble, C. C. Philipp, P. S. White, J. L. Templeton, *Organometallics* **1991**, *10*, 3504–3512.
- [88] J. L. Caldarelli, P. S. White, J. L. Templeton, *J. Am. Chem. Soc.* **1992**, *114*, 10097–10103.
- [89] Y.-F. Liu, R.-Z. Liao, W.-J. Ding, J.-G. Yu, R.-Z. Liu, *J. Biol. Inorg. Chem.* **2011**, *16*, 745–752.
- [90] R.J.P. Williams, *Inorg. Chim. Acta Rev.* **1971**, *5*, 137–155.
- [91] G. S. Hammond, *J. Am. Chem. Soc.* **1955**, *77*, 334–338.
- [92] R. L. McNaughton, M. E. Helton, M. Mader Cospere, J. H. Enemark, M. L. Kirk, *Inorg. Chem.* **2004**, *43*, 1625–1637.
- [93] C. Vidovic, *Master Thesis*, **2016**.
- [94] D. S. Frohnapfel, S. Reinartz, P. S. White, J. L. Templeton, *Organometallics* **1998**, *17*, 3759–3769.
- [95] M. B. Wells, P. S. White, J. L. Templeton, *Organometallics* **1997**, *16*, 1857–1864.
- [96] T. Zuschneid, H. Fischer, T. Handel, K. Albert, G. Häfelinger, *Z. Naturforsch., B: Chem. Sci.* **2004**, *59*, 1153–1176.
- [97] Y. Suenaga, L. P. Wu, T. Kuroda-sowa, M. Munakata, M. Maekawa, *Polyhedron* **1997**, *16*, 67–70.
- [98] J. L. Templeton, B. C. Ward, *J. Am. Chem. Soc.* **1980**, *102*, 3288–3290.

- [99] A. Mavridis, I. Moustakali-Mavridis, *Acta. Crystallogr., Sect. B: Struct. Sci.* **1977**, *33*, 3612–3615.
- [100] B. P. E. Pignataro, *Acta. Crystallogr.* **1955**, *8*, 672–674.
- [101] R. K. McMullan, Å. Kvik, P. Popelier, *Acta. Crystallogr., Sect. B: Struct. Sci.* **1992**, *48*, 726–731.
- [102] C. K. Johnson, *ORTEP. Report ORNL-3794*, Tennessee, USA, **1965**.
- [103] C. Khosla, A. B. Jackson, P. S. White, J. L. Templeton, *Organometallics* **2012**, *31*, 987–994.
- [104] E. Poverenov, I. Efremenko, A. I. Frenkel, Y. Ben-David, L. J. W. Shimon, G. Leitus, L. Konstantinovski, J. M. L. Martin, D. Milstein, *Nature* **2008**, *455*, 1093–1096.
- [105] D. F. Taber, P. W. DeMatteo, R. A. Hassan, *Org. Synth.* **2013**, *90*, 350–357.
- [106] P. I. Molina, D. J. Sures, P. Miró, L. N. Zakharov, M. Nyman, *Dalton Trans.* **2015**, *44*, 15813–15822.
- [107] W. A. Schenk, B. Steinmetz, M. Hagel, W. Adamb, C. R. Saha-Möller, *Z. Naturforsch., B: Chem. Sci.* **1997**, *52b*, 1359–1371.
- [108] J. I. de la Cruz-Cruz, M. A. Paz-Sandoval, *J. Organomet. Chem* **2015**, *791*, 107–108.
- [109] M. Buchsteiner, *unpublished results*.
- [110] K. W. S. Sproules, *Coord. Chem. Rev.* **2011**, *255*, 837–860.
- [111] U. Jayarathne, P. Chandrasekaran, A. F. Greene, J. T. Mague, S. DeBeer, K. M. Lancaster, S. Sproules, J. P. Donahue, *Inorg. Chem.* **2014**, *53*, 8230–8241.
- [112] Y. Yan, C. Keating, P. Chandrasekaran, U. Jayarathne, J. T. Mague, S. DeBeer, K. M. Lancaster, S. Sproules, I. V. Rubtsov, J. P. Donahue, *Inorg. Chem.* **2013**, *52*, 6743–6751.
- [113] Y. Yan, P. Chandrasekaran, J. T. Mague, S. DeBeer, S. Sproules, J. P. Donahue, *Inorg. Chem.* **2012**, *51*, 346–361.
- [114] S. DeBeer George, P. Brant, E. I. Solomon, *J. Am. Chem. Soc.* **2005**, *127*, 667–674.
- [115] F. A. Lima, R. Bjornsson, T. Weyhermüller, P. Chandrasekaran, P. Glatzel, F. Neese, S. DeBeer, *Phys. Chem. Chem. Phys.* **2013**, *15*, 20911–20920.
- [116] S. P. Cramer, K. O. Hodgson, W. O. Gillum, L. E. Mortenson, *J. Am. Chem. Soc.* **1978**, *100*.
- [117] S. P. Cramer, W. O. Gillum, K. O. Hodgson, L. E. Mortenson, E. I. Stiefel, J. R. Chisnell, W. J. Brill, V. K. Shah, *J. Am. Chem. Soc.* **1978**, *100*, 3814–3819.
- [118] G. M. Sheldrick, *Acta Crystallogr., Sect. A: Found.* **2008**, *64*, 112–122.
- [119] G. M. Sheldrick, *Acta Crystallogr., Sect. C: Cryst. Struct.* **2015**, *71*, 3–8.

## APPENDIX

**Table 11:** Crystal data and structure refinement for [W(CO)(C<sub>2</sub>R<sub>2</sub>)(L3S)Br] (R = Ph (1), Me (2)).

Crystal data	[W(CO)(C <sub>2</sub> Ph <sub>2</sub> )(L3S)Br] (1)	[W(CO)(C <sub>2</sub> Me <sub>2</sub> )(L3S)Br] (2)
Empirical formula	C <sub>29</sub> H <sub>31</sub> BrN <sub>4</sub> OSW	C <sub>19</sub> H <sub>27</sub> BrN <sub>4</sub> OSW · CH <sub>2</sub> Cl <sub>2</sub>
Formula weight	747.40	708.19
Crystal description	block, green	block, blue
Crystal size	0.44 x 0.31 x 0.27 mm	0.58 x 0.44 x 0.29 mm
Crystal system, space group	monoclinic, P 2 <sub>1</sub> /c	monoclinic, P 2 <sub>1</sub> /c
Unit cell dimensions:		
a	10.5126(15) Å	9.0023(12) Å
b	17.533(3) Å	23.229(3) Å
c	15.746(2) Å	11.9693(16) Å
β	107.049(3)°	96.982(4)°
Volume	2774.8(7) Å <sup>3</sup>	2484.4(6) Å <sup>3</sup>
Z	4	4
Calculated density	1.789 Mg/m <sup>3</sup>	1.893 Mg/m <sup>3</sup>
F(000)	1464	1376
Linear absorption coefficient μ	5.708 mm <sup>-1</sup>	6.577 mm <sup>-1</sup>
Absorption correction	semi-empirical from equivalents	semi-empirical from equivalents
Max. and min. transmission	0.746 and 0.540	1.000 and 0.628
Unit cell determination	2.34° < θ < 31.97°	2.28° < θ < 43.08°
	9778 reflections used at 100K	9149 reflections used at 100K
Data Collection		
Temperature	100K	100K
Diffractometer	Bruker APEX-II CCD	Bruker APEX-II CCD
Radiation source	Incoatec microfocus sealed tube	Incoatec microfocus sealed tube
Radiation and wavelength	MoK <sub>α</sub> , 0.71073 Å	MoK <sub>α</sub> , 0.71073 Å
Monochromator	multilayer monochromator	multilayer monochromator
Scan type	φ and ω scans	φ and ω scans
θ range for data collection	1.78 to 32.00°	1.92° to 36.00°
Reflections collected / unique	60013 / 9630	109342 / 11757
Significant unique reflections	8050 with I > 2σ(I)	9802 with I > 2σ(I)
R(int), R(sigma)	0.0434, 0.0295	0.0597, 0.0312
Completeness to θ = 36.0°	100.0%	100.0%
Refinement		
Refinement method	Full-matrix least-squares on F <sup>2</sup>	Full-matrix least-squares on F <sup>2</sup>
Data / parameters / restraints	9630 / 351 / 0	11757 / 291 / 0
Goodness-of-fit on F <sup>2</sup>	1.017	1.032
Final R indices [I > 2σ(I)]	R1 = 0.0230, wR2 = 0.0469	R1 = 0.0241, wR2 = 0.0457
R indices (all data)	R1 = 0.0351, wR2 = 0.0506	R1 = 0.0351, wR2 = 0.0488
Extinction expression	None	none
Weighting scheme	w = 1/[σ <sup>2</sup> (F <sub>o</sub> <sup>2</sup> )+(aP) <sup>2</sup> +bP] where P = (F <sub>o</sub> <sup>2</sup> +2F <sub>c</sub> <sup>2</sup> )/3	w = 1/[σ <sup>2</sup> (F <sub>o</sub> <sup>2</sup> )+(aP) <sup>2</sup> +bP] where P = (F <sub>o</sub> <sup>2</sup> +2F <sub>c</sub> <sup>2</sup> )/3
Weighting scheme parameters a, b	0.0235, 1.6293	0.0127, 2.6752
Largest Δ/σ in last cycle	0.001	0.002
Largest difference peak and hole	1.623 and -1.300e/Å <sup>3</sup>	1.928 and -1.064e/Å <sup>3</sup>
Structure Solution Program	SHELXS-97 (Sheldrick, 2008)	SHELXS-97 (Sheldrick, 2008)
Structure Refinement Program	SHELXL-2014/6 (Sheldrick, 2015)	SHELXL-2014/6 (Sheldrick, 2015)

**Table 12:** Selected bond lengths [Å] and angles [°] for [W(CO)(C<sub>2</sub>Ph<sub>2</sub>)(L3S)Br] (**1**).

W(1)-C(1)	2.034(2)	S(1)-W(1)-Br(1)	159.232(15)
W(1)-C(2)	2.066(2)	C(2)-C(1)-C(101)	133.2(2)
W(1)-C(3)	1.956(2)	C(1)-C(2)-C(201)	136.4(2)
W(1)-N(12)	2.2748(18)	O(3)-C(3)-W(1)	177.0(2)
W(1)-N(22)	2.2897(19)	C(5)-S(1)-W(1)	108.42(7)
W(1)-S(1)	2.3759(6)	C(13)-N(12)-N(11)	105.15(17)
W(1)-Br(1)	2.6152(4)	C(13)-N(12)-W(1)	134.19(14)
C(1)-C(2)	1.318(3)	N(11)-N(12)-W(1)	120.45(13)
C(1)-C(101)	1.460(3)	C(23)-N(22)-N(21)	105.42(17)
C(2)-C(201)	1.459(3)	C(23)-N(22)-W(1)	134.00(15)
C(3)-O(3)	1.148(3)	N(21)-N(22)-W(1)	119.25(14)
S(1)-C(5)	1.831(2)	C(1)-C(2)-W(1)-C(3)	-171.55(16)
C(3)-W(1)-N(12)	166.27(8)	C(101)-C(1)-C(2)-C(201)	3.2(5)
C(1)-W(1)-N(22)	165.17(8)	W(1)-S(1)-C(5)-C(4)	30.49(16)
C(2)-W(1)-N(22)	157.35(8)		

**Table 13:** Selected bond lengths [Å] and angles [°] for [W(CO)(C<sub>2</sub>Me<sub>2</sub>)(L3S)Br] (**2**).

W(1)-C(1)	2.0205(19)	S(1)-W(1)-Br(1)	160.301(13)
W(1)-C(2)	2.0691(18)	C(2)-C(1)-C(10)	140.6(2)
W(1)-C(3)	1.9513(19)	C(1)-C(2)-C(20)	140.6(2)
W(1)-N(12)	2.2430(15)	O(3)-C(3)-W(1)	178.95(18)
W(1)-N(22)	2.3160(15)	C(5)-S(1)-W(1)	107.60(6)
W(1)-S(1)	2.3814(5)	C(13)-N(12)-N(11)	105.17(14)
W(1)-Br(1)	2.6009(3)	C(13)-N(12)-W(1)	133.10(13)
C(1)-C(2)	1.307(3)	N(11)-N(12)-W(1)	121.43(11)
C(1)-C(10)	1.479(3)	C(23)-N(22)-N(21)	105.18(14)
C(2)-C(20)	1.480(3)	C(23)-N(22)-W(1)	133.72(12)
C(3)-O(3)	1.148(2)	N(21)-N(22)-W(1)	119.30(11)
S(1)-C(5)	1.8264(18)	C(1)-C(2)-W(1)-C(3)	-175.93(15)
C(3)-W(1)-N(12)	167.97(7)	C(10)-C(1)-C(2)-C(20)	-9.9(5)
C(1)-W(1)-N(22)	157.18(7)	W(1)-S(1)-C(5)-C(4)	34.34(12)
C(2)-W(1)-N(22)	161.74(7)		